공학박사 학위논문

Studies on Oligoethylene Glycol Chain Engineering of Indolo[3,2-b]indole Based Organic Semiconductors

에틸렌 글라이콜과 인돌로[3,2−b]인돌을 기반으로 한 유기반도체의 합성, 특성 및 응용에 대한 연구

2023년 02월

서울대학교 대학원

재료공학부

홍 승 화

Studies on Oligoethylene Glycol Chain Engineering of Indolo[3,2-b]indole Based Organic Semiconductors

A THESIS SUBMITTED IN PARTIAL FULFILLMENT OF
THE REQUESTMENTS FOR THE DEGREE OF
DOCTOR OF PHILOSOPHY
IN ENGINEERING AT THE GRADUATE SCHOOL OF
SEOUL NATIONAL UNIVERSITY

February 2023

By

Seung Hwa Hong

Supervisor

Prof. Soo Young Park

Studies on Oligoethylene Glycol Chain Engineering of Indolo[3,2-b]indole Based Organic Semiconductors

에틸렌 글라이콜과 인돌로[3,2−b]인돌을 기반으로 한 유기반도체의 합성, 특성 및 응용에 대한 연구

지도 교수 박 수 영

이 논문을 공학박사 학위논문으로 제출함

2023 년 02 월

서울대학교 대학원

재료공학부

홍승화

홍승화의 박사 학위논문을 인준함

2023 년 02 월

위 원 장 안 철 희 (인)

부위원장 박 수 영 (인)

위 원 권 민 상 (인)

위 원 김 재 필 (인)

위 원 권 지 언 (인)

Abstract

Studies on Oligoethylene Glycol Chain Engineering of Indolo[3,2-b]indole Based Organic Semiconductors

Seung Hwa Hong
Department of Materials Science Engineering
The Graduate School
Seoul National University

Solution processable organic semiconductors have been investigated over the past decade and are widely used in various organic electronic devices such as organic field-effect transistors and organic solar cells. To improve device properties, multiple types of π-conjugated molecules have been synthesized and investigated. In particular, heteroacenes have been extensively studied due to their outstanding Opto- and electronical properties with versatile processability. Especially pyrrole-containing heteroacenes also received significant attention because controlling the solubility of molecules could easily modulate by the Sn2 reaction at their N-position than other heteroacenes molecules. Therefore, Among various types of pyrrole-fused heteroacenes, I have focused particular attention on fluorinated indolo[3,2-b]indole (IDID) unit, which comprises two inner pyrrole rings, and two outer benzene rings fused all together. Moreover, substituting fluorine (F) atoms on IDID backbone could provide an extended and planar π-conjugated backbone structure. However, its organic semiconductor applications have rarely been explored owing to a lack of solubility for device processability. In this regard, this dissertation describes the following two main topics; i) replacing the carbon alkyl chains with the hydrophilic side chains, such as the oligo ethylene glycol (OEG) chains, to provide better solubility for efficient device fabrication and facilitate further tight molecular packing nature to improve charge transporting properties ii) modulating the length of OEG chains for the development of high performance organic

semiconductor.

In recent years, it has been widely believed that the suitable utilization of hole transporting materials (HTMs) in the perovskite solar cells (PSCs) represents one crucial factor in developing high-performing inverted (*p-i-n*) and conventional (*n-i-p*) PSCs. Therefore, various dopant-free HTMs have been extensively investigated for the past years. Significantly, the planar type HTMs provided high hole mobility owing to their high molecular planarity and tight π–π stacking feature. Nevertheless, the planar type HTMs have the disadvantage of introducing a particular solubility issue into their planarity, which easily results in rough film morphology. Such a feature has negatively impacted device performance. It has not been sufficiently examined because providing solubility and maintaining tight molecular stacking features is expected to have intrinsic trade-off characteristics.

Firstly, diethylene glycol (DEG) side chains are introduced at the N-positions of the rigid fluorinated IDID backbone structures to guarantee considerable advantages in their solubility regarding efficient device fabrication and obtaining further tight molecular packing. The optimized DEG-IDIDF showed proper HOMO energy level, hole mobility, film crystallinity, and superior intrinsic stability compared to PEDOT:PSS. In particular, tight molecular packing is induced due to a strong intermolecular interaction between diethylene glycol chains and IDID backbone core. The inverted PSCs device using DEG-IDIDF HTM exhibited superior performance, with a high PCE of 16.60% in dopant-free conditions, maintaining its efficiency up to 500 hours under annealing at 60 °C.

Besides the apparent advantages of DEG side chains, I could successfully design and synthesize hole transport materials (HTM) for conventional perovskite solar cells, referred to as TEG-IDIDF having a tri-ethylene glycol (TEG) side chains at *N*-positions of the fluorinated IDID core. The TEG-IDIDF showed proper HOMO energy level, higher hole mobility, crystallinity, and superior intrinsic thermal and air property compared to Spiro-OMeTAD. In particular, tight molecular packing is induced due to a strong intermolecular interaction between triethylene glycol chains and IDIDF core through C O ••• H hydrogen bonding. The perovskite solar cell device using TEG-IDIDF HTM exhibited superior performance, with a high PCE of 18.09% in dopant-free condition, maintaining its efficiency up to 50 days under a highly humid atmosphere (RH 65%), along with good thermal stability under annealing at

60 °C for 120 hours. Moreover, FAPbI3 based PSCs device with TEG-IDIDF exhibited superior PCEs of doped (22.71%) and non-doped (20.42%). Our findings demonstrate that crystalline HTM ensures much better air and thermal stability than those of devices using Spiro-OMeTAD. We believe that the crystalline HTM can be an alternative to amorphous Spiro-OMeTAD and should be further studied with the development of the perovskite layer.

Lastly, with the growing demand for environmentally sustainable electronic devices such as organic field-effect transistors (OFETs), developing green solvent processable OSCs has been the subject of intensive focus as one alternative option because of their numerous benefits until now. Thus, diverse research efforts have been devoted to replacing the carbon alkyl chains with hydrophilic side chains, such as the OEG side chains. However, the alcohol processable small molecules with the OEG side chains are yet to be developed. Therefore, the Penta-ethylene glycol (PEG) side chains are introduced at the N-positions of the fluorinated IDID backbone structures to guarantee considerable advantages in their solubility without having molecular distortion. The optimized PEG-IDIDF was found to be nicely soluble in alcohol solvents. Moreover, when the PEG-IDIDF was dissolved in a binary solvent system such as ethanol water co-solvents, more ordered packing features and larger grains with uniform morphology were exhibited, compared to the films fabricated by a single solvent such as chloroform or ethanol. The OFET devices prepared from the co-solvents provided high hole mobility of 4.07×10^{-3} cm^2 V^{-1} s^{-1}, along with a high current on/off ratio of ~10^6

Keyword: organic semiconductor, organic field effect transistor, perovskite solar cells,indolo[3,2-b]indole, hole-transporting characteristic, oligo(ethylene) glycol chains, green solvent processing

Student Number: 2019-32576

Contents

List of Tables

List of Schemes

List of Figures

Chapter 1. Introduction

1.1 Organic Semiconductors

Since the discovery of polyacetylene by Sirakawa, MacDiarmid, and Heeger in 1977, π-conjugated functional organic semiconductors (OSCs) have garnered considerable interest as promising options in a variety of their potential organic electronic devices, such as organic light emitting diodes (OLEDs), organic field-effect transistors (OFETs), organic photovoltaics (OPVs).[1-8] Intensive research efforts have been explored academically and commercially. Magnificent advances in electrical performance and theoretical fundamentals have been successfully achieved.[9,10] Therefore, developing novel π-conjugated molecules and polymers has been widely researched in electronic devices because they commonly employ OSCs as an active layer.[11,12] Although various types of devices and their different architectures are operated by a different mechanism, charge transporting characteristics of π-conjugated molecules and polymers are crucially dependent on device performance, especially for OFETs and OPVs.[27] Moreover, extensive studies on the molecular design of OSCs have been successfully considered a new research field, providing a chance to overcome the limitation of inorganic semiconductors. Moreover, they have been used in various applications

compared to inorganic counterparts due to their chemical versatility, various processability, and easily modulating intrinsic characterics, such as electrical, mechanical, thermal, and photophysical properties. For instance, organic electroluminescent layer and several charge transporting layers of OLEDs have already been successfully commercialized in big industrial market. Other applications such as organic field effect semicondcutors, have already exhibited outstanding hole (over ~ 40 cm^2 V^{-1} s^{-1}) for p-type and electron (over ~ 10 cm^2 V^{-1} s^{-1}) for n-type mobility of organic semiconductors compared to amorphous silicon.[13,14] The power conversion efficiency of organic solar cells ~10%, and perovskite solar cells have been exceeding ~20%, recently.[15,16] However, despite this rapid progress in performance, in terms of fundamental research side, device stability, unclear phenomena, and environmentally sustainable or fabrication have not been fully explored, hindering their market entrance.[17-20] Therefore, to solve the aforementioned issues, developing and understanding new materials is highly demanded.

1.1.1 Perovskite Solar Cells

Perovskite, the structure of ABX_3 (A and B are cations and X is anion) refers to the crystal structure of calcium titanate($CaTiO_3$) and it has the three-dimensional structure of ABX_3 (A and B are cations and X is anion) as shown in **Figure 1.1**.[21,22] In the perovskite materials, A is composed of organic or

inorganic cations such as methylammonium ion (CH_3NH_3), formamidinium (FA), and Cs, and B is Sn or Pb The anion X- is a halogen. In general, an iodide, bromide and chloride are the most common halogen in a single or mixed halide perovskite.[23-26] In 1978, Weber's group reported the $MAPbI_3$ perovskite and then Miyasaka group provided that the perovskite layer could be used as light absorbers reaching efficiencies of 3.8% in 2009.[27] Since then, excellent optoelectronic properties of perovskite, such as long range absorb high panchromatic absorption, high absorption coefficient, low excition binding energy, and easy processability, led to the rapid development of perovskite solar cells (PSCs). In recent years, the power conversion efficiencies (PCE) of PSCs have dramatically increased from 3.8 % to 25 %, thereby offering great opportunities and now comparable with crystalline silicon solar cells. For now, as shown in **Figure. 1.2** the PSCs can be divided into two groups based on their architecture and components: a) *n-i-p* conventional structure and b) *p-i-n* inverted structure. Among the different PSC architectures, the *n-i-p* (meso- or planar) conventional device configuration is widely used due to the structure originating from the dye-sensitized solar cells (DSSC) and the device performance with PCE greater than 24%.[28,29] However, the *n-i-p* conventional structure inevitably requires a high-temperature procedure, which makes the manufacturing process more complex and hampers the development of a

flexible device. Moreover, it is well known that device stability is still a major issue because hygroscopic dopants are highly demanded to improve hole mobility of organic hole transporting materials for high performance device stability. To overcome this limitation, the *p-i-n* inverted PSCs have also been of considerable interest as one crucial step towards unlocking the possible production of a low-temperature fabrication process compared with the conventional PSCs. However, the device performance of the inverted PSCs still lags behind compared to conventional PSCs because of the relatively lower open-circuit voltage (V_{oc}) and fill factor (FF), which are dominated by the interfaces between the perovskite and the hole transporting layers. Thus, developing novel hole transporting materials for both *n-i-p* conventional PSCs and *p-i-n* inverted PSCs is required to improve the device performance and stability.

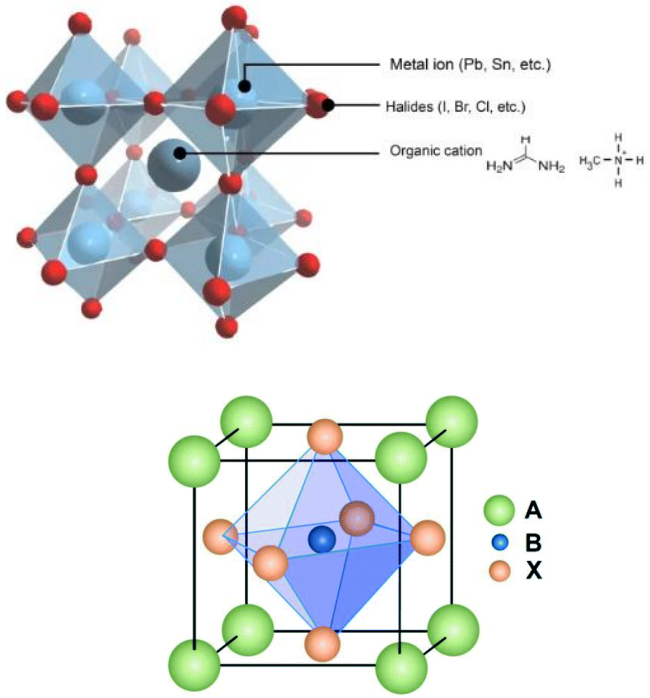

Figure 1.1 crystal structure of ABX_3, and extended strcutre of perovskite

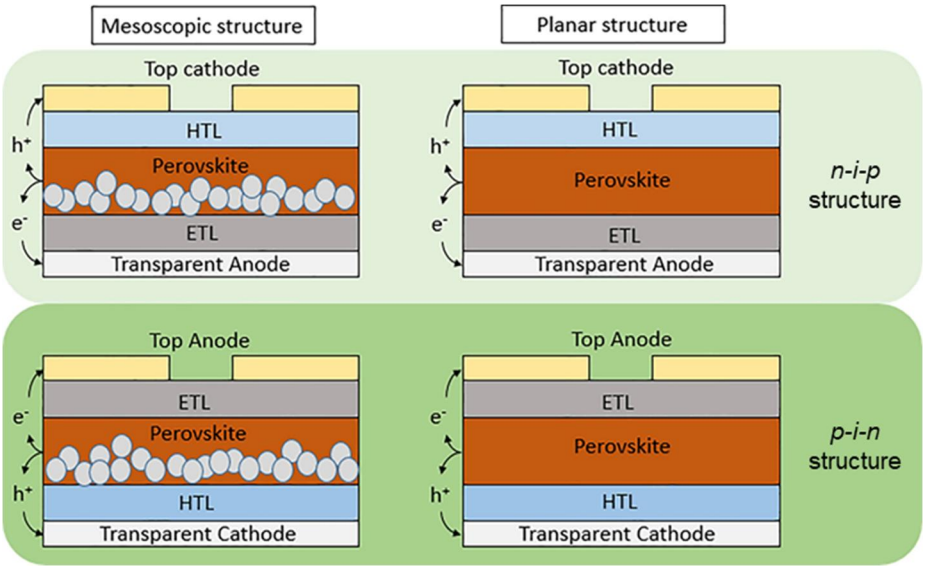

Figure 1.2 Structure of Perovskite solar Cells (conventional and Inverted)

1.1.1.1 PSCs working mechanism

The basic working mechanism (**Figure 1.3**) of conventional and inverted PSCs is similar to that of the DSSC. The absorption of light in the perovskite layer generates free electrons and holes. The excition binding energy of halide perovskite is relatively small, leading to an efficient generation of free carriers upon light absorption. Charge separation occurs by injecting the electrons into the conduction band of the electron transport material and then traveling through the electrode. Also, proper HOMO energy level (5.0eV ~ 5.4eV) of the HTM allows hole to be extracted from the perovskite to the electrode. It is crucial that these steps are kinetically faster than the recombination process at the interfaces ETL/perovskite/HTM.[30-32] Solar cell performance under illumination are characterized by current density- voltage curve (**Figure 1.4**).[33-35] The device performance of perovskite solar cells is represented by power conversion efficiency (PCE), and there are four parameters for evaluating solar cells performance such as short circuit current density (J_{sc}), open circuit voltage (V_{oc}), fill factor (FF), and PCE are determined by the following formula;

$$\mathrm{PCE} = \frac{\mathrm{P_{max}}}{\mathrm{P_{in}}} = \frac{V_{oc} * J_{sc} * FF}{P_{in}} \quad (\mathbf{1.1})$$

$$FF = \frac{J_{max} * V_{max}}{J_{sc} * V_{oc}} \quad (\mathbf{1.2})$$

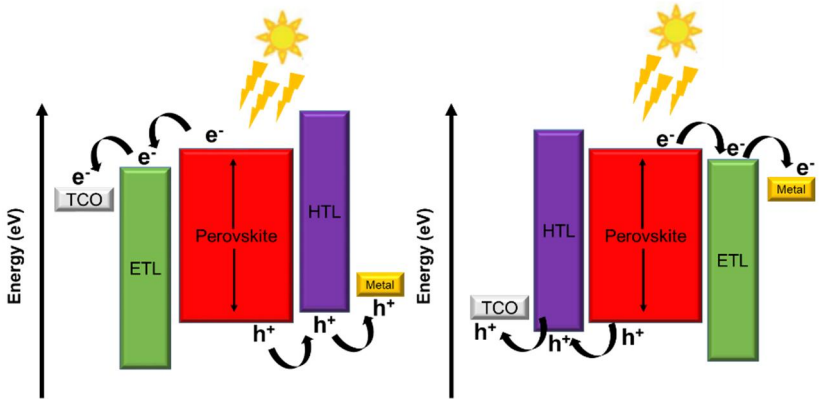

Figure 1.3 Schemetic diagram of conventional and inverted perovskite solar cells operation

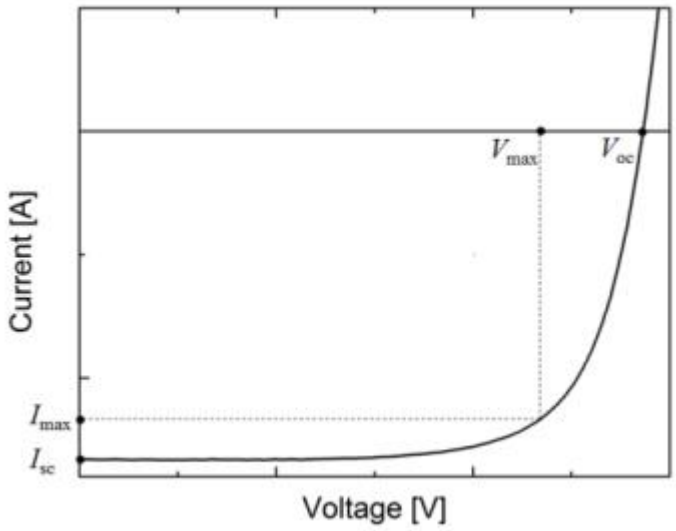

Figure 1.4 current density–voltage curve of solar cells and photovoltaic parameters represented in current density–voltage curve.

1.1.1.2 Hole Transporting materials

In general, a variety of π-conjugated organic molecules as HTMs have been extensively studied due to their tunability of the electronic properties via molecular engineering than inorganic materials. It is widely believed that the HTM plays a crucial role in the mechanism of PSCs and works as a critical component in almost all PSC device architectures. As mentioned above, The HTMs extract the photogenerated holes from the perovskite and transport them to the electrode. Also, The HTM also serves as an electron blocking layer between the electrode and perovskite layer, minimizing charge recombination.[36,37] Additionally, the HTM influences the open circuit voltage and reduces the degradation at the Electrode/perovskite interface. Therefore, the realization of higher efficient PSCs demands the choice of a suitable HTM meeting the following desirable features: 1) HOMO energy level for efficient extraction, 2) hole mobility 3) good solubility for device processability, and 4) good thermal and moisture stability.[38-44] Moreover, depending on the device structure, the basic function of the HTM includes slightly different. In a typical *n-i-p* PSCs, the HTMs stacked on top of the perovskite layer play a critical role in mitigating the device degradation, which can minimize the invasion of moisture and subsequent performance degradation. Thus, optimal film

thickness is needed to cover the whole perovskite layer. On the other hand, the HTMs in the inverted PSCs have been believed to serve as an interlayer between the perovskite layer and the bottom electrode. Thus, the dense HTMs are highly demanded because of the unintended invasion of moisture or oxygen between the perovskite layer and bottom electrode during device operation. Moreover, the HTM should ensure high thermal stability characteristics because the quality of the perovskite layer is highly dependent on the post-annealing process (~ 100 °C).

To date, the widely adapted HTM in the inverted PSCs has been the poly(3,4-ethylenedioxy thiophene):poly(styrenesulfonate) (PEDOT:PSS), when organic HTMs in conventional PSCs, 2,2',7,7'tetrakis-(N,N-di-p-methoxy-phenyl-amine)-9,9-spiro- bifluorene (Spiro-OMeTAD) have shown promise as one of the most effective and widely used HTM molecules. However, both HTMs still exhibited relatively mismatching energy levels and instability features. Significantly, the Spiro-OMeTAD typically require additional dopants such as lithium bis(trifluoromethanesulfonyl)imide (Li-TFSI), and tert-butylpyridine (t-BP), and cobalt complex (FK209) to enhance their hole mobility (**Figure 1.5**).[45,46] However, such Li-salt dopants often accelerate the degradation of the device due to their hygroscopic nature. Also, the relatively low glass temperature of Spiro-OMeTAD causes another performance

degradation due to film crystallization during thermal annealing. Therefore, developing dopant-free HTMs for stable inverted and conventional PSCs is highly demanded to solve the dopant issue.

Recently, various types of organic dopant-free HTMs were studied, and they can be divided into two major categories: small organic molecules and polymers. It is well known that organic small molecule base HTMs are more studied than polymer base HTMs due to their reproducibility, processability, tunable energy levels, and improvement in stability. A rigid core structure, including carbazole, truxene, quinolizino, acridine, and indacenodithiophene, has been considered instead of spiro-core as central core structures their planar backbone structure could improve the intermolecular π–π interactions and the corresponding hole mobility. Especially, as shown in **Figure 1.6 and 1.7**, two types of dopant-free small molecules HTMs were studied, such as TPA-based HTMs and non-TPA HTMs (planar type HTMs).[47-49] The TPA-based HTMs used the bulk function groups of triphenylamine or diphenylamine derivatives as end-capping groups to regulate the state of molecular aggregation and provide good solubility for device processing and uniform morphology. However, their end-capping group could interrupt the tight molecular packing and regulate their charge transporting characteristics. To overcome the aforementioned issue, developing planar type HTMs is highly demanded, but

the solubility issue for device processability remains to solve.

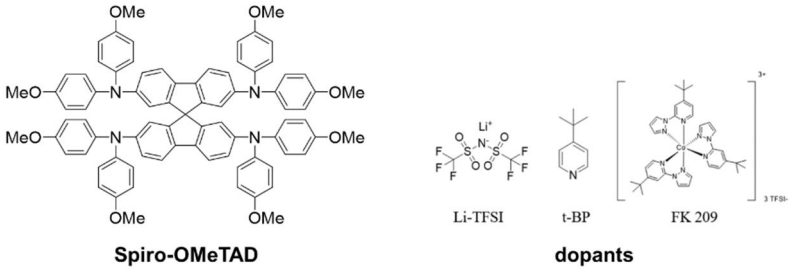

Figure 1.5 Molecular structure of Spiro-OMeTAD, and dopants: lithium bis(trifluoromethanesulfonyl)imide (Li-TFSI), tert-butylpyridine (t-BP), and cobalt complexes (FK209).

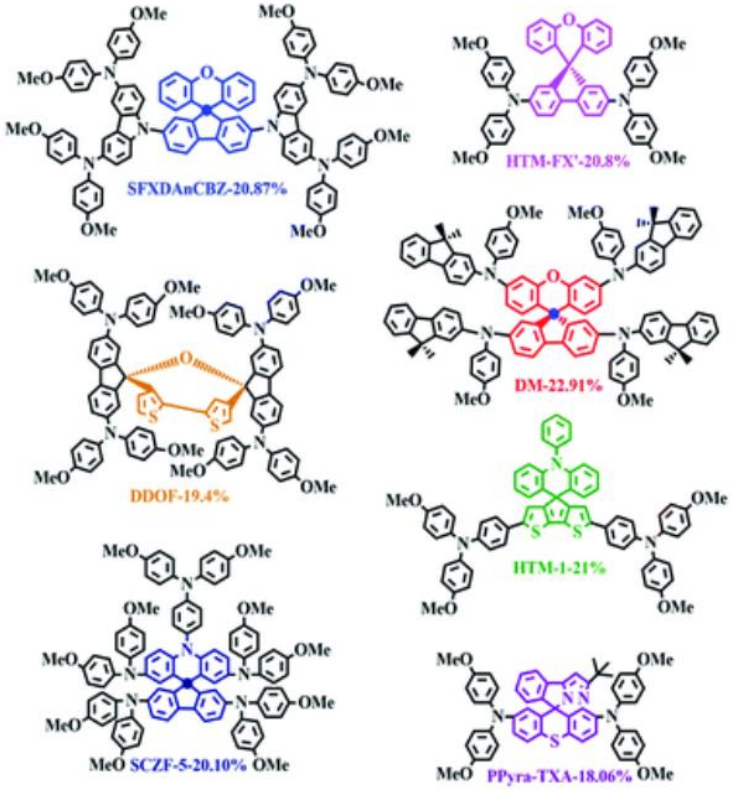
SFXDAnCBZ-20.87%
HTM-FX'-20.8%
DM-22.91%
DDOF-19.4%
HTM-1-21%
SCZF-5-20.10%
PPyra-TXA-18.06%

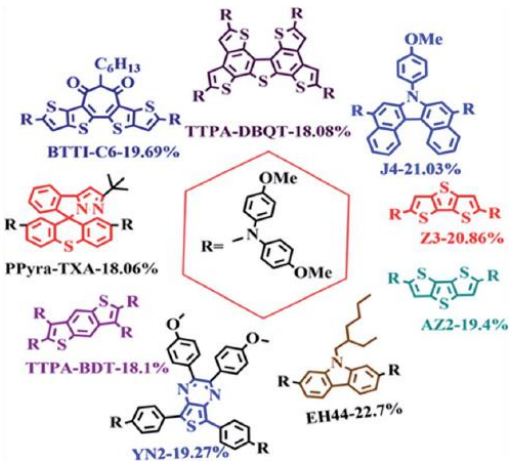
BTTI-C6-19.69%
TTPA-DBQT-18.08%
J4-21.03%
PPyra-TXA-18.06%
R=
Z3-20.86%
AZ2-19.4%
TTPA-BDT-18.1%
EH44-22.7%
YN2-19.27%

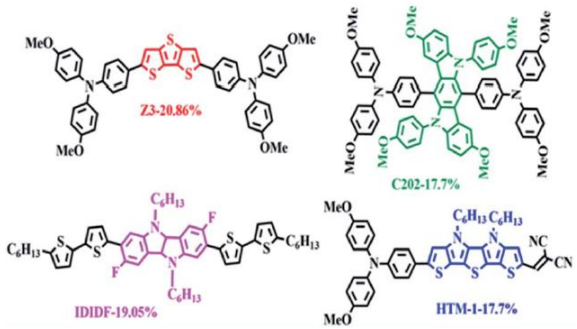

Figure 1.6 Molecular structure of spiro-based, diphenylamine containing, and heteroacenes hole transport materials with dopants

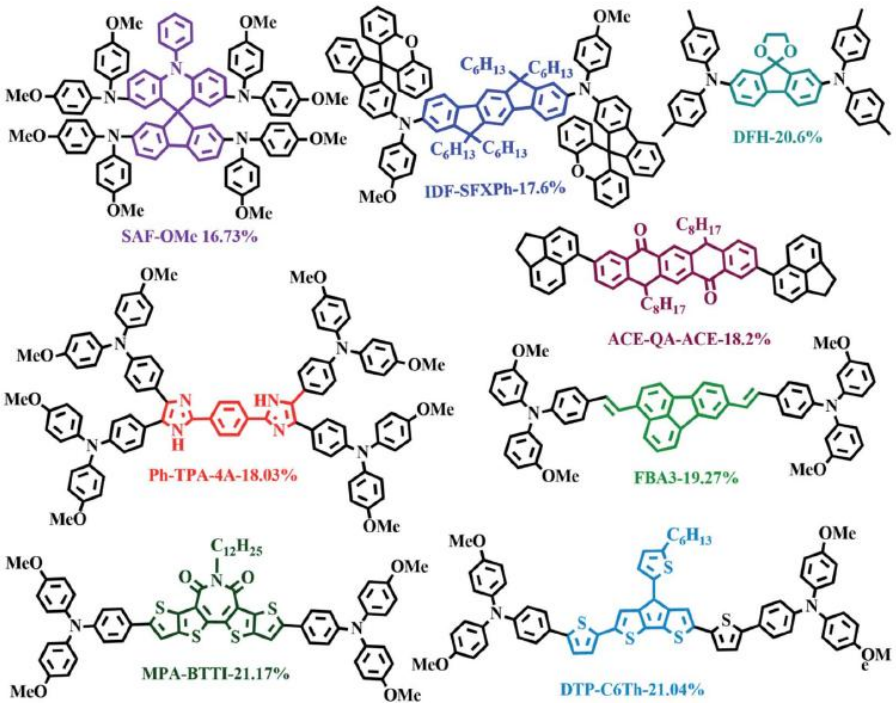

Figure 1.7 Various molecular structures of dopant-free HTMs

1.1.2 Organic Field-Effect Transistor

Recent advances in π-conjugated functional organic semiconductors (OSCs) have garnered considerable interest as promising options in a variety of their potential organic electronic devices, such as organic field effect transistors (OFETs). They are essential components in organic integrated circuits of various electronic devices, for instance, display drivers, smart cards, electronic identification tags, etc. The organic part of OFETs can exhibit numerous benefits, including lower cost and temperature for the device fabrication, lightweight and high flexibility, etc. Extensive studies on the molecular design of OSCs have improved charge transporting characteristics.

1.1.2.1 OFET working mechanism

OFETs consists of three components: organic semiconductor, insulating gate dielectric, and contacts (gate, drain, and source) and there are four types of OFETs device configuration (**Figure 1.8**): (A) Bottom gate Top contact, (B) Bottom gate Bottom contact, (C) Top gate Bottom contact, (D) Top gate Top contact. Generally, (a) and (b) exhibit better device performance than others due to the interface between the organic semiconductor and the electrodes

having better contact conditions.[50] In principle, as shown in **Figure 1.9**, a linear regime can be described when V_{ds} is smaller than (V_g – V_{th}), and the current Ids is increased with the increasing of V_{ds}. The channel is pinched off when V_{ds} is equal to (V_g – V_{th}). Saturation regime exhibited if Vds is higher than (V_g – V_{th}), the increasing of Ids gradually becomes saturated and express constant value.

The current I_{ds} can be derived by the following equation, where C_i is the capacitance per unit area of the gate dielectric, W is the channel width, L is the channel length, V_G is the gate voltage, μ is the charge mobility:

$$I_{ds,lin.} = \frac{W}{L} \mu_{lin.} C_i (V_g - V_{th}) V_{ds}$$

In linear regime, the field-effect mobility can be derived from the gradient of I_D versus V_G at constant V_{DS}:

$$\mu_{lin.} = \frac{\partial I_{ds}}{\partial V_g} \cdot \frac{L}{W C_i V_{ds}}$$

Meanwhile, in the saturation regime, the current is saturated, attributed to pinch-off, thus I_{ds} for the saturation regime can be simplified to,

$$I_{ds,sat.} = \frac{W}{2L} \mu_{sat.} C_i (V_g - V_{th})^2$$

The field-effect mobility, in saturation regime, can be derived by the following equation when the gate voltage and the square root of the saturation current are directly proportional.

$$\mu_{sat.}(V_g) = \frac{\partial I_{ds,sat}}{\partial V_g} \cdot \frac{L}{W C_i} \cdot \frac{1}{V_g - V_{thi}}$$

Transfer and output curve of OFETs are shown in **Figure 1.10**. At given V_g, linear and satureation regime can be found from the output cuve. Also, the mobility can be calculated from the transfer curve as mentioned above. On/off ratio, switching behavior in OFETs, is another important parameter in OFETs and can be extracted from the transfer curve V_{th} and S can be simply calculated by

$\sqrt{I_d}$ $vs. V_g$ plot, and $S = dV_g/d(logI_d)$.

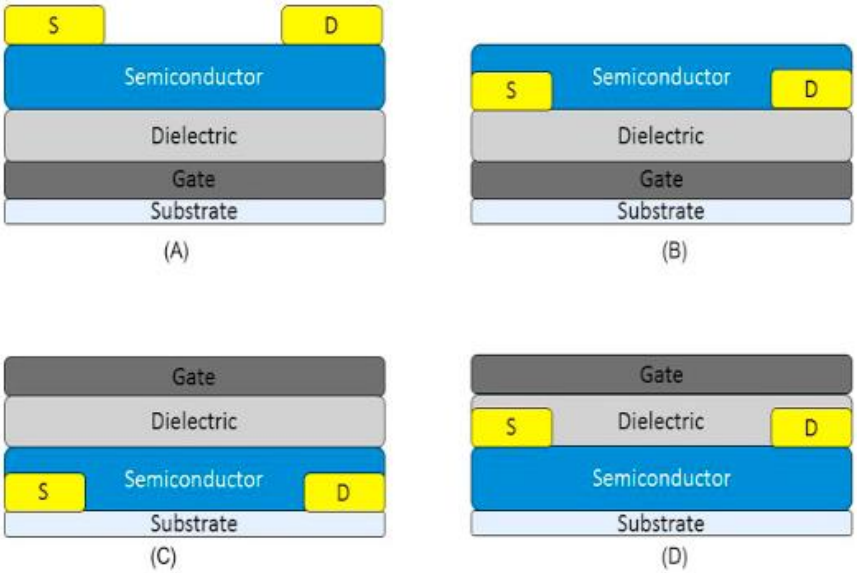

Figure 1.8 Various configurations of organic field effect transistors. (A) Bottom gate Top contact, (B) Bottom gate Bottom contact, (C) Top gate Bottom contact, (D) Top gate Top contact.

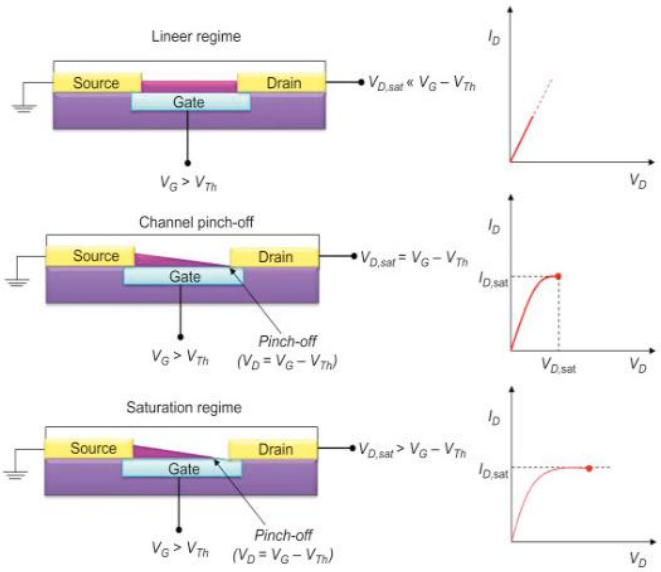

Figure 1.9 OFET working conditions and corresponding current-voltage characteristics: linear regime condition; start of saturation regime at pinch-off; saturation regime condition (VD, drain voltage; V_G, gate voltage; V_{Th} threshold voltage; ID, drain current). OFET, organic field effect transistor.

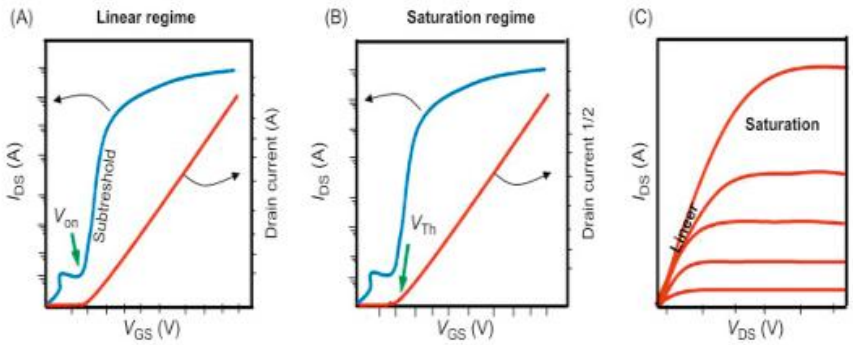

Figure 1.10 Representative current–voltage characteristics of an OFET: (A, B) transfer characteristics in both regimes (linear/saturation) and (C) output characteristics indicating the linear and saturation regimes in the same graph.

1.1.2.2 Organic Semiconductors and acenes derivatives

Previously, acenes and their derivatives have attracted attention as an active layer of OFETs due to their high electronic and optical properties (**Figure 1.11**). The device with anthracene and tetracene exhibited high mobility up to 3 cm^2 $V^{-1}s^{-1}$.[51] Moreover, the single crystal devices with pentacene, five fused benzene rings, exhibited around 40 cm^2 $V^{-1}s^{-1}$ mobility through the device optimization. However, as mentioned above, it is widely believed that the above acene and their derivatives have still been restricted by poor solubility and photooxidation. Therefore, various chemical structure modifications, e.g., substituting additional bulky groups, introducing halogen atoms, or replacing benzene rings with thiophene rings, have been extensively investigated for the past years. For example, Bao and Zhu's group reported that introducing chlorinated years. For example, Bao and Zhu's group reported that introducing chlorinated at 5- and 11-position of pentacene affected the packing motif and exhibited impressive hole mobility.[52]

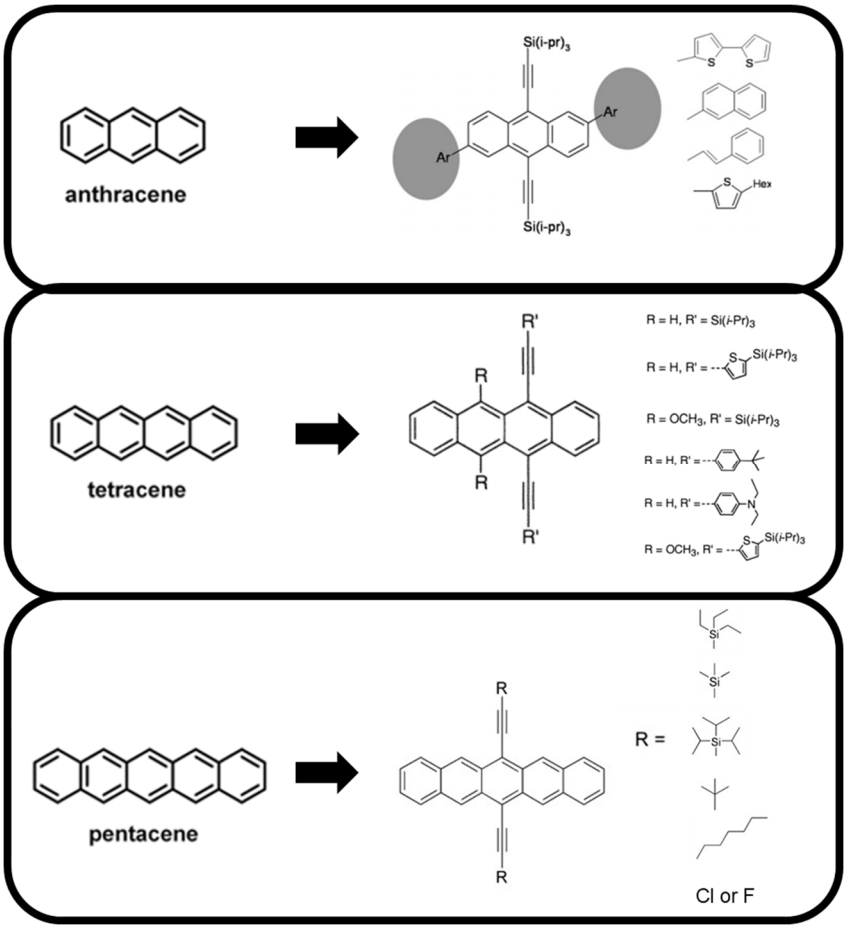

Figure 1.11 Chemical structure of Acenes and their derivatives

1.2 Sulfur or Nitrogen containing Heteroacene

As mentioned in **Chapter 1.1**, small molecule organic semiconductors have been intensively studied, and they were used in various device applications because of their rigid and linear fused acene rings with extended π-conjugated structure, which provides outstanding charge transporting characteristics.[53] However, the lack of substitution sites and their planarity showed several issues, including poor solubility and hard-to-modulate molecular structure. Therefore, heteroacenes have been studied as a new fused π-conjugated structure molecular system with facilitating stability, tight molecular stacking, and rigid backbone. Especially, sulfur (S) and nitrogen (N) atoms containing heteroacenes are the most investigated due to inducing intermolecular secondary interaction. Among various types of sulfur containing heteroacenes, BTBT derivatives have shown promise as one of the most effective and widely used heteroacenes molecules due to their tight molecular packing with superior charge carrier mobility.[54,55] As shown in **Figure 1.12**, BTBT derivatives usually exhibited a 2-dimensional lamellar structure with herringbone packing motif. Furthermore, various fabrication methods such as vacuum deposition, off-centered spin-coating, spin-coating, and crystal devices have achieved extreme mobility of 43 cm^2 V^{-1} s^{-1}. Meanwhile, nitrogen-

containing heteroacenes, pyrrole-fused heteroacenes, also received attention because their solubility is easily modulated by the Sn2 reaction at their *N*-position than other heteroacenes molecules.[56-58] To date, carbazole and indolocarbazole, nitrogen-containing heteroacenes, were adopted in various organic electronic applications owing to their synthetic versatility and their linearly fused pentacene like analog and N-H···π interaction. Depending on their chemical structure for device applications, pyrrole-fused heteroacenes exhibited outstanding hole mobilities of 0.01 ~ 1 cm^2 V^{-1} s^{-1}.[59,60] However, their derivatives still showed relatively lower charge carrier mobility than the sulfur-containing heteroacenes besides, they could provide better solution processability

1.2.2 Solution Processable Small Molecules

Mainly through two primary thin film preparation for various types of device applications: solution processing of soluble molecules and high vacuum deposition of thermally stable molecules. Until now, high vacuum deposition processing has prepared many kinds of organic molecules with high device efficiency. In general, solution processing is more cost-efficient than vacuum deposition, as it does not involve expensive high vacuum systems and is feasible for large-scale roll-to-roll production. Therefore, solution-processable organic small molecules consisting of a rigid backbone and flexible side chains

are highly demanded. Unlike polymers, there is no such entanglement, and the packing density is modulated by molecular structure. Their solubility in various organic solvents comes from their type or length of side chains (**Figure 1.13**). Moreover, flexible side chains can affect the morphology of organic small molecules in the solid state; thus, their optoelectronics properties and device performance are also affected. Therefore, the type and length of side chains are the keys to small molecules.

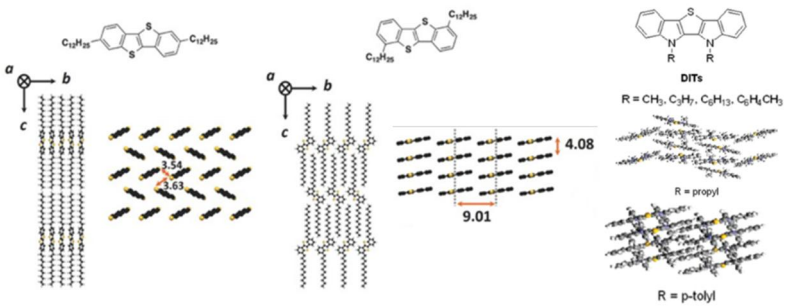

Figure 1.12 Packing structure of sulfur or nitrogen containing heteroatoms elucidated by single crystal crystallography

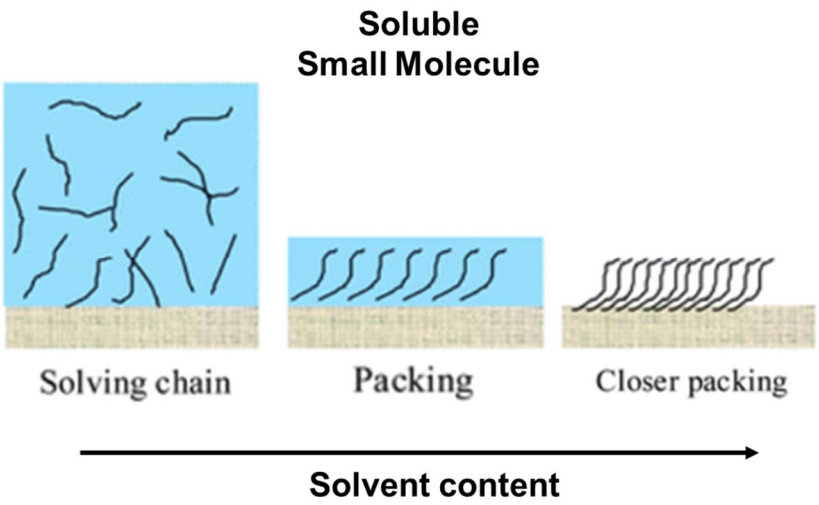

Figure 1.13 Schematic of small molecules during the coating process

1.2.3 Alkyl chains and Oligoethylene glycol chains

Alkyl chains, including linear and branched alkyl chains, are the most commonly employed side chains in OSCs. The influence of alkyl chains on the device performance has been intensively investigated; even a subtle change in the alkyl chains may substantially influence charge transporting characteristics.[61,62] However, relatively long alkyl chains are demanded to provide sufficient solubility when they could interrupt molecular stacking. Therefore, intentional manipulation of both solubility and molecular stacking is one promising way to achieve high device performance because both features are expected to have intrinsic trade-off characteristics. Recently, oligo(ethylene glycol) (OEG) chain is another essential substitution for OSCs, which are well known for their hydrophilicity.[63-65] Indeed, compared with the widely used hydrophobic alkyl chains, they possess several different properties, i.e., hydrophilicity, high polarity, high flexibility, and ionic conductivity owing to alkyl chains with part of CH2 groups replaced by oxygen atoms (**Figure 1.14**).[66-68] Depending on the electronegativity, a carbon-oxygen covalent bond exhibits a dipole moment (μ) of 0.74 Debye, while a carbon-carbon covalent bond showed almost 0 Debye ($\mu \approx 0$). Therefore, OEG side chains lead to strong polarity with hydrophilicity, and OSCs may be soluble in polar organic solvents

such as alcohol or water, unlike hydrophobic carbon alkyl chains. In addition, OEG chains are more flexible than alkyl chains owing to no steric hindrance for the rotation of the C…O bond. As a result, the C…O bond in OEG chains of the energy barrier (E = 0.08 eV) is smaller than that of the C…C bond of the energy barrier (E = 0.11 eV). Meanwhile, OSCs with OEG side chains could have relatively low thermal properties owing to the ionic conductivity of OEG side chains because ion mobility accompanies a large-amplitude excursion of OSCs. Therefore, OSCs bearing OEG side chains should have carefully synthesized, especially in small molecules, and applied in various optoelectronic devices.

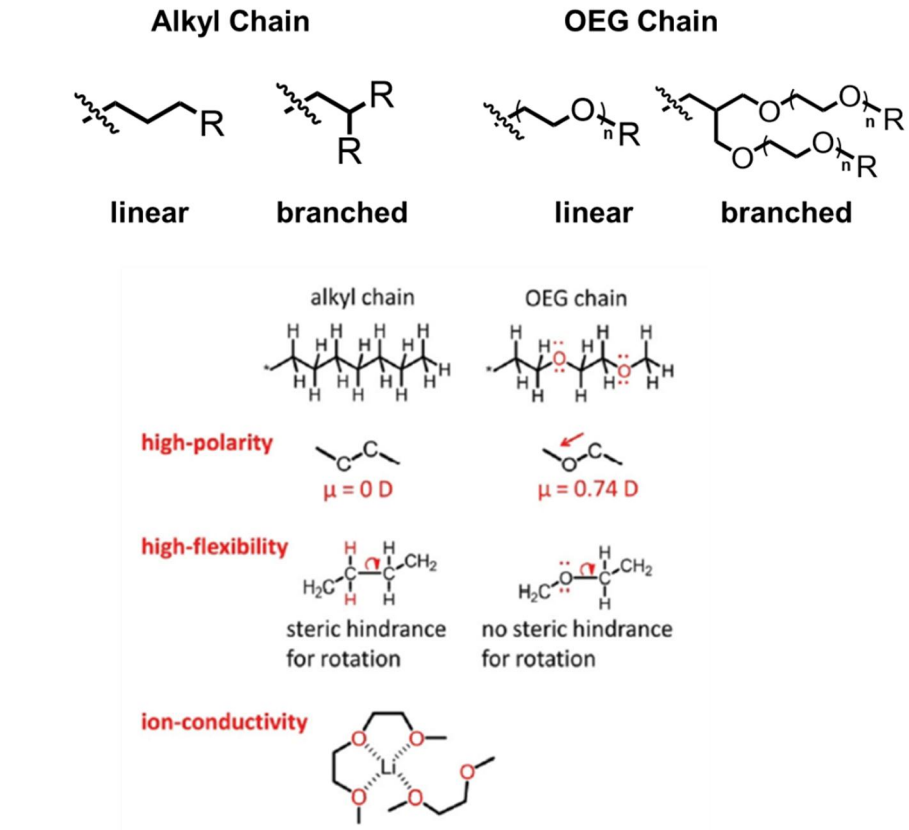

Figure 1.14 Schematic characteristics of OEG chains: high polarity, high flexibility and ionic conductivity.

1.3 Research Proposal

As discussed in **Chapter 1.1** and **Chapter 1.2**, *N*-atom containing heteroacenes have been extensively explored as a structurally and electronically fascinating molecular platform for applications in organic electronics. Based on their strong electron donating nature and controllable π-conjugated system with high flexibility, they are essential given electronic structure engineering. Moreover, easily modulating solubility and molecular stacking by substituting various alkyl chains at the N-position of heteroacenes could provide a rationalization of chemical structure to develop high performance organic semiconductors. In this respect, Among various kinds of pyrrole-fused heteroacenes, indolo[3,2-b]indole (IDID) core which is comprised two pyrrole rings and two benzene rings fused linearly with centrosymmetric geometry, is also investigated as a donor building block for the push-pull structure of small molecule and polymer analog. Attributed to symmetrically-fused two pyrrole rings, IDID exhibited strong electron donating nature, and also solubility of the incorporated structure could be feasibly controlled.[69-71] Also, through the incorporation of fluorine (F) atom into the IDID core, further molecular structure planarization is exhibited with the additional intramolecular interactions (conformation locking). Despite such a promising perspective of IDID core, fluorinated IDID derivatives were restricted by the presence of

rough morphology owing to its insufficient solubility. Therefore, enhancing solubility and controllable crystallinity features in the flourniated IDID derivatives remains a crucial step in our work. Our essential concept of this work is the use of various alkyl chains, especially OEG side chains, on the nitrogen atoms of the IDID core to ensure enhancement in solubility necessary for efficient device fabrication and to facilitate further tight molecular packing nature that directly relates to charge transport and mobility characteristics. In this thesis, I will elaborate on the OEG side chains and fluorinated IDID core as promising organic semiconductor backbone using a newly designed and synthesized family of IDID-based organic semiconductors and their applications in organic electronics, proposing molecular design principles to realize high-performance organic semiconductors.

In Chapter 2, various length of OEG side chains on fluorinated IDID based small molecules as dopant-free hole transporting materials will be presented for efficient and stable inverted and conventional perovskite solar cells.

In Chapter 3, indolo[3,2-b]indole-based crystalline small molecules with penta-ethylene glycol side chains will be introduced for aqueous-alcohol-processable OFETs

1.4 Reference

[1] C. K. Chiang, C. R. Fincher, Y. W. Park, A. J. Heeger, H. Shirakawa, E. J. Louis, S. C. Gau, A. G. MacDiarmid, Phys. Rev. Lett. 1977, 29, 1098.

[2] J. H. Burroiughes, D. D. C. Bradley, A. R. Brown, R. N. Marks, K. Mackay, R. H. Friend, P. L. Burns, A. B. Holms, Nature 1990, 347, 539.

[3] A. Kraft, A. C. Grimsdale, A. B. Holmes, Angew, Chem. Int. Ed. 1998, 37, 402.

[4] G. Horowits, Adv. Mater. 1998, 10, 365.

[5] Z. Bao, J. A. Rogers, H. E. Kats, J. Mater. Chem. 1999, 9, 1895.

[6] H. E. Kats, Z. Bao, S. L. Gilats, Acc. Chem. Res. 2001, 34, 359.

[7] C. J. Brabec, N. S. Sariciftci, J. C. Hummelen, Adv. Funct. Mater. 2001, 11, 15.

[8] K. M. Coakley, M. D. McGehee, Chem. Mater. 2004, 16, 4533.

[9] A. R. Murphy, J. M. J. Fréchet, Chem. Rev. 2007, 107, 1066.

[10] C. Wang, H. Dong, W. Hu, Y. Liu, D. Zhu, Chem. Rev. 2012, 112, 2008.

[11] Y. Shirota, H, Kageyama, Chem. Rev. 2007, 107, 953.

[12] H. Dong, X. Fu, J. Liu, Z. Wang, W. Hu, Adv. Mater. 2013, 25, 6158

[13] O. D. Jurchescu, M. Popinciuc, B. J. van Wees, T. T. M. Palstra, Adv. Mater. 2007, 19, 688

[14] M. Yamagishi, J. Takeya, Y. Tominari, Y. Nakazawa, T. Kuroda, S. Ikehata, M. Uno, T. Nishikawa, T. Kawase, Appl. Phys. Lett. 2009, 90, 182117

[15] H. Li, B. C. K. Tee, J. J. Cha, Y. Cui, J.W. Chung, S. Y. Lee, Z. Bao, J. AM. Chem. Soc. 2012, 134, 2760.

[16] D.-H. Dou, Y.-Q. Zheng, Z.-F. Yao, Z.-A Yu, T. Lei, X. Shen, X.-Y Luo, J. Sun, S.-D. Zhang, Y.-F Ding, G. Han, Y. Yi, J.-Y. Wang, J. Pei, J. Am. Chem. Soc. 2015, 137, 15947.

[17] W. P. Su, J. R. Schrieffer, A. J. Heeger, J. Phys. Rev. Lett. 1979, 42, 1698.

[18] J.-L. Brédas, G. B. Street, Acc. Chem. Res. 1985, 18, 309.

[19] J.-L. Brédas, D. Beljonne, V. Coropceanu, J. Cornil, Chem. Rev. 2004, 104,

[20] L. L. Chua, J. Zaumseil, J. F. Chang, E. C. W. Ou, P. K. H. Ho, H. Sirringhaus, R. H Friend, Nature 2005, 434, 194

[21] Mineralogy Database. 2015, http://webmineral.com/ (2015)

[22] Gao P, Michael G, Mohammad K. N, Energy Environ. Sci 2014, 7, 2448

[23] M. A. Green, A. Ho-Baillie and H. J. Snaith, Nat. Photonics, 2014, 8, 506–514.

[24] N. J. Jeon, J. H. Noh, W. S. Yang, Y. C. Kim, S. Ryu, J. Seo and S. I. Seok, Nature, 2015, 517, 476–480.

[25] G. Grancini, C. Roldan-Carmona, I. Zimmermann, E. Mosconi, X. Lee, D. Martineau, S. Narbey, F. Oswald, F. De Angelis, M. Graetzel and M. K. Nazeeruddin, Nat.Commun., 2017, 8, 15684.

[26] Y. Wu, F. Xie, H. Chen, X. Yang, H. Su, M. Cai, Z. Zhou, T. Noda and L. Han, Adv. Mater., 2017, 29, 1701073.

[27] G. Horowits, *Adv. Mater.* **1998**, *10*, 365.

[28] H. D. Pham, L. Gil-Escrig, K. Feron, S. Manzhos, S. Albrecht, H. J. Bolink and P. Sonar, J. Mater. Chem. A, 2019, 7, 12507–12517.

[29] L. Zhu, J. Xu, Y. Shan, C. Zhong, X. Tang, D. Long, Y. Zhang and F. Wu, J. Mater. Chem. C, 2019, 7, 3226–3230.

[30] Y. Yuan, G. Giri, A. L. Ayzner, A. P. Zoombelt, S. C. B. Mannsfeld, J. Chen, D. Nordlund, M. F. Toney, J. Huang, Z. Bao, Nat. Commun. 2014, 5, 3005.

[31] W. P. Su, J. R. Schrieffer, A. J. Heeger, J. Phys. Rev. Lett. 1979, 42, 1698.

[32] J.-L. Brédas, G. B. Street, Acc. Chem. Res. 1985, 18, 309.

[33] S. Gunes, H. Neugebauer, N. S. Sariciftci, *Chem. Rev.* **2007**, *107*, 1324.

[34] A. J. Heeger, *Adv. Mater.* **2014**, *26*, 10.

[35] Y. Yu, J. Gao, J. C. Hummelen, F. Wudl, A. J. Heegre, *Science* **1995**, *270*, 1789.

[36] J. Urieta-Mora, I. Garcia-Benito, A. Molina-Ontoria and N. Martin, Chem. Soc. Rev., 2018, 47, 8541–8571.

[37] C. H. Teh, R. Daik, E. L. Lim, C. C. Yap, M. A. Ibrahim, N. A. Ludin, K. Sopian and M. A. Mat Teridi, J. Mater.Chem. A, 2016, 4, 15788–

15822.

[38] I. Gelmetti, N. F. Montcada, A. Perez-Rodriguez, E. Barrena, C. Ocal, I. Garcia-Benito, A. Molina-Ontoria, N. Martin, A. Vidal-Ferran and E. Palomares, Energy Environ. Sci., 2019, 12, 1309–1316.

[39] X. Zhao and M. Wang, Mater. Today Energy, 2018, 7, 208–220.

[40] W.-J. Chi, Q.-S. Li and Z.-S. Li, Nanoscale, 2016, 8, 6146–6154.

[41] B. Pashaei, H. Shahroosvand, M. Ameri, E. Mohajerani and M. K. Nazeeruddin, J. Mater. Chem. A, 2019, 7, 21867–21873.

[42] J. Urieta-Mora, I. Garcia-Benito, I. Zimmermann, J. Arago, A. Molina-Ontoria, E. Orti, N. Martin and M. K. Nazeeruddin, J. Org. Chem., 2020, 85, 224–233.

[43] S. Maddala, C.-L. Chung, S.-Y. Wang, K. Kollimalayan, H.-L. Hsu, P. Venkatakrishnan, C.-P. Chen and Y. J. Chang, Chem. Mater., 2020, 32, 127–138.

[44] P. Xu, P. Liu, Y. Li, B. Xu, L. Kloo, L. Sun and Y. Hua, ACS Appl. Mater. Interfaces, 2018, 10, 19697–19703.

[45] Z. Hawash, L. K. Ono, S. R. Raga, M. V. Lee and Y. Qi, Chem. Mater., 2015, 27, 562–569.

[46] E. J. Juarez-Perez, M. R. Leyden, S. Wang, L. K. Ono, Z. Hawash and Y. Qi, Chem. Mater., 2016, 28, 5702–5709.

[47] U. Bach, D. Lupo, P. Comte, J. E. Moser, F. Weissortel, J. Salbeck, H. Spreitzer and M. Gratzel, Nature, 1998, 395, 583–585.

[48] A. Binek, M. L. Petrus, N. Huber, H. Bristow, Y. Hu, T. Bein and P. Docampo, ACS Appl. Energy Mater., 2016, 8, 12881–12886.

[49] (a) C. Yin, J. Lu, Y. Xu, Y. Yun, K. Wang, J. Li, L. Jiang, J. Sun, A. D. Scully, F. Huang, J. Zhong, J. Wang, Y.-B. Cheng, T. Qin and W. Huang, 2018, 8, 1800538. (b) Y.-K. Wang, Z.-C. Yuan, G.-Z. Shi, Y.-X. Li, Q. Li, F. Hui, B.-Q. Sun, Z.-Q. Jiang and L.-S. Liao, 2016, 26, 1375-1381.

[50] C. A. Di, Y. Q. Liu, G. Yu, D. B. Zhu, Acc. Chem. Res. 2009, 42, 1573.

[51] C. Reese, W.-J. Chung, M. Ling, M. Roberts, Z. Bao, Appl. Phys. Lett. 2006,

89, 202108.

[52] H. Moon, R. Zeis, E.-J. Borkent, C. Besnard, A. J. Lovinger, T. Siegrist, C. Kloc, Z. Bao, J. Am. Chem. Soc. 2004, 126, 15322.

[53] J. E. Anthony, Chem. Rev. 2006, 106, 5028

[54] J. Soeda, Y. Hirose, M. Yamagishi, A. Nakao, T. Uemura, K. Nakayama, M. Uno, Y. Nakazawa, K. Takimiya, J. Takeya, Adv. Mater. 2011, 23, 3309.

[55] Y. Yuan, G. Giri, A. L. Ayzner, A. P. Zoombelt, S. C. B. Mannsfeld, J. Chen, D. Nordlund, M. F. Toney, J. Huang, Z. Bao, Nat. Commun. 2014, 5, 3005.

[56] J. F. Morin, N. Drolet, Y. Tao, M. Leclerc, Chem. Mater. 2004, 16, 4619.

[57] N. Drolet, J. F. Morin, N. Leclerc, S. Wakim, Y. Tao, M. Leclerc, Adv. Funct. Mater. 2005, 15, 1671.

[58] H. Jiang, H. Zhao, K. K. Zhang, X. Chen, C. Kloc, W. Hu, Adv. Mater. 2012, 23, 5075.

[59] P. L. T. Boudreault, S. Wakim, N. Blouin, M. Simard. C. Tessier, Y. Tao, M. Leclerc, J. Am. Chem. Soc. 2007, 129, 9125.

[60] P. L. T. Boudreault, S. Wakim, M. L. Tang, Y. Tao, Z. Bao, M. Leclerc, J. Mater, Chem.2009, 19, 2921.

[61] C. Wang, H. Dong, W. Hu, Y. Liu and D. Zhu, Chem. Rev.,2012, 112, 2208–2267.

[62] B. Meng , Y. Fu , Z. Xie , J. Liu and L. Wang , Macromolecules, 2014, 47 , 6246

[63] T. Lei , J. Y. Wang and J. Pei , Chem. Mater., 2014, 26 , 594

[64] J. Mei and Z. Bao , Chem. Mater., 2014, 26 , 604

[65] B. Meng , H. Song , X. Chen , Z. Xie , J. Liu and L. Wang , Macromolecules, 2015, 48 , 4357

[66] B. X. Dong , C. Nowak , J. W. Onorato , J. Strzalka , F. A. Escobedo , C. K. Luscombe , P. F. Nealey and S. N. Patel , Chem. Mater., 2019, 31 , 1418

[67] S. Torabi , F. Jahani , I. Van Severen , C. Kanimozhi , S. Patil , R. W. A. Havenith , R. C. Chiechi , L. Lutsen , D. J. M. Vanderzande , T. J. Cleij , J. C. Hummelen and L. J. A. Koster , Adv. Funct. Mater., 2015, 25 , 150

[68] S. Torabi , F. Jahani , I. Van Severen , C. Kanimozhi , S. Patil , R. W. A. Havenith , R. C. Chiechi , L. Lutsen , D. J. M. Vanderzande , T. J. Cleij , J. C. Hummelen and L. J. A. Koster , Adv. Funct. Mater., 2015, 25 , 150

[69] I. Cho, S. K. Park, B. Kang, J. W. Chung, J. H. Kim, K. Cho and S. Y. Park, Adv. Funct. Mater., 2016, 26, 2966

[70] I. Cho, N. J. Jeon, O. K. Kwon, D. W. Kim, E. H. Jung, J. H. Noh, J. Seo, S. I. Seok, S. Y. Park, Chem. Sci., 2017, 8 (1), 734

[71] I. Cho, Jeon, N. J.; Kwon, O. K.; Kim, D. W.; Jung, E. H.; Noh, J. H.; Seo, J.; Seok, S. I.; S. Y. Park, Chem. Sci., 2017, 8 (1), 734

[72] M. J. Sung, N. G. An, C. Wang, Y. Kim, J. Y. Kim, S. Kwon., Dyes and Pigments, 2019, 161, 419

Chapter 2.

Engineering length of ethylene glycol chains on indolo [3,2-b] indole-based small molecules as dopant-free hole transporting materials for inverted (p-i-n) and conventional (n-i-p) perovskite solar cells

2.1 Introduction

Recently, perovskite solar cells (PSCs) are fast becoming one of the most reliable options to meet the demand for future photovoltaic devices owing to their promising optical and electronic properties.[1-3] As a result, a general PSC frame can be classified as an existing conventional (*n-i-p*) and inverted (*p-i-n*) architecture. Conventional PSCs have exceeded the power conversion efficiencies (PCEs) over 25 % in a few years. However, this architecture must be made using complex preparation for the metal oxide scaffold layer and high-temperature annealing. In addition, it is well known that device stability is still a significant issue, as hygroscopic dopants are highly required in hole transporting layer (HTL) for high performance.[4-9] On the other hand, inverted PSCs are also receiving considerable attention because of their low temperature production and device stability compared to conventional PSCs. [10-13] However, the inverted PSCs underperform conventional PSCs due to the relatively

smaller open circuit voltage (V_{oc}) and fill factor (FF) contributed by the interface between the perovskite and the HTL.[14-18] Thus, the development of suitable hole transporting materials (HTMs) ensuring the above features in the currently considered PSCs still represents a crucial step towards extending their wide use in attaining higher PCEs with enhanced environmental stability characteristics.[19-21]

To develop high performance inverted and conventional PSCs, numerous studies, including various perovskite layers and hole transporting materials (HTM), have been extensively conducted up to now.[22-25] However, their widespread utilization of the PSCs still need to be restricted by insufficient characteristics observed in various HTMs. Thus, one essential prerequisite is the development of prominent HTMs suitable for their use in PSCs. At first, the HTMs in the inverted PSCs have been believed to serve as an interlayer between the perovskite layer and the bottom electrode. Thus, the dense HTMs are highly demanded because of the unintended invasion of moisture or oxygen between the perovskite layer and bottom electrode during device operation. Moreover, the HTM should ensure high thermal stability characteristics because the quality of the perovskite layer is highly dependent on the post-annealing process.[26] In this regard, solving thermal stability in HTMs also represents one key approach for extending practical use in an inverted PSC,

with smooth morphology, suitable energy level, good solubility, and enhanced hole mobility.

To date, the widely adopted inverted HTM in the inverted PSCs is the poly(3,4-ethylenedioxythiophene):poly(styrenesulfonate)(PEDOT:PSS). But, the PEDOT: PSS still exhibited inconsistent energy levels, large batch-to-batch variation, and intrinsic acidity, thus causing insufficient efficiency and instability features.[27-31] Therefore, one promising approach for improved device performance in the inverted PSCs is to use dopant-free organic small molecule HTMs. Unlike polymeric HTMs, organic small molecule HTMs have significant advantages in reproducibility, processability, tunable energy levels, and improved stability.[32-35]

Second, the HTMs in the conventional PSCs, 2,2,7,7-tetrakis-(N,N-di-p-methoxy-phenyl-amine)9,9spiro-bifluorene (Spiro-OMeTAD) have shown promise as one of the most effective and widely used HTM molecules. However, this HTM has the disadvantage of adapting several dopants, such as lithium bis (trifluoromethanesulfonyl) imide (Li-TFSI) and 4-tert-butylpyridine (4-tBP) owing to the low hole mobility of the undoped Spiro-OMeTAD.[36-38] It is widely believed that the above dopants had significant impacts on device degradation; for example, the hygroscopic nature of Li-TFSI easily absorbed the air, thereby providing quick decomposition of the perovskite film. The

strong polar nature of 4-tBP was likely linked with the rapid corrosion of the perovskite layer by the formation of other complexes with PbI_2.

Given the abovementioned dopant issues, various dopant-free triphenylamine (TPA) based HTMs, and planar type HTMs have been extensively investigated for the past years as they have exhibited enhanced device characteristics.[39] TPA based and planar type HTMs were primarily designed to improve the intermolecular interaction by replacing the orthogonal spiro cores with rigid p-type backbone. In general, the TPA-based HTMs employed the bulky functional groups of TPA derivatives working as an end-capping group due to the better solubility and suppressing intermolecular π–π interactions to prevent molecular crystallization, favoring the formation of high-quality thin films.

To address such issues, a planar type HTM with a proper solubility and crystallinity characteristic has been the subject as a crucial way to attain further outstanding hole mobility and uniform film morphology to serve as an effective protecting layer possibly enabled by their tight molecular packing nature. In our previous approaches, we reported the conventional (*n-i-p*) PSCs based on the planar type HTM of IDIDF.[40] The device with the doped IDIDF provided the PCE (19.8%) because of their rigid molecular structures. However, the utilization of IDIDF HTM has still been limited by relatively rough morphology

governed by insufficient solubility and the inherent use of dopants necessary for enhanced mobility. Therefore, intentional manipulation of solubility and crystallinity is one promising way to achieve high device performance because both features are expected to have intrinsic trade-off characteristics.

Our essential concept of this work is to adapt oligo(ethylene) glycol chains (OEG) at *N*-positions of the fluroniated IDID core to enhance solubility regarding efficient device fabrication and obtain further tight molecular packing that directly relates to charge transport characteristics. Thus, the diethylene glycol (DEG) and tri-ethylene glycol (TEG) side chains are chosen to construct tight molecular stacking features for advancing mobility without impacting its original backbone structures, which is denoted as the DEG-IDIDF and TEG-IDIDF in this work. The DEG-IDIDF exhibited proper solubility in common organic solvents for inverted perovskite solar cells; however, it did not show sufficient solubility to cover the perovskite surface in conventional PSCs. On the other hand, the TEG-IDIDF exhibited sufficient solubility to cover the perovskite surface in conventional PSCs owing to relatively longer OEG side chains; however, its melting temperature is slightly lower than 100 °C; thus, the TEG-IDIDF could not use in HTL for inverted PSCs. As such, the inverted $MAPbI_3$ based PSCs containing the DEG-IDIDF HTM yielded a PCE of 16.60 %. In particular, the PSCs devices confirmed stable

characteristics, which might be owing to their tight molecular packing crystalline features induced by close π–π interaction between the planar structures in film states. The PSCs maintained 80 % performance of their initial PCEs over 500 hours despite being annealed at 60 °C. The conventional $MAPbI_3$ based PSCs devices, including the TEG-IDIDF, gave an outstanding PCE of 18.09 % when $FAPbI_3$ based PSCs devices with TEG-IDIDF exhibited superior PCEs of doped (22.71%) and non-doped (20.42%) without a rapid degradation originally present in PSC during exposure to humidity. The long humidity-resistant crystallinity nature of TEG-IDIDF that possibly comes from the tight molecular packing with strong π–π interaction between the planar structures is likely ascribed to an enhancement in device stability for longer 50 days.

2.2 Experimental

Synthesis:

As seen in Scheme 2-1, the fluorinated IDID core is synthesized, according to the following procedures. All reagents used in the experimental systhesis process are purchased at Sigma Aldrich, TCI, and Alfa Aesar unless otherwise stated.

5-Fluoro-2-nitroaniline (2).

500mL two-necked round-bottom flask, with a magnetic stirrer bar and a reflux condenser, was filled with 350mL of acetic acid (AcOH) and 5-Fluoro-2-nitrobenzene (35.00 g, 194.32 mmol), N-bromosuccinimide (35.82 g, 203.54 mmol). The reaction mixture was stirred for 3 hours. The reaction was poured into 1000mL of H_2O. The yellow powder were filtrated and washed with H_2O (2000 mL x 2) to afford 2 (40.2 g, yield 89.35%). ^{1}H-NMR (300 MHz, $CDCl_3$, δ): 8.39 (d, J ¼ 7.08 Hz, 1H), 6.60 (d, J ¼ 9.60 Hz, 1H), 6.1963 (s, 2H).

1-bromo-2-fluoro-4-iodo-5-nitrobenzene (3).

5-Fluoro-2-nitroaniline (2) (30.00 g, 127.65 mmol) was dissolved in H_2O (40 mL), AcOH (120 mL), and H_2SO_4 (80 mL) mixed solution at 0 ºC. Furthermore, slowly added $NaNO_2$ solution (9.69 g, 139.5 mmol, in 30 mL of H_2O) was

added dropwise slowly, using a dropping funnel. After Stirring for an hour, KI solution (25.425 g, 153 mmol, in 30 mL of H_2O) was dropped slowly and then the mixture was heated to 60 ºC for 3 hours, cool down to 0 ºC. With an ice bath, the reaction mixture was poured into $NaHCO_3$ (400mL) and methylene chloride (600mL). The product was washed with H_2O and dried over $MgSO_4$, filtered. Finally, the product was recrystallized to afford 3 as an orange crystal (13 g, yield 61.14%). ^{1}H-NMR (300 MHz, $CDCl_3$, δ): 8.18 (d, J ¼ 6.21 Hz 1H), 7.81 (d, J ¼ 7.35 Hz, 1H).

(4-bromo-5-fluoro-2-nitrophenyl)ethynyl)trimethylsilane (4).

1-bromo-2-fluoro-4-iodo-5-nitrobenzene(3)(8g,20.38mmol), bis(triphenylphos phine)palladium(II)dichloride (1.4g, 2.02 mmol), and copper(I) iodide (800 mg, 4.3 mmol) was dissolved in THF with a 250mL two-neck round-bottom flask in argon (Ar) gas. The trimethylsilylacetylene (2.1 g, 20.5 mmol), and trimethylamine (13 mL) were slowly added and stirring 3 hours at room temperature. The reaction mixture was poured through a silica plug. The concentrated filtrate was purified by column chromatography (ethyl acetate (EA)/n-hexane 1 : 4, v/v) to afford 4 as a brown oil (6.7 g, yield 71.2%). ^{1}H-NMR (300 MHz, $CDCl_3$, δ): 8.31 (d, J ¼ 6.24 Hz, 1H), 7.38 (d, J ¼ 8.19 Hz, 1H), 0.28 (s, 9H).

1-bromo-4-ethynyl-2-fluoro-5-nitrobenzene (5).

((4-bromo-5-fluoro-2-nitrophenyl)ethynyl)trimethylsilane(4) (4.3g,17.3mmol), K_2CO_3 (2.3 g, 17.86 mmol), 18-crown-6 (0.39 g 1.75 mmol) were dissolved in methylene chloride (25 mL), H_2O (13 mL), and acetone (6mL) and stirring 3 hours at room temperature. The reaction mixture was extracted with methylene chloride (500mL) and washed with brine (250 mL x 2).The product was purified by column chromatography (EA/n-hexane 1 : 4, v/v) to afford 5 as a yellow brown powder (1.29 g, yield 75.57%). ^{1}H-NMR (300 MHz, $CDCl_3$, δ): 8.36 (d, J ¼ 6.24 Hz, 1H), 7.43 (d, J ¼ 8.04 Hz, 1H), 3.64 (s, 1H).

1,2-bis(4-bromo-5-fluoro-2-nitrophenyl)ethyne (6).

1-bromo-2-fluoro-4-iodo-5-nitrobenzene (3) (4 g, 13.21 mmol), 1-bromo-4-ethynyl-2-fluoro-5-nitrobenzene (5). (2.9 g, 14.30 mmol), bis(triphenylphosphine)palladium(II) dichloride (0.48g, 0.78 mmol), and copper(I) iodide (0.23g, 1.36 mmol) were dissolved in THF (32 mL) and triethylamine (12 mL). The reaction mixture was extracted with chloroform and was purified by the flash column chromatography. The product was recrystallized with EA solvent afforded compound 6 as a brown solid (2.93 g, yield 57.38%). ^{1}H-NMR (300 MHz, $CDCl_3$, δ): 8.47 (d, J ¼ 6.18 Hz, 2H), 7.56 (d, J ¼ 7.86 Hz, 2H).

1,2-bis(4-bromo-5-fluoro-2-nitrophenyl)ethane- 1,2-dione (7).

Potassium permanganate (3.18 g, 14.65 mmol) and Adogen 464 (few drops) were dissolved in H_2O (30 mL), methylene chloride (35 mL), and AcOH (1.7 mL). After stirring 3 hours in Ar gas, the 1,2-bis(4-bromo-5-fluoro-2-nitrophenyl)ethyne (6) (2.34 g, 4.32 mmol) was added and refluxed for 12 hours. The reaction mixture was poured into H_2O (300 mL) with $NaHSO_3$, and extracted with methylene chloride . The organic phase was separated, washed with water and purified by column chromatography (EA/n-hexane 1 : 9, v/v) to afford 7 as a yellow crystalline solid (1.78 g, yield 81.23%). ^{1}H-NMR (300 MHz, $CDCl_3$, δ): 8.55 (d, J ¼ 5.61 Hz, 2H), 7.4 (d, J ¼ 6.93 Hz, 2H).

2,7-dibromo-3,8-difluoro-5,10-dihydroindolo [3,2-b]indole (8).

1,2-bis(4-bromo-5-fluoro-2-nitrophenyl)ethane-1,2-dione (7) (1.8 g, 3.4 mmol) was dissolved in AcOH (13 mL) and then, the stannous chloride (13.6 g, 78.6 mmol), acetic acid (20 mL), and 1 N HCl (21 mL) mixed solution was added and refluxed for 6 hours at 65 ºC. The product was washed with acetic acid, 1 N HCl, water, and ethanol and purified by the flash column chromatography (EA/n-hexane 1 : 4 v/v). Finally, the purified product was washed with chloroform (300 mL), filtered, and afford 8 as a light brown solid (1.3 g, yield 82.10%). ^{1}H-NMR (300 MHz, acetone-*d6*, δ): 10.47 (s, 2H), 7.84 (d, J ¼ 5.88 Hz, 2H), 7.67 (d, J ¼ 9.36 Hz, 2H).

2,7-dibromo-3,8-difluoro-5,10-bis(2-(2-(2-methoxyethoxy)ethoxy)ethyl)-4b,5,9b,10-tetrahydroindolo[3,2-b]indole (9-1).

2,7-dibromo-3,8-difluoro-5,10-dihydroindolo [3,2-b]indole (8) (0.3g, 1.1 mmol) was dissolved in anhydrous THF (25 mL) in Ar gas and then NaH (0.13 g, 4.5 mmol) was added. After stirring 1 hour, 1-((2-(2-(2-methoxyethoxy) ethoxy)ethyl)sulfonyl)-4-methylbenzene (1.0 g, 6.43 mmol) was added to the reaction mixture and refluxed for over 12 hours. The reaction mixture extracted with methylene chloride and purified by flash column chromatography (EA/n-hexane 1 : 4, v/v) and recrystallization (EA) to afford 9 as a white crystalline solid (0.43 g, yield 75.94%). ^{1}H-NMR (300 MHz, $CDCl_3$, δ): 7.66(m, 3H) 4.56(t, J ¼ 6 Hz 2H), 3.92 (t, J ¼ 6 Hz 2H), 3.51 (m, 12H), 3.51 (s, 6H).

3,8-difluoro-2,7-bis(5'-hexyl-[2,2'-bithiophen]-5-yl)-5,10-bis(2-(2-methoxyethoxy)ethyl)-5,10-dihydroindolo[3,2-b]indole (DEG-IDIDF)

2,7-dibromo-3,8-difluoro-5,10-bis(2-(2-methoxyethoxy)ethyl)-5,10-dihydroindolo[3,2-b]indole (9-1) (320 mg, 0.94 mmol), 50-hexyl-2,20-bithiophene-5-boronic acid pinacol ester (520 mg, 1.69 mmol), and tetrakis(triphenylphosphine) palladium(0) (110 mg, 0.09 mmol) were dissolved in THF (35 mL), and then 2 N NaOH aqueous solution (12 mL) were added and refluxed at 60 ºC in an Ar atmosphere for 24 hours. The reaction mixture

was neutralized (1 N HCl), and extracted with Chloroform. The product was purified by column chromatography (chloroform/n-hexane 1 : 2, v/v) and recrystallization (EA 8:Hex 2) to afford DEG-IDIDF as orange crystals (330 mg, yield 63.12%). 1H-NMR (500 MHz, tetrahydrofuran-d8, d): 7.86(d, J ¼ 6.5 Hz 1H) 7.77(d, J ¼ 12 Hz 1H) 7.47(d, J ¼ 3 Hz 1H) 7.15(d, J ¼ 3 Hz 1H) 7.07(d, J ¼ 3.5 Hz 1H) 6.74(d, J ¼ 3.5 Hz 1H) 4.72(t, J ¼ 5Hz 2H), 3.95(t, J ¼ 5.5 Hz 2H), 3.49(t, J ¼ 6Hz 2H), 3.41(t, J ¼ 3.5 Hz 2H) 3.15(s, 3H) 2.84 (t, J ¼ 8 Hz 2H), 1.69 (m, 2H), 1.36 (m, 6H), 0.92(t, J ¼ 4.5 Hz 3H). HRMS (FAB+, m-NBA): calcd for 942.34; found, 942.32.

2,7-dibromo-3,8-difluoro-5,10-bis(2-(2-(2-methoxyethoxy)ethoxy)ethyl)-4b,5,9b,10-tetrahydroindolo[3,2-b]indole (9-2).

A 100 mL two-necked RBF, equipped with a magnetic stirrer bar and reflux condenser was baked under a reduced pressure and backfillled with Ar (x3). 2,7-dibromo-3,8-difluoro-5,10-dihydroindolo [3,2-b]indole (8) (380 mg, 0.95 mmol), anhydrous THF (20 mL), and NaH (91.20 mg, 3.79 mmol) were added to the baked reaction vessel. After 10 minutes at room temperature (RT), 1-((2-(2-(2- methoxyethoxy) ethoxy)ethyl) sulfonyl)-4-methylbenzene (627 mg, 3.79 mmol) was added to the reaction mixture. After that, the reaction mixture was gently refluxed for 24 hours. After reaction completion, the reaction mixture

was poured into brine (200 mL) and extracted with DCM. The organic layer was separated, washed (water, 200 mL x 3), dried with MgSO4,and concentrated, sequentially. The resulting crude product was purified by the flash column chromatography (EA/n-hexane 1 : 9, v/v) and recrystallization (EA) to afford 2 as a white crystalline solid (410 mg, yield 75.94%). 1H-NMR (300 MHz, CDCl3, δ): 7.66(m, 3H) 4.56(t, J ¼ 6 Hz 2H), 3.92 (t, J ¼ 6 Hz 2H), 3.51 (m, 12H), 3.51 (s, 6H).

3,8-difluoro-2,7-bis(5'-hexyl-[2,2'-bithiophen]-5-yl)-5,10-bis(2-(2-(2-methoxyethoxy)ethoxy)ethyl)-5,10-dihydroindolo[3,2-b]indole (TEG-IDIDF).

2,7-dibromo-3,8-difluoro-5,10-bis(2-(2-(2-methoxyethoxy)ethoxy)ethyl)-4b,5,9b,10-tetrahydroindolo[3,2-b]indole **(9-2)** (650 mg, 1.14 mmol), 50-hexyl-2,20- bithiophene-5-boronic acid pinacol ester (904 mg, 2.40 mmol), tetrakis(triphenylphosphine)palladium(0) (132 mg, 0.11 mmol), THF (30 mL), and 2 N NaOH aqueous solution (15 mL) were added to a 100 mL two-necked RBF, equipped with a magnetic stirrer bar and reflux condenser. The reaction mixture was gently refluxed at 80 ºC in an Ar atmosphere. After 24 hours, the reaction mixture was quenched with H2O (300 mL), neutralized (1 N HCl), and extracted with DCM. The combined organic phase was dried with MgSO4 and concentrated under reduced pressure. The crude product was purified by flash

column chromatography (chloroform/n-hexane 1 : 8, v/v) and recrystallization (EA) to afford TEG-IDIDF as orange crystals (760 mg, yield 73.23%). 1H-NMR (500 MHz, tetrahydrofuran-d8, d): 7.64(d, J ¼ 6 Hz 2H) 7.62(s, 2H) 7.41(d, J ¼ 1.5 Hz 2H) 7.14(d, J ¼ 6 Hz 2H) 7.05(d, J ¼ 3.5 Hz 2H) 6.71(d, J ¼ 3.5 Hz 2H) 4.64(t, J ¼ 5.5Hz 4H), 3.98(t, J ¼ 5.5 Hz 4H), 3.56(m, 32H), 3.29(s, 6H) 2.81 (t, J ¼ 8 Hz 4H), 1.71 (m, 4H), 1.35 (m, 12H), 0.91(t, J ¼ 4.5 Hz 6H).

Materials:

Indium tin oxide glass substrate with a sheet resistance of 15Ω sq^{-1} were purchased from AMG tech (Korea). $PC_{60}BM$ were purchased from Nano-C and Lumtech. PbI_2 (99.999%) and solvents (chlorobenzene, dimethyl sulfoxide, dimethylformamide, and diethyl ether) were purchased from Alfa Aesar and Sigma-Aldrich respectively.

Characterization of HTMs: $^{1}H-NMR$ and $^{13}C-NMR$ spectra were recorded on an Avance 500 spectrometer (Bruker BioSciences Korea Co. Ltd.). High resolution mass spectra were taken by the JMS-700 (JEOL, Japan) instrument in FAB mode. Elemental analyses were recorded with the Flash 2000 (Thermo Fisher Scientific, Germany). The differential scanning calorimeter (DSC) measurements were carried out using a PerkinElmer DSC7 with a TAC 7/DX

instrument controller at the heating and cooling rate of 10 °C min^{-1}. The thermogravimetric analysis (TGA) was performed by increasing the temperature from 30 to 600 °C with a rate of 10 °C min^{-1} using Discovery TGA (TA instruments) in the N_2 atmosphere. Cyclic voltammetry measurements were performed using a 273A (Princeton Applied Research) with a one-compartment platinum working electrode, a silver wire, a platinum wire counter-electrode, and the IDID derivatives were spin-coated indium-tin-oxide (ITO) glass as a reference electrode. Measurements were performed in a 0.5×10^{-3} M acetonitrile solution with 0.1 M tetrabutylammonium tetrafluoroborate as supporting electrolyte at a scan rate of 50 mV s^{-1}. Each oxidation potential was calibrated using ferrocene as a reference. LUMO levels were evaluated with the HOMO level and the optical band gap, which was obtained from the edge of the film absorption spectra. The UV/Vis absorption spectra were monitored with the Lambda 1050 spectrometer (Perkin Elmer). Single crystal of DEG-IDIDF was grown from its dilute solution in mixed methanol and Ethylene Acetate via slow evaporation of solvent and characterized on a PHOTON 100 CMOS Detector (Large 100cm^2-active area / High sensitivity) using graphite monochromated Mo/Kα radiation (λ = 0.71073 Å) at a temperature of 293 K.

Device fabrication (inverted Perovskite solar cells):

The patterned indium tin oxide (ITO) glass substrates were cleaned by an ultrasonic treatment in deionized water, acetone, and isopropanol for each 25 min. After ultraviolet-ozone treatment for 30 min, The HTM were dissolve in CB solvent and then spin-coated at distinct spin-coating rate for 30 s, and then thermally annealed at different temperature for 10 min. A thin layer of PFN-Br was then spin-coated from a 0.5 mg mL^{-1} solution in anhydrous methanol at 5000 RPM for 30 s to increase the wettability on the HTM film. The perovskite solution was prepared by dissolving PbI_2:CH_3NH_3I (MAI) (1:1 molar ratio) into DMF:DMSO at 50 wt%. The film of $PC_{60}BM$ was formed by spin coating process (2000 rpm) and then the ZnO nanoparticle solution was spin-coated at 5000 rpm. Finally, an Ag electrode of 100 nm thickness was deposited by thermal evaporation under a vacuum of 10^{-6} Torr.

Device fabrication (conventional Perovskite solar cells):

The patterned indium tin oxide (ITO) glass substrates were wet-cleaned in an ultrasonic bath of deionized water, acetone, and isopropanol for each 20 min. After ultraviolet-ozone treatment for 30 min, the sol-gel ZnO solution was spin-coated at 3000 rpm and annealed at 200 °C for 10 min. The 40 nm of $PC_{60}BM$ was formed by spin coating process. The perovskite solution was prepared by

dissolving PbI_2 : CH_3NH_3I (MAI) into DMF:DMSO (1:1 molar ratio) at 50 wt%. During spin coating, 0.5ml of diethyl ether was dropped on substrate and annealed 65 ℃ for 1 min and 100 ℃ for 2 min. After cooling down to room temperature, Spiro-OMeTAD solution (72mg/ml in chlorobenzene) with 28.8 μL of 4-tBP and 17.5 μL (520mg/ml in acetonitrile) was spin-coated on the perovskite layer at 6000 rpm for 20s. Fore the case of the non-doped IDIDF based HTMs, an approximately 50 nm-thick film was prepared on the top of perovskite layer by spin coating. For the case of the doped IDIDF based HTM, a 100 nm-thick film was prepared by the same spin coating process. Finally, a gold electrode of 80 nm thickness was deposited by thermal evaporation under a vacuum of 10^{-6} Torr.

Out-of-plane XRD and Grazing Incidence Wide Angle X-ray Scattering (GIWAXS) measurements:

Out-of-plane XRD measurements were performed using a D8-advance X-ray diffractometer (Bruker Miller Co., Germany). GIWAX measurements were conducted at the 3C-SAXS I (X-ray E = 10.55 eV, λ = 1.121 Å) and PLS-II 9A U-SAXS beamline (X-ray E = 11.06 keV, λ = 1.121 Å) beamline in the Pohang Accelerator Laboratory (PAL) and a 2D charge-coupled device (CCD) detector (Mar165 CCD). The samples were mounted on a *z*-axis goniometer equipped

with a vacuum chamber (10^{-3} Torr), and the samples were loaded 0.201 m away from the CCD detector.

Characterization of Perovskite solar cell:

The *J–V* characteristics of PSCs were measured by using a Keithley 4200 source measurement unit. The solar cell performances were characterized under AM 1.5G conditions with an illumination intensity of 100 $mWcm^{-2}$, which was generated by the Oriel Sol3A solar simulator. The lamp irradiation was calibrated using a NREL certificated KG-5 filtered standard silicon photodiode (VLSI Standards Inc.). The active area was 0.05 cm^2, and measurements were carried out under an ambient atmosphere.

Hole mobility measurements:

The device architecture of ITO/PEDOT:PSS/HTM/MoO3/Ag was prepared for the hole mobilities measurement. The mobilities were obtained by the SCLC is described by:

$$J = \frac{9\varepsilon_0 \varepsilon_r \mu V^2}{8L^3}$$

ε_0, permittivity of free space; ε_r, relative permittivity of the material; μ, the hole mobility; L, thickness of the film.

SC-XRD:

CCDC 2213286 contains the supplementary crystallographic data for DEG-IDIDF. These data can be obtained free of charge from The Cambridge Crystallographic Data Centre

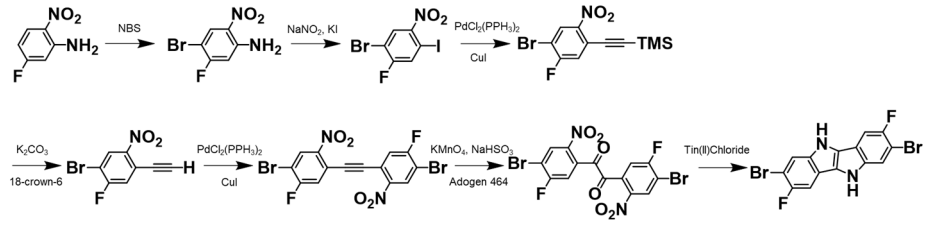

Scheme 2.1 chemical structures of DEG-IDIDF

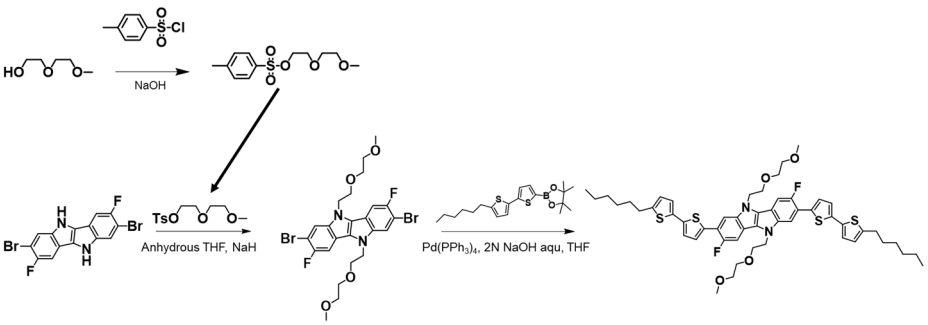

Scheme 2.2 chemical structures of DEG-IDIDF

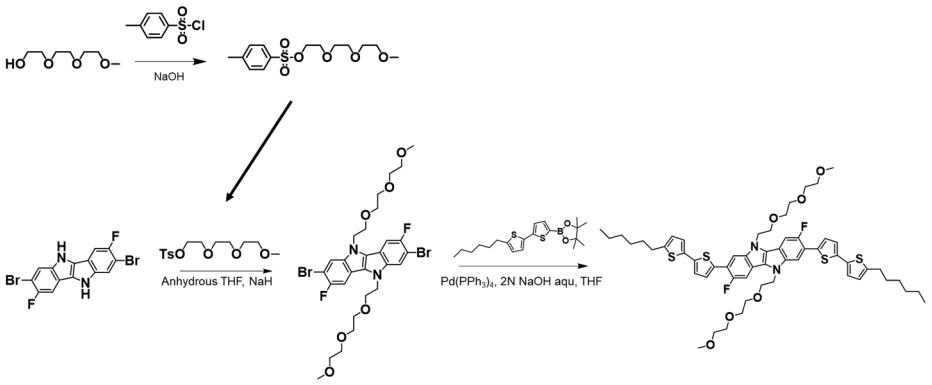

Scheme 2.3 chemical structures of TEG-IDIDF

2.3 Results and Discussion

2.3.1 inverted (*p-i-n*) perovskite solar cells

2.3.1.1 Optical, electrochemical, and thermal characteristics of DEG-IDIDF

The DEG side chains were substituted at *N*-positions, and the 5′ -hexyl-2,2′ -bithiophene units were substituted at the 2, 7-position of fluorinated IDID core, DEG-IDIDF (**Figure 2.1**). The DEG-IDIDF has excellent solubility in common organic solvents such as chlorobenzene and chloroform, thus providing solution processability. In addition, limiting solubility in polar solvents such as dimethylformamide and dimethyl sulfoxide is achieved, ensuring solution processability and high resistance to perovskite precursor solutions during the device fabrication process. The normalized UV-vis absorption spectra for DEG-IDIDF in chlorobenzene (CB) solution and thin films are shown in **Figure 2.2**. A π-π* transition of the absorption peak appeared at 440 nm for the solution, and the film displayed a spectrum at 509 nm. As expected, a large bathochromic shift (91 nm) was detected in the absorption spectrum with an additional peak. It seems to be due to the dense packing and planarization occurring in the highly ordered structure in the film state. DEG-IDIDF has an absorption peak in the visible region, but the

transmittance of DEG-IDIDF coated ITO remains >80% in the 400-550 nm range due to the use of a thin HTM film (12 nm) in the device. (**Figure 2.3**), thus ensuring negligible parasitic absorption loss.

The electrochemical properties of the IDID derivatives in the film state are monitored by cyclic voltammetry (CV) measurements (**Figure 2.4**). Although the attachment of the electron-donating OEG side chain increases the HOMO level (-5.13 eV), the HOMO level of the DEG-IDIDF compared to IDIDF (-5.22 eV) still favors efficient hole injection from the perovskite layer with respect to the valence band of the perovskite layer (-5.40eV). The onset of absorption calculates the optical band gap. The corresponding lowest occupied molecular orbital (LUMO) levels of DEG-IDIDF and IDIDF were -2.85 eV and -2.90 eV, respectively.

The thermal properties of DEG-IDIDF are determined by the differential scanning calorimetry (DSC) analyses (**Figure 2.5**). The resulting data is given in **Table 2.1**. The melting temperature (T_m) and cold crystallization temperature (T_c) values of DEG-IDIDF were 158 °C and 114 °C. These high thermal properties are beneficial for the advanced PCE of various inverted $MAPbI_3$ based PSCs because their PSCs require a thermal annealing process of around 100 °C.

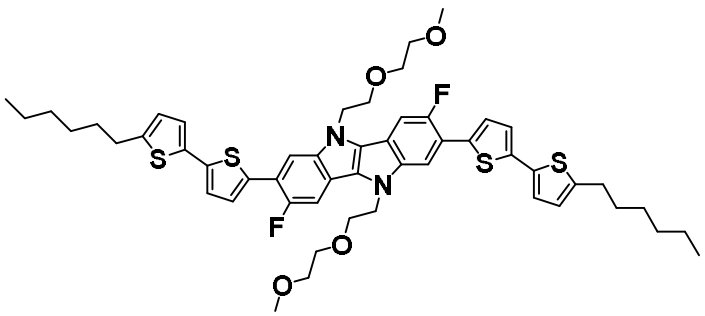

Figure 2.1 Chemical structures of DEG-IDIDF

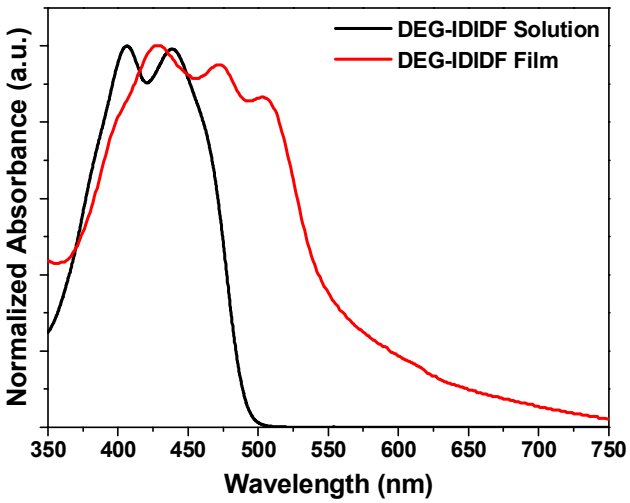

Figure 2.2 UV-vis absorption spectra of the DEG-IDIDF in solution and film states

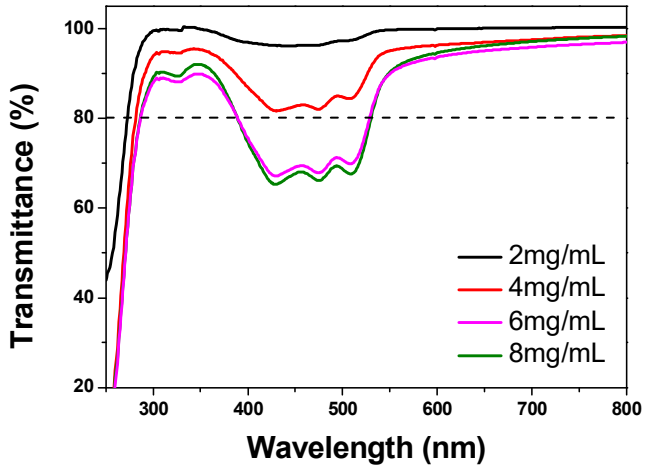

Figure 2.3 Transmittance dependence of DEG-IDIDF films on solution concentrations for film casting

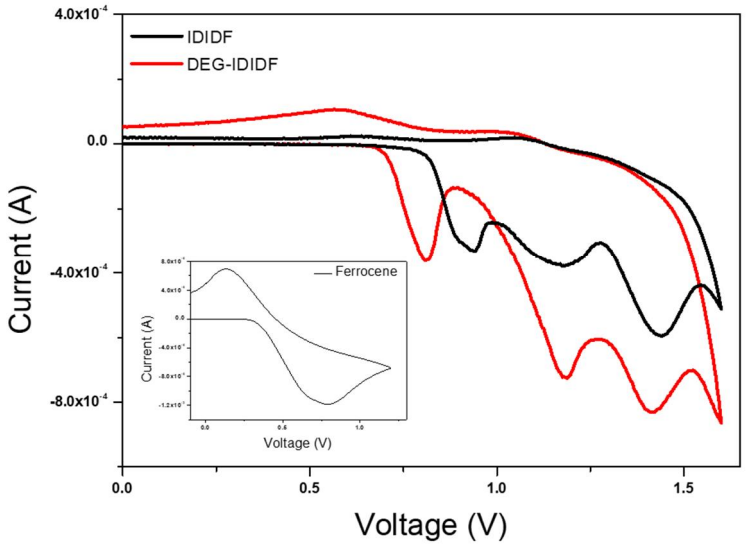

Figure 2.4 Cyclic voltammograms (CVs) of IDIDF and PEG-IDIDF (with ferrocene)

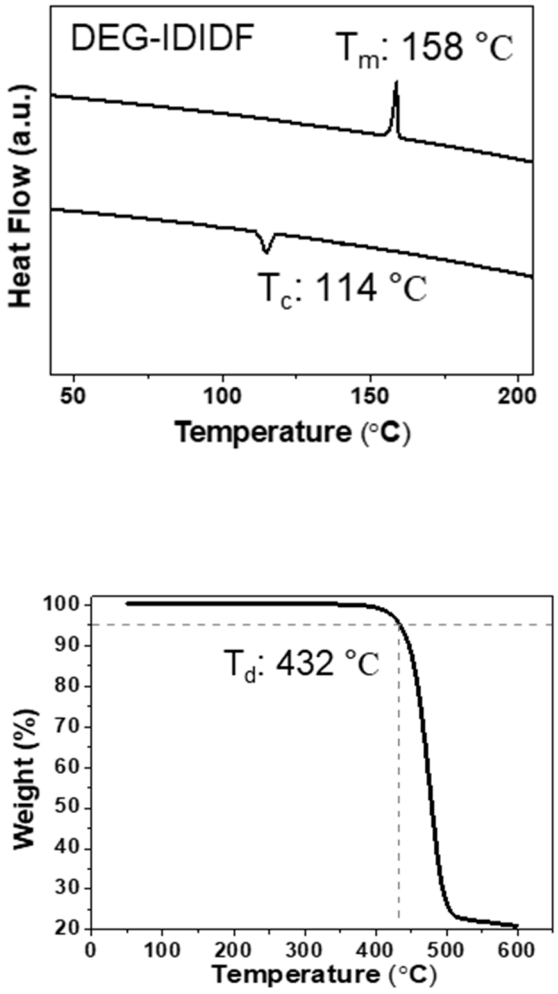

Figure 2.5 DSC and TGA curves of DEG-IDIDF

HTM	Abs.(Sol) $[nm]$	Abs.(Film) $[nm]$	HOMO(Film) $[eV]$	LUMO(Cal) $[eV]$	E_g $[eV]$
DEG-IDIDF	440	504	-5.13	-2.96	2.17

Table 2.1 Optical and electrochemical characteristics of the DEG-IDIDF

2.3.1.2 Structual Analyses of DEG-IDIDF

The molecular configuration and packing arrangement of DEG-IDIDF were investigated by single crystal analysis. **Figure 2.6** shows the intramolecular C F ••• H interactions in the DEG-IDIDF, leading to a planar molecular structure with a twist angle of 8.68° between the IDID backbone and thiophene. The molecular stacks of the DEG-IDIDF gave a relatively closer π–π distance 3.40 Å compared to the IDIDF (3.48 Å). These observations may be due to the presence of rigid π–π stacking in the DEG-IDIDF induced by the additional C H ••• C interaction between the flexible DEG side chains and IDID backbone. On the other hand, strong intermolecular interaction provides closer molecular stacking, giving advanced hole transporting properties in the device. Moreover, the devices, glass/ITO/HTMs and glass/ITO are prepared for the grazing incidence wide angle X-ray diffraction (GIWAXS) analyses to identify molecular orientation further and stacking in the film state. As shown in **Figure 2.7**, the device with DEG-IDIDF exhibited a distinct Bragg peak, corresponding to the high crystallinity of DEG-IDIDF, while the IDIDF revealed unclear peaks. In addition, two strong Bragg peaks in out-of-plane direction at q_z: 0.51 (d=12.38 Å) and 0.62 (d = 10.211 Å) were clearly shown without film annealing. Interestingly, the peak at q_z: 0.51 progressively reduced and disappeared when the annealing temperature was raised up to 120 °C;

however, the peak at q_z: 0.62 remained (**Figure 2.8**). Thus, the film of DEG-IDIDF clearly affected by annealing temperature and hole transporting properties.

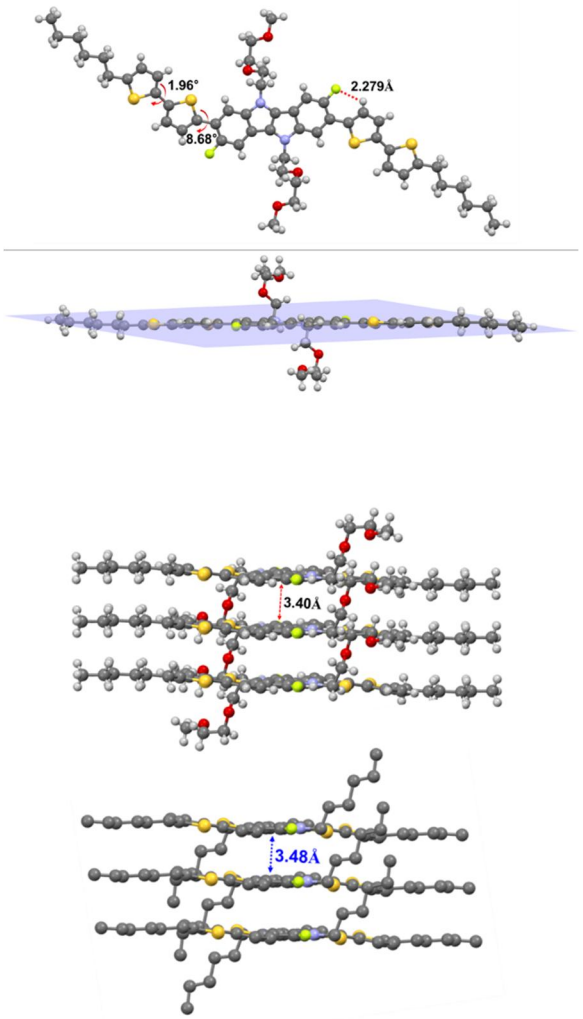

Figure 2.6 Single-crystal analysis of DEG-IDIDF and IDIDF

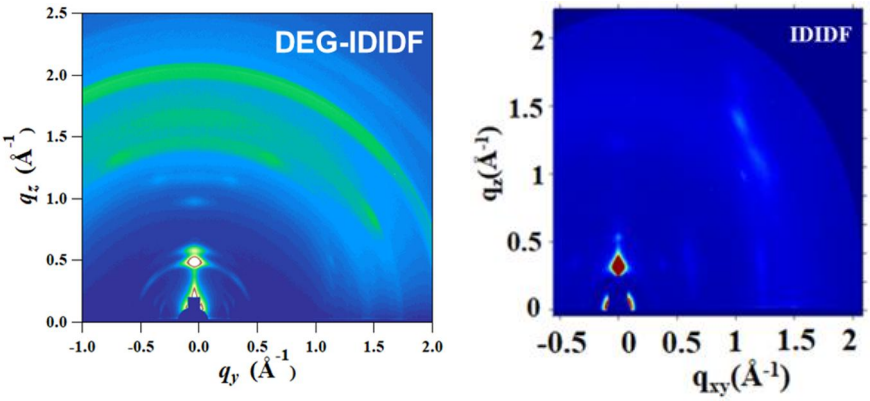

Figure 2.7 GIWAXS patterns of films of DEG-IDIDF and IDIDF

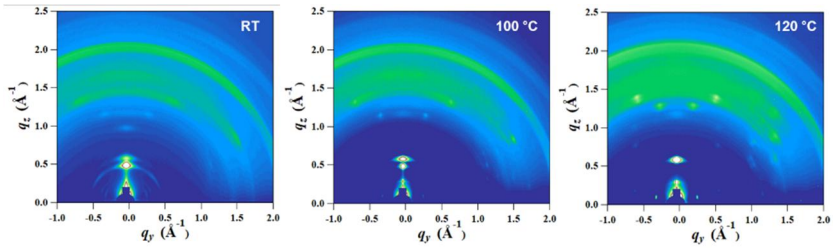

Figure 2.8 GIWAXS patterns of films of DEG-IDIDF with thermal annealing RT, 100 °C, and 120 °C

2.3.1.3 Charge transport property of HTMs

To further validate the hole transporting properties, the space-charge-limited current (SCLC), time-resolved PL measurements, and steady-state photoluminescence (PL) quenching were performed (**Figure 2.9**). The hole only devices were prepared for IDID derivatives, and the DEG-IDIDF (5.91×10^{-4} cm^2 V^{-1} s^{-1}) showed better hole mobility than IDIDF (3.35×10^{-4} cm^2 V^{-1} s^{-1}). Moreover, a significant decrease in PL emission was detected, and both DEG-IDIDF and IDIDF based devices confirmed a quenching efficiency of ~90%, indicating fast hole transporting properties at the HTM/Perovskite interface (**Figure 2.10**). In time-resolved PL analyses (**Figure 2.11**), the average lifetimes were calculated, and 128 ns, 4.3 ns, and 3.8 ns were obtained for the bare perovskite layer, IDIDF, and DEG-IDIDF, respectively. These findings support the superior hole extraction ability of DEG-IDIDF, which correlates with the enhancement of hole mobility driven by π–π stacked ordered structures in film state.

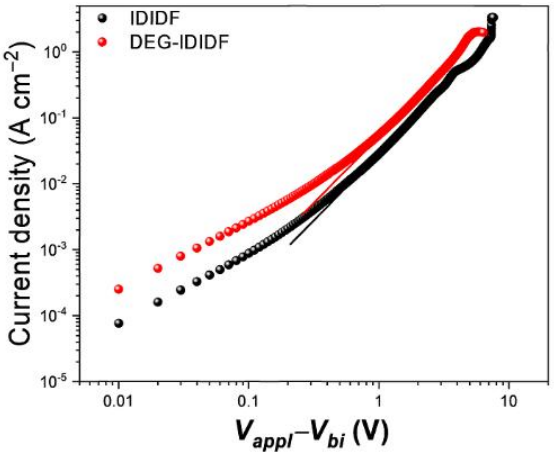

Figure 2.9 SCLC mobility of DEG IDIDF and IDIDF

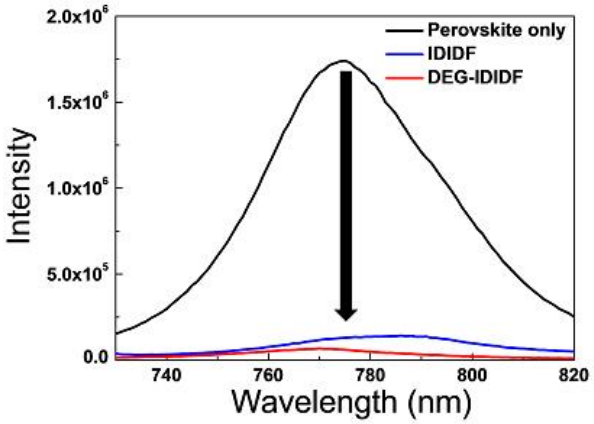

Figure 2.10 Steady-state PL spectra of IDID derivatives based perovskite films.

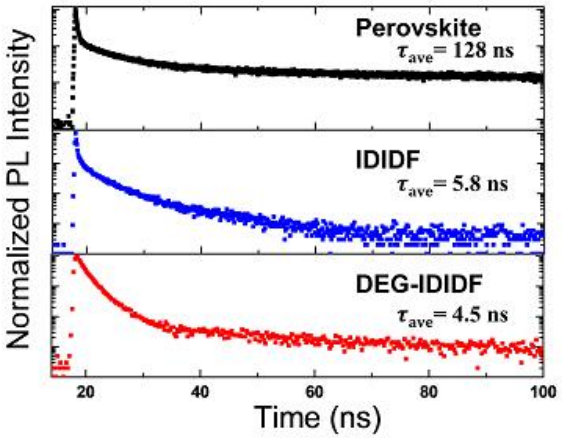

Figure 2.11 time-resolved PL spectra of IDID derivatives based perovskite films.

2.3.1.4 Characteristics of perovskite solar cell devices and device stability

The inverted PSCs were prepared with the structure of the glass/ITO/HTM/MAPbI3/PCBM/ZnO/Ag, when the HTMs were IDID derivatives and PEDOT:PSS for comparison. The device performance of the photovoltaic parameters were summarized in **Table 2.2** and **Figure 2.12**. All devices were prepared with systematic optimization of film thickness and annealing temperature of each HTMs. As expected, the PEDOT:PSS based PSCs exhibited the PCEs of 12.14 % owing to the aforementioned issues. Also, the IDIDF based PSCs yielded the PCEs of 12.72 % (V_{oc} = 1.08 V, J_{sc} = 18.83 mA cm^{-2}, and FF = 62%). On the other hand, the DEG-IDIDF-based PSC showed the highest PCE of 16.60 % with a V_{oc} of 1.04 V, short-circuit current density (J_{sc}) of 21.23 mA cm^{-2}, and FF of 75%. However, a slightly low V_{oc} was exhibited owing to a relatively high HOMO level compared to IDIDF, whereas enhancements in J_{sc} and FF were clearly observed. The result is primarily from better solubility and higher crystallinity properties leading to an ordered morphology from the film state. In addition, the thermal annealing analyses support that a dramatic enhancement in J_{sc} is in good agreement with the results observed from the GIWAXS analyses (**Table 2.3**). The average PCEs and the reverse and forward scans were shown in **Figure 2.13**. Also, the

integrated J_{sc} value (21.07 mA cm^{-2}) was calculated from the external quantum efficiency (EQE) spectra of the device and well matched (**Figure 2.14**). To identify the device air stability, humidity stability features of the encapsulated PSCs with each HTM were monitored for 240 hours under an ambient atmosphere at relative humidity (RH) of 35 ± 5%. The DEG-IDIDF and IDIDF PSC devices maintained 90% of their initial PCEs, while the PEDOT:PSS based PSC devices exhibited only 68% of their initial PCE. Moreover, the devices were tested under thermal stress at 60 °C. The DEG-IDIDF based PSCs maintained 80% of their initial efficiency for 500 hours (Figure 2.15). These experimental results suggest that DEG-IDIDF HTM could serve as a promising protective layer. This improvement in electrical and structural properties is believed to be owing to the above-mentioned high crystallinity properties induced by the introduction of flexible DEG side chains.

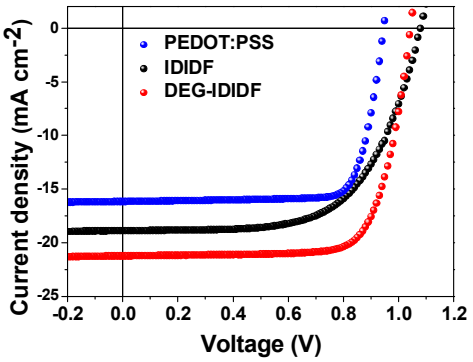

Figure 2.12 J-V characteristics of the best-performing devices with PEDOT:PSS, IDIDF, and DEG-IDIDF as HTMs

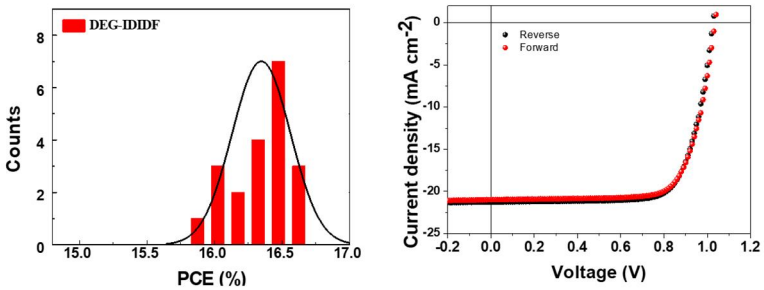

Figure 2.13 PCE histograms of over 20 devices and reverse and forward scans of the champion devices based on DEG-IDIDF

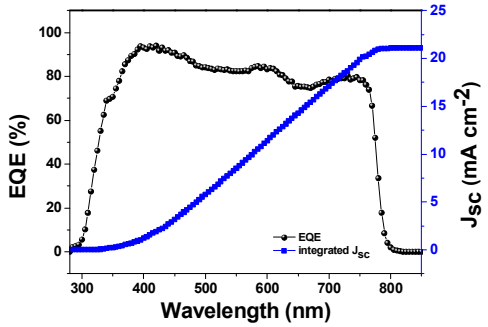

Figure 2.14 EQE spectra of the best performing PSC

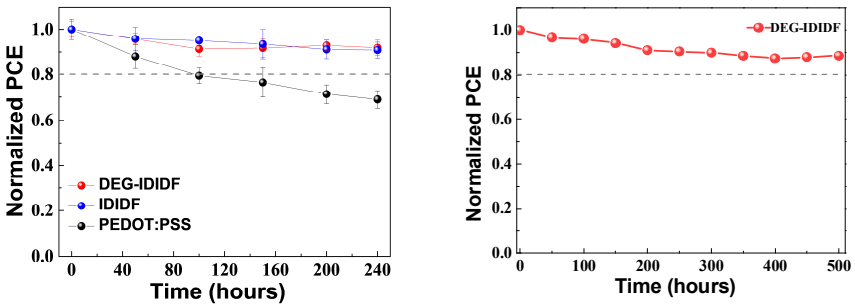

Figure 2.15 Air and thermal stability of HTMs based PSCs

HTM	Annealing (°C)	V_{oc} (V)	J_{sc} (mA/cm^2)	FF (%)	PCE (%)
PEDOT:PSS	150	0.95	16.16	0.79	12.14
IDIDF	120	1.08	18.83	0.62	12.72
DEG-IDIDF	120	1.04	21.23	0.75	16.60

Table 2-2. The best-performing photovoltaic performance of the PSCs including each PEDOT:PSS, IDIDF, and DEG-IDDF HTM.

HTM	Annealing (°C)	V_{oc} (V)	J_{sc} (mA/cm^2)	FF (%)	PCE (%)
DEG-IDIDF	RT	1.01	15.69	0.71	11.26
	80	1.04	16.84	0.74	12.96
	100	1.04	19.06	0.75	14.84
	120	1.04	21.23	0.75	16.60

Table 2-3. Photovoltaic performance of the DEG-IDIDF PSC devices under various thermal annealing

2.3.2 conventional (*n-i-p*) perovskite solar cells

2.3.2.1 Photovoltaic device performance of TEG-IDIDF

To clarify the eligibility of the TEG-IDIDF as suitable HTMs, the PSCs devices with the structures of glass/ITO/ZnO/PCBM/$MAPbI_3$/HTM/Au were fabricated, where doped and dopant-free Spiro-OMeTAD were taken as references. The devices, including the IDIDF, were also prepared for comparison. The J–V curves of the PSCs were shown in **Figure 2.16** and their performances were summarized in **Table 2.4**. As expected, the dopant-free Spiro-OMeTAD based PSC exhibited a low PCE of 7.02 % when the doped Spiro-OMeTAD based PSC showed a PCE of 17.26 % owing to relatively low hole mobility. Similarly, the non-doped IDIDF based PSC yield the PCE of 13.93 %. On other hands, the non-doped TEG-IDIDF based PSC exhibited the highest PCE of 18.09 % (V_{oc} = 1.09 V, J_{sc} = 23.61 mA cm^{-2}, and FF = 70%). Owing to superior solubility and high crystallinity feature in film state, TEG-IDIDF based PSCs provided better Voc, Jsc, and FF, compared with those of other HTM-based PSCs. The hysteresis and statistic features of the total 13 devices (TEG-IDIDF based PSCs) are provided in **Figure 2.17 and 2.18**. The reverse and forward scans showed the PCEs of 18.09 and 17.9 %, respectively. The average PCEs were about 18.09 ± 0.94 %, which were estimated from the

10 devices. It reflects a relatively small standard deviation in device reproducibility, and more than 80 % of devices demonstrated higher PCEs of > 17.5 % in our work. Finally, in order to achieve boost the PCE of the TEG-IDIDF based PSC devices, $FAPbI_3$ perovskite based device with the dopant-free and doped TEG-IDIDF as shown in **Figure 2.19** and summarized in **Table 2.5**. The dopant-free TEG-IDIDF based mixed halide perovskite exhibited the PCE of 20.42% (V_{oc} = 1.11 V, J_{sc} = 24.85 mA cm^{-2}, and FF = 74%) when doped TEG-IDIDF showed remarkable photovoltaic performance, with a maximum PCE of 22.71% along with an enhanced J_{sc} of 26.43 mA cm^{-2}, a V_{oc} of 1.14V, and a FF of 75%.

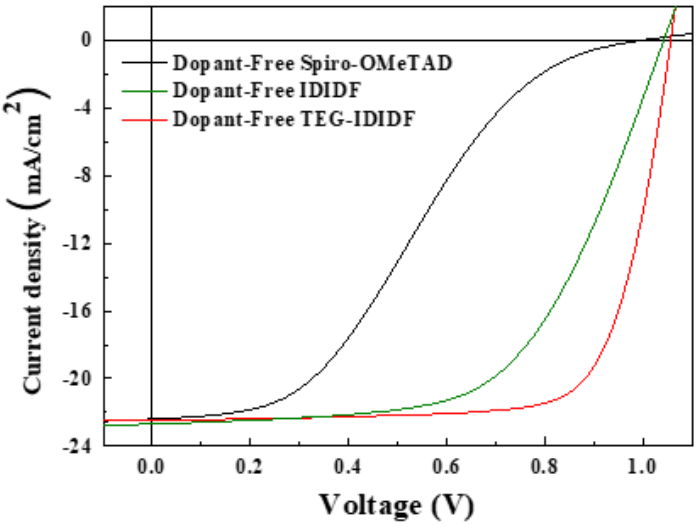

Figure 2.16 J-V characteristics of the $MAPbI_3$ based devices with undoped Spiro-OMeTAD, IDIDF, and TEG-IDIDF

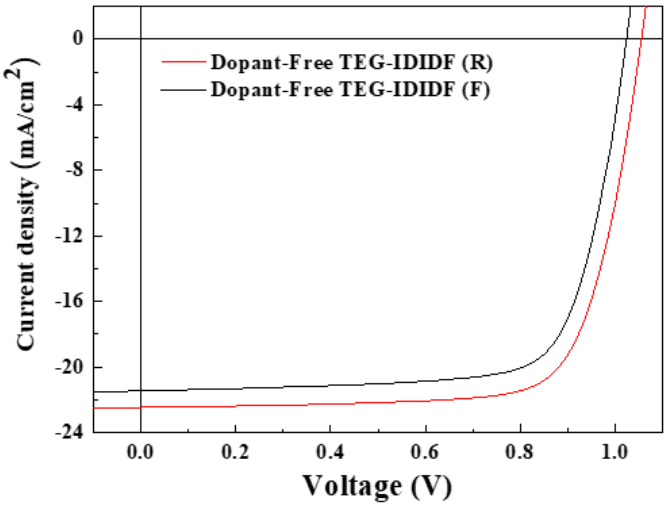

Figure 2.17 Reverse and forward scans of the champion devices based on TEG-IDIDF

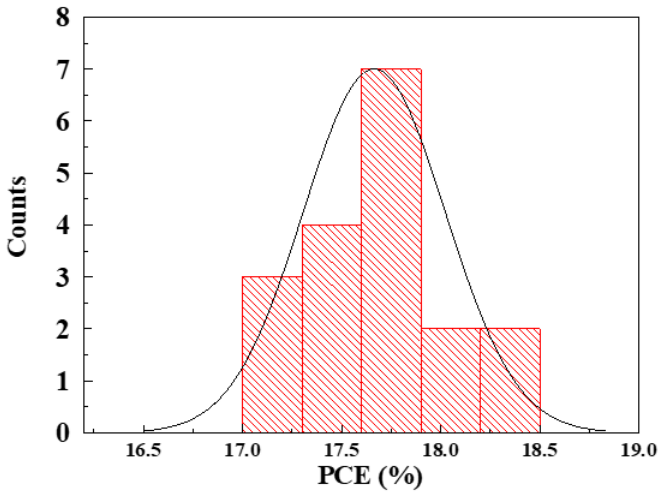

Figure 2.18 PCE histograms of over 17 devices of TEG-IDIDF

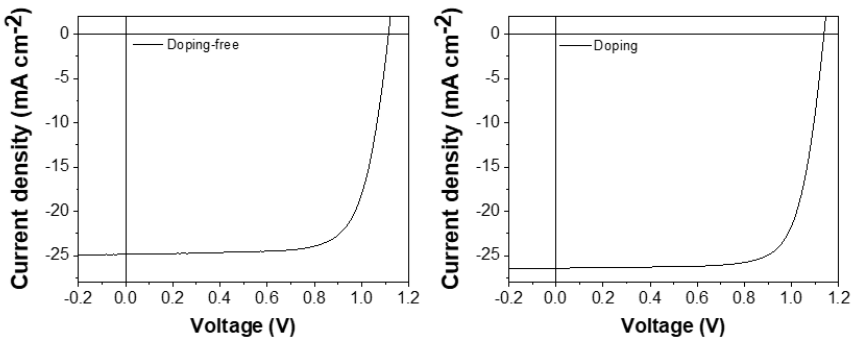

Figure 2.19 J-V characteristics of the $FAPbI_3$ based PSCs with doped and undoped TEG-IDIDF

HTM	V_{oc} (V)	J_{sc} (mA cm^{-2})	FF (%)	PCE (%)
Spiro-OMeTAD (w/o doping)	1.00	22.40	0.31	7.03
Spiro-OMeTAD (w/o doping)	1.08	21.52	0.74	17.26
IDIDF	1.04	22.69	0.59	13.93
TEG-IDIDF	1.09	23.61	0.70	18.09

Table 2.4 Photovoltaic performance of the $MAPbI_3$ based PSCs devices including different HTMs

HTM	Doping	V_{oc} (V)	J_{sc} (mA cm^{-2})	FF (%)	PCE (%)
TEG-IDIDF	X	1.11	24.846	0.740	20.43
	O	1.14	26.425	0.753	22.71

Table 2.5 Photovoltaic performance of the $FAPbI_3$ based PSCs devices including doped and undoped TEG-IDIDF

2.3.2.2 Optical, electrochemical, and thermal characteristics

The normalized UV-vis absorption (**Figure 2.20**) spectra of TEG-IDIDF in chloroform (CF) solutions and thin films were measured. A large bathochromic shift (89 nm) with additional vibronic peaks was clearly detected when the absorption peaks at 388 nm for the the solution and 477 nm for the film state, respectively. This result clearly showed that tight packing and planarization arising from the highly ordered structure in the film state even though relatively flexible and long tri-ethylene glycol chains were substituted compared to hexyl side chains. Further electrochemical properties of TEG-IDID and Spiro-OMeTAD in film state are monitored by photoelectron spectroscopy analyses (PESA) and the cyclic voltammogram (CV) (**Figure 2.21 and 2.22**). Energy level diagrams of the PSC device, including different HTMs, were shown in **Figure 2.23**, and the data were summarized in **Table 2.6**. The highest occupied molecular orbital (HOMO) level is estimated to be 5.04 eV for the TEG-IDIDF, while the lowest occupied molecular orbital (LUMO) level is -2.82 eV derived from the optical bandgap energies, respectively. The HOMO value determined by the CV is in good agreement with that of PESA observations. These deep HOMO energy levels of TEG-IDIDF were favorable for hole injection from the perovskite than that of Spiro-OMeTAD (4.93 eV). The thermogravimetric (TGA) and differential scanning calorimetry (DSC)

analyses are also conducted to clarify the thermal stability and thermal transitions of the IDID derivatives (**Figure 2.24**). The decomposition temperatures (T_d, 5% mass loss) of IDIDF, and TEG-IDIDF were 438 ^{o}C, and 430 ^{o}C and melting temperature (T_m) values were 162 ^{o}C, and 97 ^{o}C, respectively. Therefore, TEG-IDIDF possessed possibly assuring no significant variation in thermal stability.

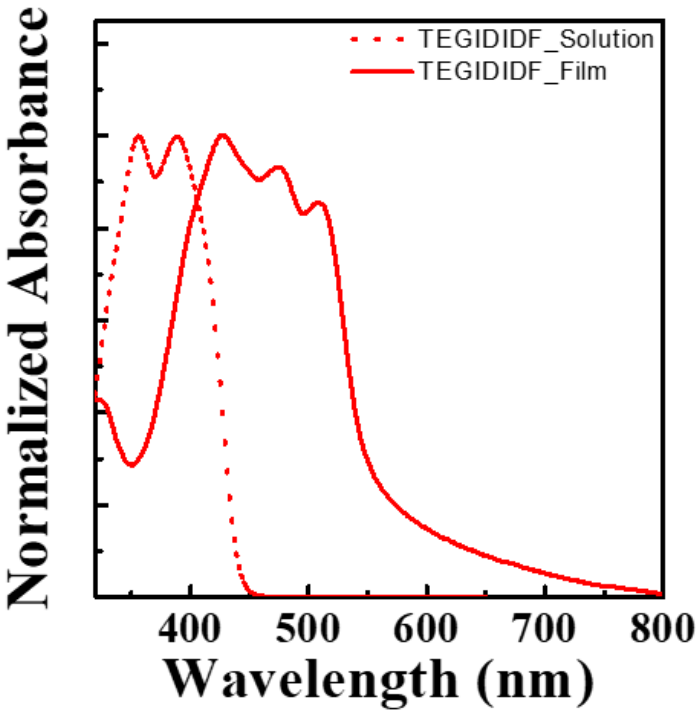

Figure 2.20 UV-vis absorption spectra of the TEG-IDIDF in solution and film states

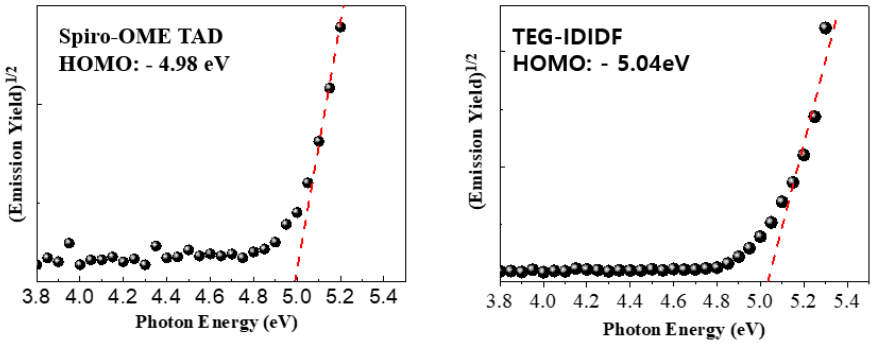

Figure 2.21 Photoelectron spectroscopy analyses of Spiro-OMeTAD and TEG-IDIDF

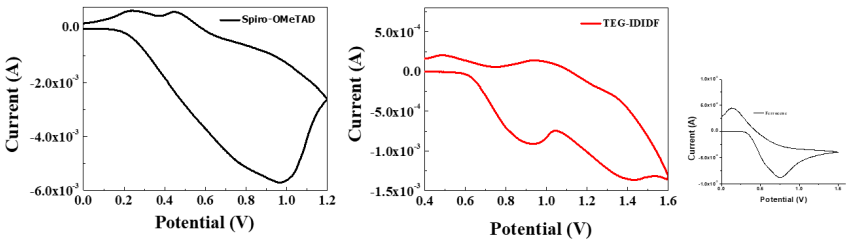

Figure 2.22 Cyclic voltammograms of Spiro-OMeTAD and TEG-IDIDF with ferrocene

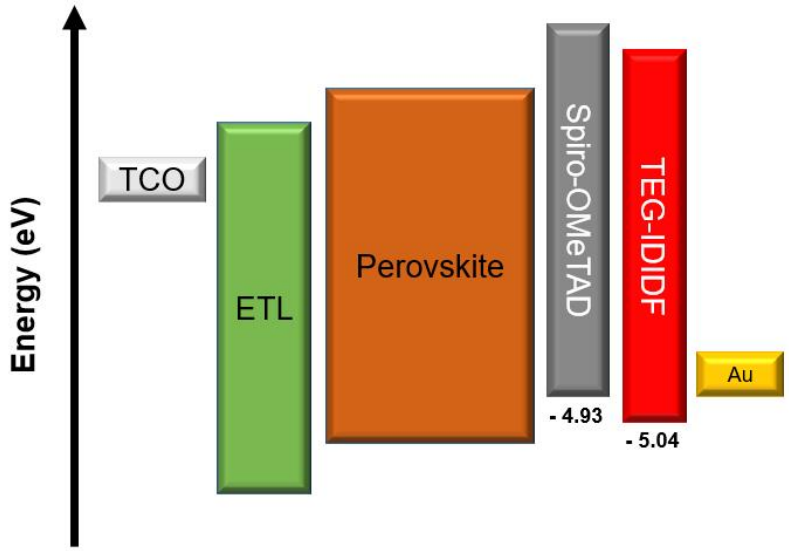

Figure 2.23 Energy level diagrams of the PSCs device including Spiro-OMeTAD and TEG-IDIDF

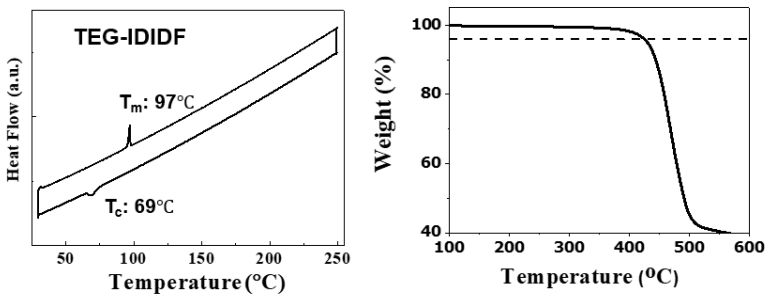

Figure 2.24 DSC and TGA analyses of TEG-IDIDF

HTM	Abs.(Sol) (nm)	Abs.(Film) (nm)	HOMO(Film) (eV)	LUMO(Film) (eV)	E_g
TEG-IDIDF	388	477	-5.04	-2.82	2.22

Table 2.6 Optical and electrochemical characteristics of TEG-IDIDF, together with the hole mobility acquired by the and SCLC.

2.3.2.3 Structual Analyses of HTMs

To identify the molecular conformation and packing motif of the TEG-IDIDF in solid and film state, single-crystal X-ray crystallography (SC-XRD) and grazing incidence wide angle X-ray diffraction (GIWAXS) analysis are carried out. SC-XRD analysis of TEG-IDIDF exhibited a planar conformation with a torsion angle of 10.36 ° between the core and thiophene (**Figure 2.25**). More importantly, even though TEG-IDIDF had longer OEG chains at *N*-positions of IDID backbone compared to DEG-IDIDF, the molecules stacks of the TEG-IDIDF gives a tight π–π distance of 3.41 Å owing to the appearance of strong intermolecular interaction, which is C O --- H interaction (2.52 Å) between the TEG chains and IDID backbone. To further confirm the molecular orientation and stacking of IDID derivatives in the thin film state, the GIWAXS analysis is used. The Spiro-OMeTAD exhibited no preferential molecular orientation due to its amorphous nature, while the distinct Bragg spots were clearly detected. Furthermore, the GIWAXS pattern of the TEG-IDIDF thin film has two strong Bragg reflections in the out-of-plane direction at q_z: 0.48 (d=12.87 $Å^{-1}$) and 0.97 (d = 6.43 $Å^{-1}$). These two Bragg spots agrees well with the SC-XRD reflections at 2θ = 6.94º (002 peak, d = 12.72 $Å^{-1}$) and 13.92 º (004 peak, d = 6.36 $Å^{-1}$). The detailed d-spacing distances for the (002) and (004) peaks estimated by SC-XRD, GIWAXS, and out-of-plane XRD analysis are

summarized in **Figure 2.26** and **Table 2.7**. These results clearly provided that the TEG-IDIDF showed similar molecular packing in solid and film states; thus, the strong intermolecular interaction with a C O --- H interaction should be existed in the film state, and it can promote the action of efficient charge transport for better photovoltaic performance.

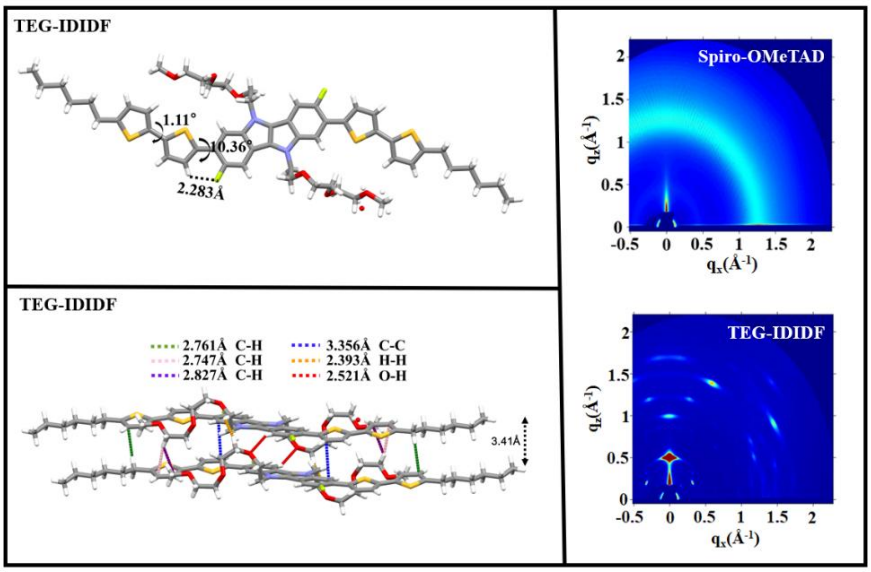

Figure 2.25 SC-XRD analysis of TEG-IDIDF and GIWAXS analyses of Spiro-OMeTAD and TEG-IDIDF

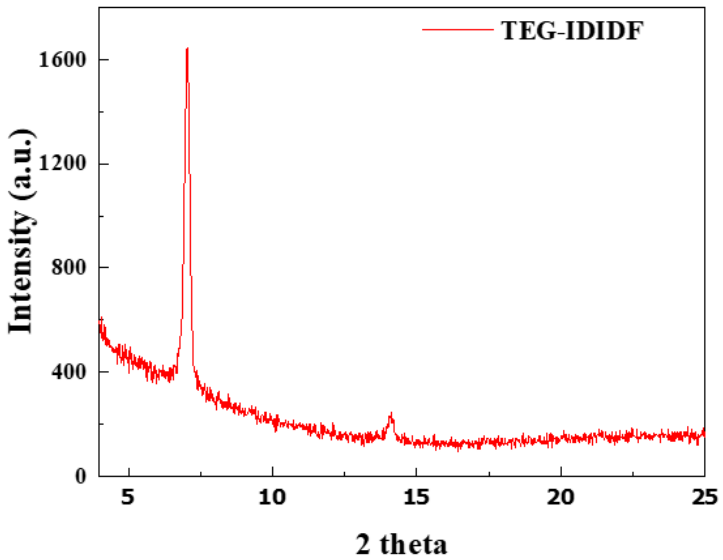

Figure 2.26 Out-of-plane XRD of the TEG-IDIDF

hkl	SC-XRD	GIWAXS	Out-of-plane XRD
002	12.72	12.87	12.54
004	6.36	6.44	6.27

Table 2.7 SC-XRD, GIWAXS, and out-of-plane XRD patterns of the TEG-IDIDF and clearly identifiying the (002) and (004) peaks of TEG-IDIDF

2.3.2.4 Charge transporting properties of HTM

The hole transporting characteristic of TEG-IDIDF was acquired from the space-charge-limited current (SCLC) analysis. Hole-only devices were fabricated, where doped Spiro-OMeTAD was also tested for comparison. The outstanding hole mobility of 6.25×10^{-4} $cm^2 V^{-1} s^{-1}$ was obtained with undoped TEG-IDIDF when doped Spiro-OMeTAD exhibited 3.67×10^{-4} $cm^2 V^{-1} s^{-1}$. To check the hole extraction ability of the HTMs at the perovskite/HTM interface, we measured steady-state photoluminescence (PL) and time-resolved PL characteristics of $MAPbI_3$/HTMs (**Figure 2.27**). Strong PL quenching was observed when TEG-IDIDF and doped Spiro-OMeTAD were coated on perovskite film. Similarly, from time-resolved PL measurements, perovskite only device showed PL decay lifetime of 128 ns. When TEG-IDIDF, and doped Spiro-OMeTAD were used as HTM, TEG-IDIDF showed the the PL decay lifetimes reducing (τ_{ave} : 4.3 ns) when Spiro-OMeTAD showed (τ_{ave} 5.6 ns).[24,25] These results clearly demonstrates the outstanding hole extraction ability of TEG-IDIDF due to its high mobility from the ordered structure with closed π–π stacking in the thin film state.

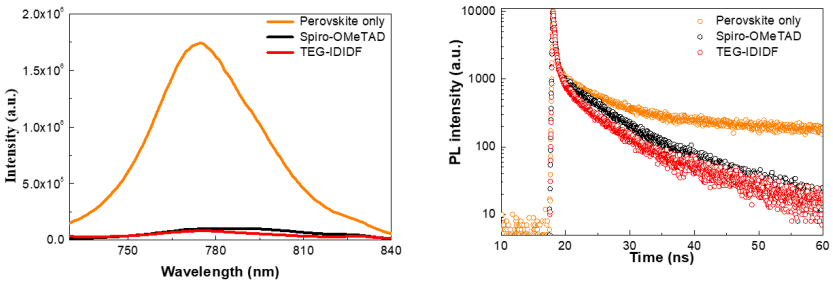

Figure 2.27 Stead-state PL quenching and TCSPC PL measurements of bare Perovskite film and each HTM (doped Spiro-OMeTAD and undoped TEG-IDIDF) coated on the perkvsite layer

2.3.2.5 Device stability

To ensure that the perovskite layer and TEG-IDIDF retained their crystallinity at high humidity conditions, we measured the device performance and investigated by GIWAX (**Figure 2.28 and 2.29**). The device (ITO/ZnO/PCBM/$MAPbI_3$/TEG-IDIDF) and stored under environmental conditions of 65% relative humidity for 50 days. The pristine device showed clear TEG-IDIDF bragg spots and the perovskite layer. Interestingly, the devices which were stored under 65 % RH for 25 days exhibited clear peaks as well as Pristine. However, the devices stored under 65 % RH for 50 days showed indistinctive bragg spots of TEG-IDIDF when PbI_2 peak also appeared, which means perovskite crystallinity is broken by the high moisture. Meanwhile, doped Spiro-OMeTAD based devices were also prepared at the same condition as shown in **Figure 2.29**. Only the perovskite layer peaks were shown due to the amorphous of Spiro-OMeTAD. The device stored at 65% humidity showed that the PbI_2 peak appeared only in 3 days, and perovskite layer peaks were also damaged by moisture. Respectively, TEG-IDIDF could effectively protect the perovskite layer due to its high crystallinity in the film state. These result clearly show why the PCE retained at high humidity for 50 days.

Moreover, the thermal stability of PSCs device is also another crucial factor in the PSC community. However, only a few of HTMs have been studied

by now. The devices with TEG-IDIDF and doped Spiro-OMeTAD were tested under thermal stress at 60 °C. It is well known that the glass transition temperature of doped Spiro-OMeTAD (50 °C) is relatively low, and its crystallization of doped Spiro-OMeTAD at high temperature is negatively affected device performance. As seen in **Figure 2.30**, the doped Spiro-OMeTAD based PSC device showed apparent degradation when thermal annealing was applied from 60 °C for 24 hours. In contrast, TEG-IDIDF based PSC device clearly showed that the device maintained its initial value when the thermal stress at 60 °C for 120 hours. These experimental findings suggest that the TEG-IDIDF can become a suitable alternative protecting layer over the Spiro-OMeTAD.

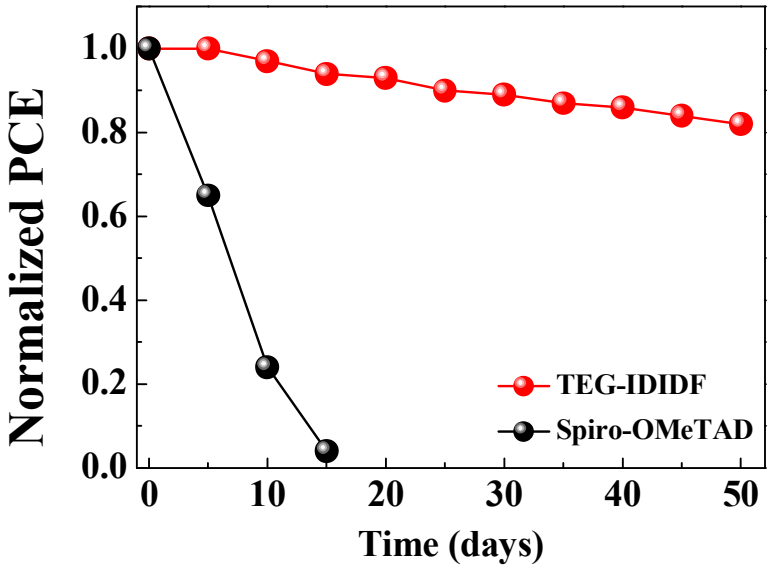

Figure 2.28 Efficiency features of the PSC devices containing the TEG-IDIDF and doped-Spiro-OMeTAD HTMs under 60 % RH.

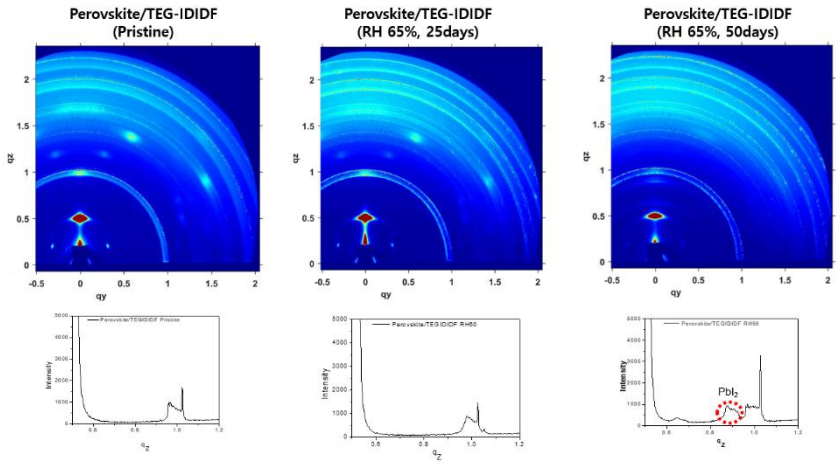

Figure 2.29 GIWAXS analyses of the device with Pervskite/undoped TEG-IDIDF under constant humidity (RH 65) taken for 50 days and their corresponding out-of-plane linecuts of GIWAXS patterns.

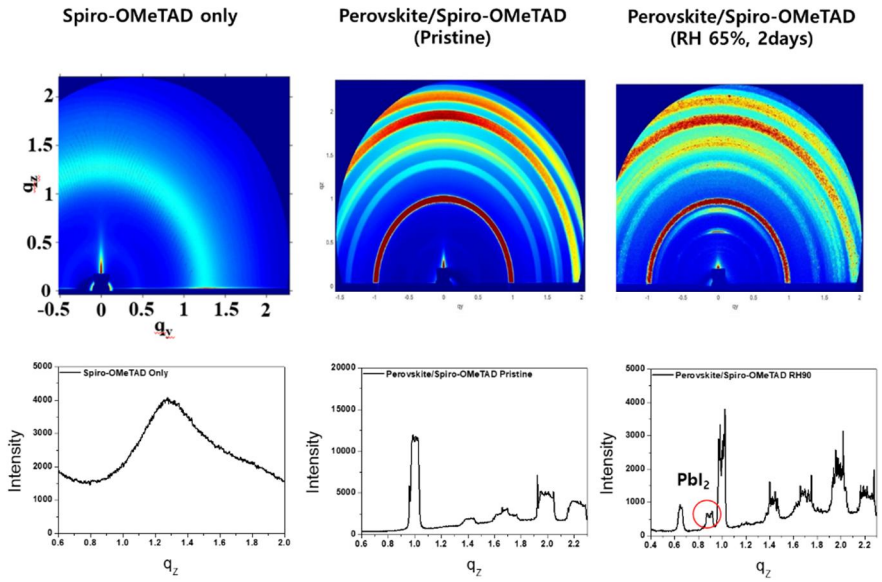

Figure 2.30 GIWAXS analyses of the device with Pervskite/doped Spiro-OMeTAD under constant humidity (RH65) taken for 3 days and their corresponding out-of-plane linecuts of GIWAXS patterns.

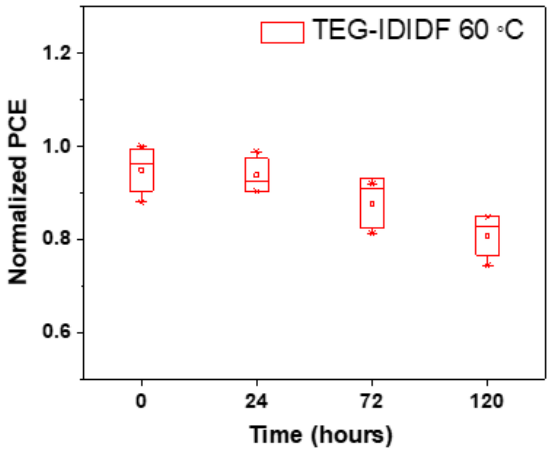

Figure 2.31 Thermal stability of the PSCs device with undoped TEG-IDIDF

2.4 Conclusion

As an efficient HTM, a novel small molecule dopant-free crystallized DEG-IDIDF and TEG-IDIDF were investigated by applying a DEG and TEG chain at the *N*-position of the IDID backbone for improved solubility and mobility. Corresponding tight π–π interactions between planar structures lead to tight molecular packing, ensuring improved crystallinity properties of DEG-IDIDF and TEG-IDIDF. The DEG-IDIDF inverted PSCs showed an improved PCE of approximately 16.60% when compared to the IDIDF and PEDOT:PSS based PSCs. Moreover, the TEG-IDIDF conventional PSCs exhibited an outstanding PCE of 18.09 %, when $FAPbI_3$ based PSCs device with TEG-IDIDF exhibited superior PCEs of doped (22.71%) and non-doped (20.42%) without a rapid degradation originally present in PSC during exposure to humidity. Both DEG-IDIDF and TEG-IDIDF containing PSCs showed outstanding thermal stability, and it could ensure the role of an efficient passivation layer during thermal stress. Therefore, these experimental observations suggest that HTMs without dopants could make substantial progress toward realizing of high-performance inverted and convetional PSCs after establishing more optimization processes.

2.5 Reference

[1] Yoo, J. J.; Seo, G.; Chua, M. R.; Park, T. G.; Lu, Y.; Rotermund, F.; Kim, Y.-K.; Moon, C. S.; Jeon, N. J.; Correa-Baena, J.-P.; et al. Efficient perovskite solar cells via improved carrier management. Nature 2021, 590 (7847), 587-593.

[2] De Bastiani, M.; Mirabelli, A. J.; Hou, Y.; Gota, F.; Aydin, E.; Allen, T. G.; Troughton, J.; Subbiah, A. S.; Isikgor, F. H.; Liu, J.; et al. Efficient bifacial monolithic perovskite/silicon tandem solar cells via bandgap engineering. Nature Energy 2021, 6 (2), 167-175.

[3] Kim, J. Y.; Lee, J.-W.; Jung, H. S.; Shin, H.; Park, N.-G. High-Efficiency Perovskite Solar Cells. Chem. Rev. 2020, 120 (15), 7867-7918.

[4] You, G.; Zhuang, Q.; Wang, L.; Lin, X.; Zou, D.; Lin, Z.; Zhen, H.; Zhuang, W.; Ling, Q. Dopant-Free, Donor–Acceptor-Type Polymeric Hole-Transporting Materials for the Perovskite Solar Cells with Power Conversion Efficiencies over 20%. Adv. Energy Mater. 2020, 10 (5), 1903146.

[5] Jeong, M.; Choi, I. W.; Go, E. M.; Cho, Y.; Kim, M.; Lee, B.; Jeong, S.; Jo, Y.; Choi, H. W.; Lee, J.; et al. Stable perovskite solar cells with efficiency exceeding 24.8% and 0.3-V voltage loss. Science 2020, 369 (6511), 1615-1620.

[6] Pham, H. D.; Xianqiang, L.; Li, W.; Manzhos, S.; Kyaw, A. K. K.; Sonar, P. Organic interfacial materials for perovskite-based optoelectronic devices. Energy & Environmental Science 2019, 12 (4), 1177-1209, 10.1039/C8EE02744G.

[7] Xia, Y.; Ran, C.; Chen, Y.; Li, Q.; Jiang, N.; Li, C.; Pan, Y.; Li, T.; Wang, J.; Huang, W. Management of perovskite intermediates for highly efficient inverted planar heterojunction perovskite solar cells. J.Mater. Chem. A. 2017, 5 (7), 3193-3202, 10.1039/C6TA09554B.

[8] Li, E.; Liu, C.; Lin, H.; Xu, X.; Liu, S.; Zhang, S.; Yu, M.; Cao, X.-M.; Wu,

Y.; Zhu, W.-H. Bonding Strength Regulates Anchoring-Based Self-Assembly Monolayers for Efficient and Stable Perovskite Solar Cells. Adv. Funct. Mater. 2021, 31 (35), 2103847.

[9] Sun, X.; Deng, X.; Li, Z.; Xiong, B.; Zhong, C.; Zhu, Z.; Li, Z. a.; Jen, A. K.-Y. Dopant-Free Crossconjugated Hole-Transporting Polymers for Highly Efficient Perovskite Solar Cells. Advanced Science 2020, 7 (13), 1903331.

[10] Bu, T.; Liu, X.; Zhou, Y.; Yi, J.; Huang, X.; Luo, L.; Xiao, J.; Ku, Z.; Peng, Y.; Huang, F.; et al. A novel quadruple-cation absorber for universal hysteresis elimination for high efficiency and stable perovskite solar cells. Energy & Environmental Science 2017, 10 (12), 2509-2515, 10.1039/C7EE02634J.

[11] You, J.; Meng, L.; Song, T.-B.; Guo, T.-F.; Yang, Y.; Chang, W.-H.; Hong, Z.; Chen, H.; Zhou, H.; Chen, Q.; et al. Improved air stability of perovskite solar cells via solution-processed metal oxide transport layers. Nature Nanotechnology 2016, 11 (1), 75-81.

[12] Jiang, Q.; Zhang, L.; Wang, H.; Yang, X.; Meng, J.; Liu, H.; Yin, Z.; Wu, J.; Zhang, X.; You, J. Enhanced electron extraction using SnO2 for high-efficiency planar-structure HC(NH2)2PbI3-based perovskite solar cells. Nature Energy 2016, 2 (1), 16177.

[13] Jeng, J.-Y.; Chiang, Y.-F.; Lee, M.-H.; Peng, S.-R.; Guo, T.-F.; Chen, P.; Wen, T.-C. CH3NH3PbI3 Perovskite/Fullerene Planar-Heterojunction Hybrid Solar Cells. Adv. Mater. 2013, 25 (27), 3727-3732.

[14] Yao, Y.; Cheng, C.; Zhang, C.; Hu, H.; Wang, K.; De Wolf, S. Organic Hole-Transport Layers for Efficient, Stable, and Scalable Inverted Perovskite Solar Cells. Adv. Mater. n/a (n/a), 2203794.

[15] Li, M.-H.; Sun, T.-G.; Shao, J.-Y.; Wang, Y.-D.; Hu, J.-S.; Zhong, Y.-W. A sulfur-rich small molecule as a bifunctional interfacial layer for stable perovskite solar cells with efficiencies exceeding 22%. Nano Energy 2021, 79, 105462.

[16] Wang, Y.; Yue, Y.; Yang, X.; Han, L. Toward Long-Term Stable and Highly Efficient Perovskite Solar Cells via Effective Charge Transporting Materials. Adv. Energy Mater. 2018, 8 (22), 1800249.

[17] Zhang, F.; Wang, Z.; Zhu, H.; Pellet, N.; Luo, J.; Yi, C.; Liu, X.; Liu, H.; Wang, S.; Li, X.; et al. Over 20% PCE perovskite solar cells with superior stability achieved by novel and low-cost hole-transporting materials. Nano Energy 2017, 41, 469-475.

[18] 27 Yang, W. S.; Noh, J. H.; Jeon, N. J.; Kim, Y. C.; Ryu, S.; Seo, J.; Seok, S. I. High-performance photovoltaic perovskite layers fabricated through intramolecular exchange. Science 2015, 348 (6240), 1234-1237.

[19] H. D. Pham, T. T. Do, J. Kim, C. Charbonneau, S. Manzhos, K. Feron, W. C. Tsoi, J. R. Durrant, S. M. Jain, P. Sonar, 2018, 8, 1703007.

[20] J. Qiu, H. Liu, X. Li, S. Wang, F. Zhang, Solar RRL 2019, 3.

[21] Z. Cui, Y. Wang, Y. Chen, X. Chen, X. Deng, W. Chen, C. Shi, Organic

[22] J. Chen, J. Xia, H.-J. Yu, J.-X. Zhong, X.-K. Wu, Y.-S. Qin, C. Jia, Z. She, D.-B. Kuang, G. Shao, Chemistry of Materials 2019, 31, 5431.

[23] J. Xiang, X. Liu, M. Sun, X. Li, S. Wang, Y. Xiao, J. Zhang, F. Zhang, ChemistrySelect 2018, 3, 13032. https://doi.org/10.1002/slct.201803002

[24] D. Bharath, M. Sasikumar, N. R. Chereddy, J. R. Vaidya, S. Pola, Solar Energy 2018, 174, 130.

[25] C. Shen, Y. Wu, H. Zhang, E. Li, W. Zhang, X. Xu, W. Wu, H. Tian, W. H. Zhu, Angew Chem Int Ed Engl 2019, 58, 3784.

[26]

[27] Jiang, K.; Wang, J.; Wu, F.; Xue, Q.; Yao, Q.; Zhang, J.; Chen, Y.; Zhang, G.; Zhu, Z.; Yan, H.; et al. Dopant-Free Organic Hole-Transporting Material for Efficient and Stable Inverted All-Inorganic and Hybrid Perovskite Solar Cells. Adv. Mater. 2020, 32 (16), 1908011.

[28] Said, A. A.; Xie, J.; Zhang, Q. Recent Progress in Organic Electron Transport Materials in Inverted Perovskite Solar Cells. Small 2019, 15 (27), 1900854.

[29] Yang, X.; Xi, J.; Sun, Y.; Zhang, Y.; Zhou, G.; Wong, W.-Y. A dopant-free twisted organic small-molecule hole transport material for inverted planar perovskite solar cells with enhanced efficiency and operational stability. Nano Energy 2019, 64, 103946.

[30] Chen, W.; Wu, Y.; Fan, J.; Djurišić, A. B.; Liu, F.; Tam, H. W.; Ng, A.; Surya, C.; Chan, W. K.; Wang, D.; et al. Understanding the Doping Effect on NiO: Toward High-Performance Inverted Perovskite Solar Cells. Adv. Energy Mater. 2018, 8 (19), 1703519.

[31] Yang, J.; Siempelkamp, B. D.; Liu, D.; Kelly, T. L. Investigation of CH3NH3PbI3 Degradation Rates and Mechanisms in Controlled Humidity Environments Using in Situ Techniques. ACS Nano 2015, 9 (2), 1955-1963.

[32] Sun, K.; Zhang, S.; Li, P.; Xia, Y.; Zhang, X.; Du, D.; Isikgor, F. H.; Ouyang, J. Review on application of PEDOTs and PEDOT:PSS in energy conversion and storage devices. Journal of Materials Science: Materials in Electronics 2015, 26 (7), 4438-4462.

[33] Wang, Y.; Chen, W.; Wang, L.; Tu, B.; Chen, T.; Liu, B.; Yang, K.; Koh, C. W.; Zhang, X.; Sun, H.; et al. Dopant-Free Small-Molecule Hole-Transporting Material for Inverted Perovskite Solar Cells with Efficiency Exceeding 21%. Adv. Mater. 2019, 31 (35), 1902781.

[34] Pham, H. D.; Hayasake, K.; Kim, J.; Do, T. T.; Matsui, H.; Manzhos, S.; Feron, K.; Tokito, S.; Watson, T.; Tsoi, W. C.; et al. One step facile synthesis of a novel anthanthrone dye-based, dopant-free hole transporting material for efficient and stable perovskite solar cells. J.Mater. Chem. C. 2018, 6 (14), 3699-3708, 10.1039/C7TC05238C.

[35] Rakstys, K.; Saliba, M.; Gao, P.; Gratia, P.; Kamarauskas, E.; Paek, S.; Jankauskas, V.; Nazeeruddin, M. K. Highly Efficient Perovskite Solar Cells Employing an Easily Attainable Bifluorenylidene-Based Hole-Transporting Material. Angew. Chem. Int. Ed. 2016, 55 (26), 7464-7468.

[36] 38 Belisle, R. A.; Jain, P.; Prasanna, R.; Leijtens, T.; McGehee, M. D. Minimal Effect of the Hole-Transport Material Ionization Potential on the

Open-Circuit Voltage of Perovskite Solar Cells. ACS Energy Letters 2016, 1 (3), 556-560.

[37] M. Cheng, K. Aitola, C. Chen, F. Zhang, P. Liu, K. Sveinbjörnsson, Y. Hua, L. Kloo, G. Boschloo, L. Sun, Nano Energy 2016, 30, 387.

[38] X. M. Zhao, F. Zhang, C. Y. Yi, D. Q. Bi, X. D. Bi, P. Wei, J. S. Luo, X. C. Liu, S. R. Wang, X. G. Li, S. M. Zakeeruddin, M. Gratzel, Journal of Materials Chemistry A 2016, 4, 16330.

[39] X. Sun, Q. Xue, Z. Zhu, Q. Xiao, K. Jiang, H.-L. Yip, H. Yan, Z. a. Li, Chemical Science 2018, 9, 2698.

[40] I. Cho, N. J. Jeon, O. K. Kwon, D. W. Kim, E. H. Jung, J. H. Noh, J. Seo, S. I. Seok, S. Y. Park, Chem. Sci., 2017, 8 (1), 734

Chapter 3.

Aqueous-alcohol-processable indolo[3,2-b]indole based crystalline small molecules for organic field effect transistors with penta-ethylene glycol side chains

3.1 Introduction

Recent advances in π-conjugated functional organic semiconductors (OSCs) have garnered considerable interest as promising options in a variety of their potential organic electronic devices, such as organic field effect transistors (OFETs).[1-5] Extensive studies on the molecular design of OSCs have improved charge transporting characteristics, and the mobility of solution processed OFETs has been boosted to over 43 $cm^2 V^{-1}s^{-1}$.[6-9] Despite high-performing mobility, the state-of-the-art molecules are soluble only in halogenated or aromatic solvents, which are very toxic to humans and the environment. These solvents are being restricted under rigorous chemical regulations such as Registration Evaluation, Authorization and Restriction of Chemicals (REACH), thereby retarding the industrialization of solution processed OFET technology.[10-12] In this regard, substantial efforts have been dedicated to replacing these toxic solvents with green solvents such as alcohol and water.

In recent years, several groups have reported that replacing linear alkyl

chains with branched alkyl chains or appending ionic groups to the alkyl chains is an efficient approach to improving the solubility of OSCs in green solvents.[13-15] For instance, Geng *et al*. addressed the DPP-based polymers containing the branched alkyl side chains, demonstrating the hole mobility of 1 cm^2 V^{-1} s^{-1} in anisole solvent processed OFETs.[16] However, although the branched alkyl chains could provide sufficient solubility for halogen-free solvent, the device efficiency could reduce owing to intrinsic branched alkyl chains disturbing the molecular stacking, and the dissolution difficulty in alcohol solvents. Yang *et al*. also developed the water soluble conjugated polymer, poly(p-phenylene-vinylene), PPV with ionic groups, resulting in hole mobility of 5.0×10^{-4} cm^2 V^{-1} s^{-1}. [17] Moreover, polymers with ionic groups also revealed relatively low mobility because the ionic groups could serve as potential charge traps, which restricted efficient charge transporting characteristics in practical device applications.[18]

To overcome the abovementioned drawbacks, oligo(ethylene glycol) (OEG) side chains have been used due to their distinct characteristics, such as hydrophilicity, high polarity, and flexibility. As a result, the OSCs with short OEG chains could provide better solubility for polar organic solvents than the OSCs with long carbon alkyl chains. Moreover, the high flexibility of OEG chains would result in close π - π stacking and thereby enhanced charge carrier

mobility, but further research utilizing OEG chains is rare due to batch-to-batch variation of polymer semiconductors.[19-21] In this respect, controlling the OEG chain length and the substitution position on the OSCs is one promising strategy for obtaining eco-friendly processes and high device performance.

3.2 Experimental

Material synthesis of PEG-IDIDF:

2,7-dibromo-3,8-difluoro-5,10-di(2,5,8,11,14-pentaoxahexadecan-16-yl)-5,10-dihydroindolo[3,2-b]indole. (1)

A 100 mL two-necked RBF, equipped with a magnetic stirrer bar and reflux condenser was baked under a reduced pressure and back fillled with Ar (x3). 2,7-dibromo-3,8-difluoro-5,10-dihydroindolo [3,2-b]indole (380 mg, 0.95 mmol), anhydrous THF (20 mL), and NaH (91.20 mg, 3.79 mmol) were added to the baked reaction vessel. After 10 minutes at room temperature (RT), 2,5,8,11,14-pentaoxahexadecan-16-yl 4-methylbenzenesulfonate (1.54g, 3.79 mmol) was added to the reaction mixture. After that, the reaction mixture was gently refluxed for 24 hours. After reaction completion, the reaction mixture was poured into brine (200 mL) and extracted with DCM. The organic layer was separated, washed (water, 200 mL x 3), dried with $MgSO_4$, and concentrated, sequentially. The resulting crude product was purified by the flash column chromatography (EA/n-hexane 1 : 9, v/v) and recrystallization (EA) to afford 2 as a white crystalline solid (610 mg, 73.92%). 1H-NMR (300 MHz, CDCl3, δ): 7.65(s, 1H), 7.63(d, J ¼ 6 Hz 1H), 4.54(t, J ¼ 6 Hz 2H), 3.92 (t, J ¼ 6 Hz 2H), 3.53 (m, 16H), 3.36 (s, 3H).

3,8-difluoro-5,10-di(2,5,8,11,14-pentaoxahexadecan-16-yl)-2,7-bis(5'-hexyl-[2,2'-bithiophen]-5-yl)-5,10-dihydroindolo[3,2-b]indole (PEG-IDIDF).

2,7-dibromo-3,8-difluoro-5,10-di(2,5,8,11,14-pentaoxahexadecan-16-yl)-5,10-dihydroindolo[3,2-b]indole (1) (600 mg, 0.74 mmol), 50-hexyl-2,20-bithiophene-5-boronic acid pinacol ester (1.03g, 2.76 mmol), tetrakis(triphenylphosphine)palladium(0) (132 mg, 0.11 mmol), THF (30 mL), and 2 N NaOH aqueous solution (15 mL) were added to a 100 mL two-necked RBF, equipped with a magnetic stirrer bar and reflux condenser. The reaction mixture was gently refluxed at 80 ºC in an Ar atmosphere. After 24 hours, the reaction mixture was quenched with H_2O (300 mL), neutralized (1 N HCl), and extracted with DCM. The combined organic phase was dried with $MgSO_4$ and concentrated under reduced pressure. The crude product was purified by flash column chromatography (chloroform/n-hexane 1 : 8, v/v) and recrystallization (EA) to afford PEG-IDIDF as orange crystals (530 mg, 63.62%). 1H-NMR (500 MHz, tetrahydrofuran-d8, d): 7.86(d, J ¼ 6.5 Hz 1H) 7.77(d, J ¼ 12.5 Hz 1H) 7.48(d, J ¼ 3 Hz 1H) 7.16(d, J ¼ 3 Hz 1H) 7.07(d, J ¼ 3.5 Hz 1H) 6.74(d, J ¼ 3.5 Hz 1H) 4.74(t, J ¼ 5Hz 2H), 3.97(t, J ¼ 5.5 Hz 2H), 3.45(m, 16H), 3.23(s, 3H) 2.82 (t, J ¼ 8 Hz 2H), 1.69 (m, 2H), 1.35 (m, 6H), 0.91(t, J ¼ 4.5 Hz 3H). HRMS (FAB+, m-NBA): calcd for 1206.50; found, 1206.50.

Characterization:

Chemical structures were fully identified by ^{1}H NMR and ^{13}C NMR (Bruker, Advance-300 and Advance-500), GC-Mass (JEOL, JMS-700), and elemental analysis (CE Instrument, EA1110). UV-vis spectra were recorded on a SHIMADZU UV-1650PC. HOMO levels of organic materials were obtained from the cyclic voltammetry measurements. The differential scanning calorimeter (DSC) measurements were carried out using a PerkinElmer DSC7 with a TAC 7/DX instrument controller at the heating and cooling rate of 10 °C min^{-1}. The thermogravimetric analysis (TGA) was performed by increasing the temperature from 30 to 600 °C with a rate of 10 °C min−1 using Discovery TGA (TA instruments) in the N_2 atmosphere. Cyclic voltammetry measurements were performed using a 273A (Princeton Applied Research) with a one-compartment platinum working electrode, a silver wire, a platinum wire counter-electrode, and the IDID derivatives were spin-coated indium-tin-oxide (ITO) glass as a reference electrode. Measurements were performed in a 0.5×10^{-3} M acetonitrile solution with 0.1 M tetrabutylammonium tetrafluoroborate as supporting electrolyte at a scan rate of 50 mV s^{-1}. Each oxidation potential was calibrated using ferrocene as a reference. LUMO levels were evaluated with the HOMO level and the optical band gap, which was obtained from the edge of the film absorption spectra. GIWAXS was done at

the 9A Beam-line of Pohang Acceleration Laboratory. Film surface topologies were obtained by a NX-10 (Park systems, Korea).

Device Fabrication and Measurement:

To prepare the substrates, SiO_2/Si substrates (p-doped 300 nm) were rinsed with acetone and isopropyl alcohol, respectively, for 10 min in an ultrasonicator, followed by 30 min UV (360 nm) O_3 treatment. The polymer dielectric layer, PVN (MW = 175 kg mol^{-1}, Aldrich), dissolved in toluene (3 mg mL^{-1}) was then spin-coated onto the SiO_2 surface (3000 rpm for 1 min), followed by annealing (100 °C for 15 min) in a glove box to form a charge trapping layer (≈10 nm). Afterward, IDID derivatives were dissolved in chloroform (0.2–0.3 wt%), and spin-coated at 3000 rpm for 30 sec in the nitrogen filled glove box. Source and drain electrode were thermally deposited same condition with VD device fabrication. The urrent-voltage characteristics of all the OFETs were measured in a nitrogen filled glove box, using a Keithley 4200 SCS instrument connected to a probe station.

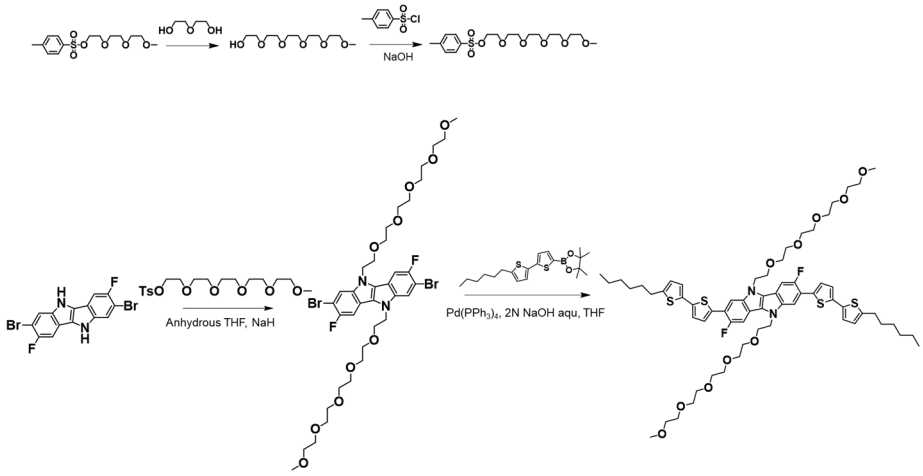

Scheme 3.1 chemical structures of TEG-IDIDF

3.3 Results and Discussion

3.3.1 Material synthesis, optical, electrochemical, and thermal characteristics

Scheme. 1 shows the molecular structures of IDID derivative, namely, PEG-IDIDF, where the penta-ethylene glycol side chains are denoted as PEG, respectively. Structural details for the IDID derivative monitored from the ^{1}H NMR, ^{13}C NMR, and mass analyses, together with the synthetic procedure in the Experimental section. It is worth noting that the PEG-IDIDF exhibited promising solubility (above 30 mg mL^{-1}) in common organic solvents at room temperature (RT) as summarized in **Table 3.1**. In addition, as expected from our molecular designing rationale, the PEG-IDIDF ensured sufficient alcohol solvent solubility (8 mg mL^{-1} at RT), when IDID derivatives with shorter OEG side chains, di-ethylene and tri-ethylene glycol side chains, were not dissolved in alcohol solvents. **Figure 3.1** plots the normalized UV-vis absorption spectra for the IDIDF and PEG-IDIDF in chloroform (CF) solutions and thin films. Although PEG side chains replaced the hexyl side chains of IDIDF, both IDIDF and PEG-IDIDF showed similar absorption spectra in the solution and film states. It indicates that the PEG side chains at N-positions of the IDID do not induce noticeable distortion of the molecule. Electrochemical properties of the IDID derivatives in the film state are estimated by the cyclic voltammogram

(CV) measurements (**Figure 3.2**). The highest occupied molecular orbital (HOMO) levels were estimated to be –5.18 eV and –5.03 eV for the IDIDF and PEG-IDIDF, respectively, while the lowest occupied molecular orbital (LUMO) levels were –2.90 eV and –2.79 eV. All data were derived from the optical bandgap (E_g^{opt}) of the IDID derivatives as calculated from the film absorption onsets. Their corresponding results are summarized in **Table 3.2**. The thermal properties of the PEG-IDIDF were evaluated by the thermogravimetric (TGA) and differential scanning calorimetry (DSC) analyses (**Figure 3.3 and 3.4**). The observed decomposition (T_d, 5% mass loss) and melting (T_m) temperatures of the PEG-IDIDF were 318 ^oC and 54 ^oC, respectively. In the cooling cycle, one exothermic peak (24 °C) is noticed, and we could predict that the broad exothermic peak is crystallization temperature.

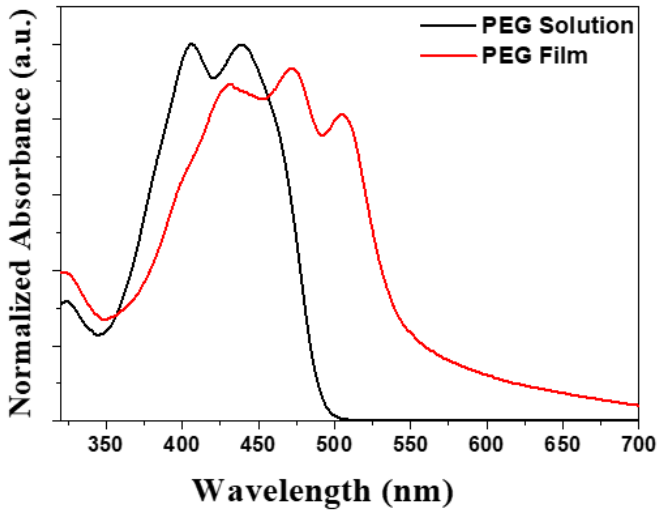

Figure 3.1 Normalized UV–visible absorption spectra of the PEG-IDIDF molecules in solution and film state.

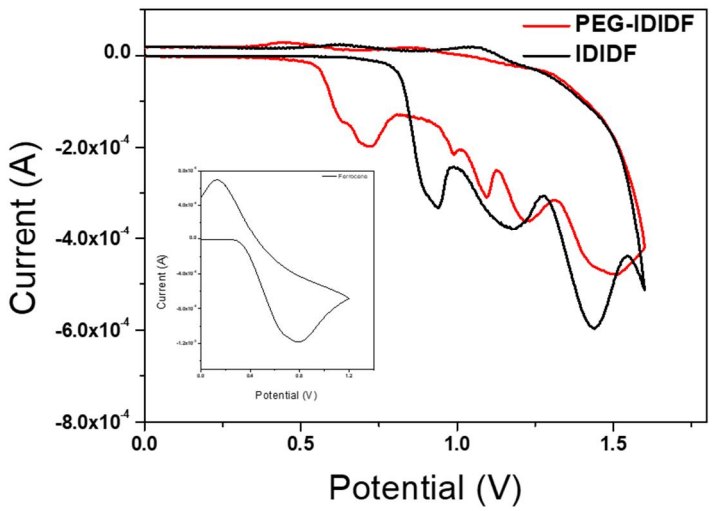

Figure 3.2 Cyclic voltammograms (CVs) of IDIDF and PEG-IDIDF (Inset: CV of ferrocene)

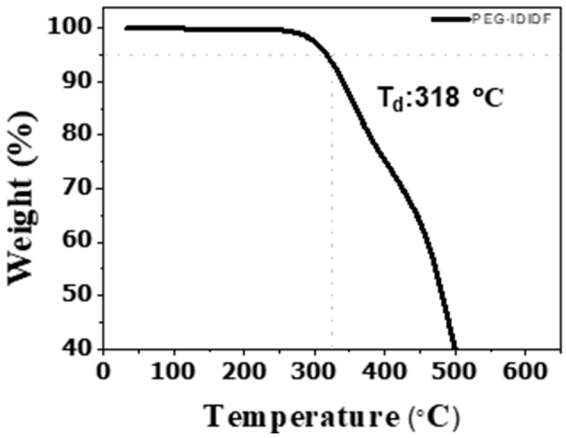

Figure 3.3 TGA curves of PEG-IDIDF

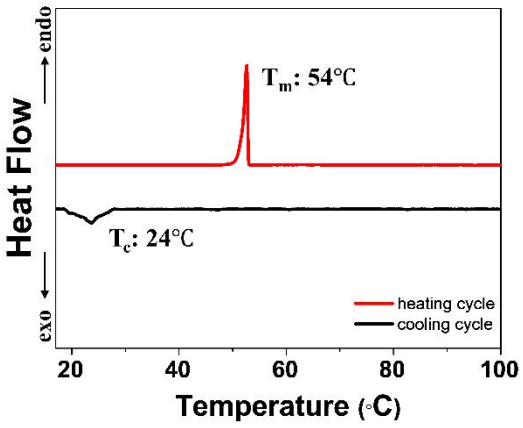

Figure 3.4 DSC analysis of PEG-IDIDF

	PEG-IDIDF
Chloroform	35
Anisole	32
Tetrahydrofuran	31
Ethanol	8
Water	< 0.1

Table 3.1 Solubility (mg mL^{-1}) of the PEG-IDIDF in various solvents at room temperature

Compound	Abs.(Sol) [nm]	Abs.(Film) [nm]	HOMO(Film) [eV]	LUMO(Film) [eV]	E_g^{opt} [eV]
IDIDF	440	507	-5.18	-2.90	2.28
PEG-IDIDF	439	505	-5.03	-2.79	2.24

Table 3.2 Optical and electrochemical characteristics of the IDIDF and PEG-IDIDF

3.3.2 Structual Analyses of HTM

To identify the film morphologies of the PEG-IDIDF, the tapping-mode atomic force microscopy (AFM) images and their optical images are examined. As shown in **Figures 3.5 and 3.6**, the PEG-IDIDF film was also prepared by employing CF and ethanol solvents. The film processed by ethanol provided the more layer-like surface morphologies with low RMS values of 1.02 nm compared than the film processed by the CF (2.40 nm). The film prepared by the ethanol with a high boiling point (<80 °C) than that of the chloroform (<60 °C) led to larger grains. It may be owing to a slower solvent evaporation feature of ethanol, which can allow for more structural rearrangement prior to film solidification. But, this ethanol-processed film provided somewhat unfavorable morphologies with low film crystallinity. To adjust proper grains and preferential morphological variation, the PEG-IDIDF films are fabricated by the binary solvent system (ethanol water co-solvents), which possibly induces the formation of well-ordered film morphology. The ethanol-water composition varied from 10:0 to 8.5:1.5 (vol%:vol%). As seen in the inset pictures of **Figure 3.7**, the PEG-IDIDF was well dissolved up to a composition containing 10% water. Surprisingly, as the water content increased from 0 to 10%, the PEG-IDIDF film exhibited larger grains and smooth morphologies

compared to those formed with a single solvent. However, when the water content increased up to 12%, the solubility of PEG-IDIDF started to drop significantly and then became nearly insoluble in higher water content, and thereby the largely aggregated morphologies were observed, and these phenomena became more severe in higher water content. Consequently, an aqueous processing approach with proper co-solvents is highly effective for achieving homogeneous film morphology.

To clarify the molecular orientation and stacking of the IDID derivatives, X-ray diffraction (XRD) and grazing wide angle X-ray scattering (GIWAXS) analyses are carried out, where the IDID derivatives films are dissolved in various solvents systems. As shown in **Figure 3.8**, the out-of-plane XRD patterns of IDIDF and PEG-IDIDF films were fabricated by the CF solvent. For the film of PEG-IDIDF, several distinct diffraction peaks at $2\theta = 5.70°$, 11.41°, and 17.13° were observed when the IDIDF film exhibited a diffraction peak at $2\theta = 4.23°$. These features suggest that the PEG-IDIDF has a well-ordered crystalline film with edge-on orientation than the IDIDF. To clarify the crystallization of films of PEG-IDIDF depending on the various solvents, we have also quantified the full width at half the maximum (FWHM) intensity of the first XRD diffraction peak and summarized in **Table 3.3**. The PEG-IDIDF film fabricated by the ethanol revealed the highest FWHM value of 0.293 $Å^{-1}$,

which was likely relevant to the reduced crystallinity feature induced by the small grains. The FWHM values are decreased as the water content increased, and the PEG-IDIDF film fabricated by using ethanol water co-solvent (90:10) ratio showed a similar FWHM value (0.164 $Å^{-1}$) compared to the film fabricated by CF solvent (0.157$Å^{-1}$). These results imply that an optimal water content in ethanol solvent produced more ordered edge-on crystallites of PEG-IDIDF in film states, even using green solvents.

To further clarify the molecular orientation and stacking of the PEG-IDIDF in film state, the GIWAXS analyses are carried out **(Figure 3.9).** According to single crystal analysis, the IDIDF molecule stacked toward the a-axis with the slipped π-stacking motif. Thus, it can be assumed that both IDIDF and PEG-IDIDF have similar packing motifs owing to their similar backbone structure with two long-axis hexyl chains. The presence of distinct Bragg spots in the PEG-IDIDF also suggests the formation of more oblique orientation toward edge-on direction than IDIDF. As seen, the PEG-IDIDF film processed by the CF, strong diffraction peaks were observed along the direction at q_z = 0.41 $Å^{-1}$, 0.81 $Å^{-1}$, 1.08 $Å^{-1}$ and 1.21$Å^{-1}$ (d-spacing of 15.05 Å, 7.74 Å, 5.82 Å and 5.19 Å). In clear contrast, several diffraction peaks such as q_z = 1.08 $Å^{-1}$ were not found in the PEG-IDIDF film fabricated by ethanol/water co-solvents. In addition, the strong and distinct Bragg rods were observed for the PEG-

IDIDF film in qxy=0.39 $Å^{-1}$, and 0.78 $Å^{-1}$, indicative of a more oblique orientation toward the edge-on direction, which may facilitate charge transport in the device. These experimental findings imply that adding a proper amount of water to ethanol highly affect the enhancement in crystalline nature and film morphology due to the highly-ordered molecular stacking of the PEG-IDIDF.

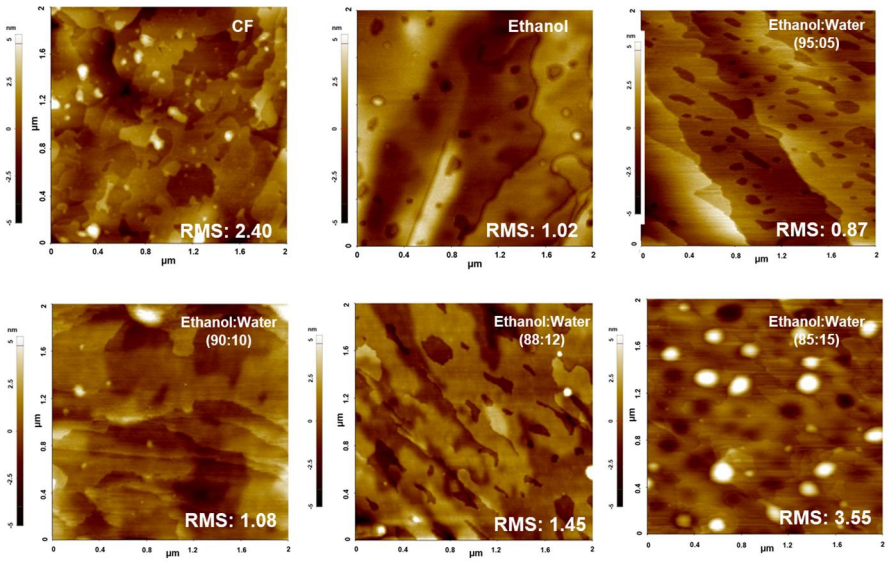

Figure 3.5 AFM topography images (2 μm × 2 μm) of the PEG-IDIDF films processed from various solvents

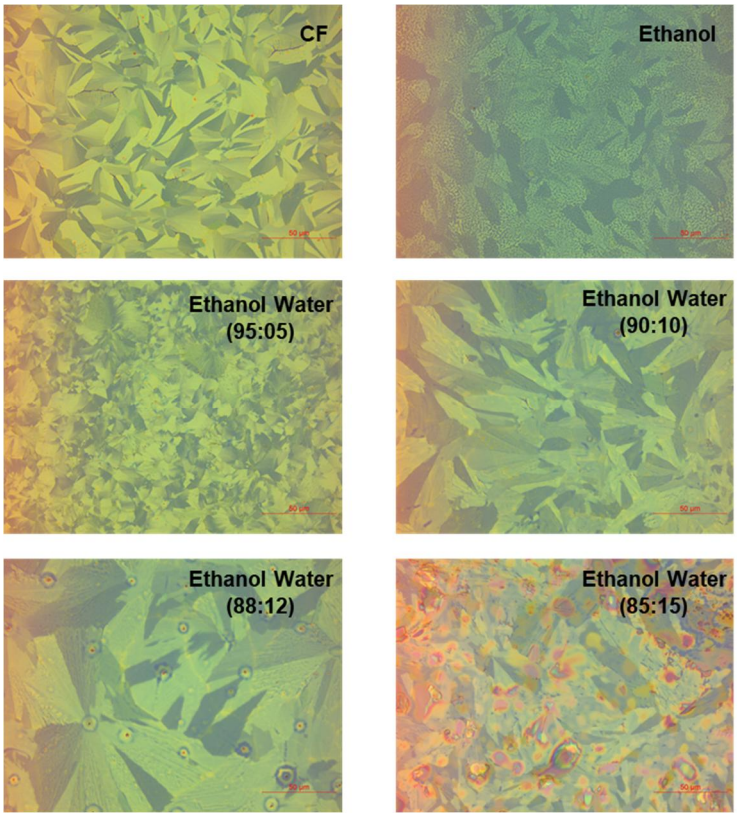

Figure 3.6 Optical images of the PEG-IDIDF films processed from various solvents

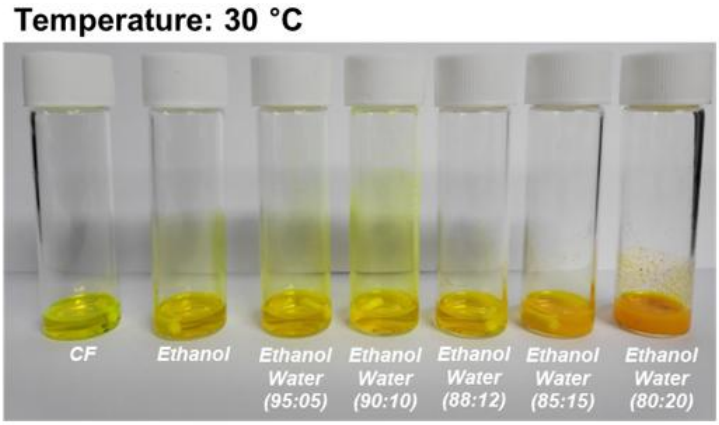

Figure 3.7 Photographic image of PEG-IDIDF (8mg/mL) solutions

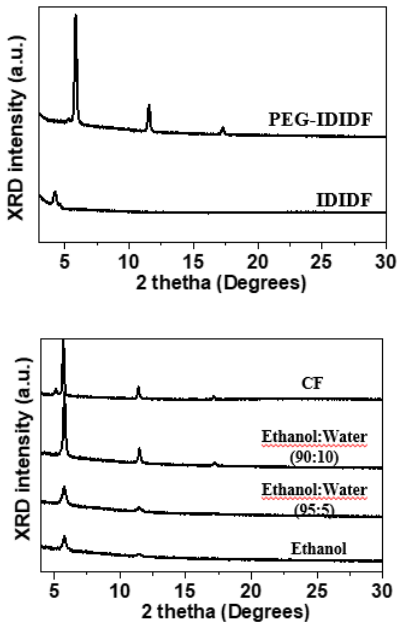

Figure 3.8 Out-of-plane XRD spectra of the IDIDF and PEG-IDIDF processed with CF and Out-of-plane XRD spectra of the PEG-IDIDF processed with various solvents

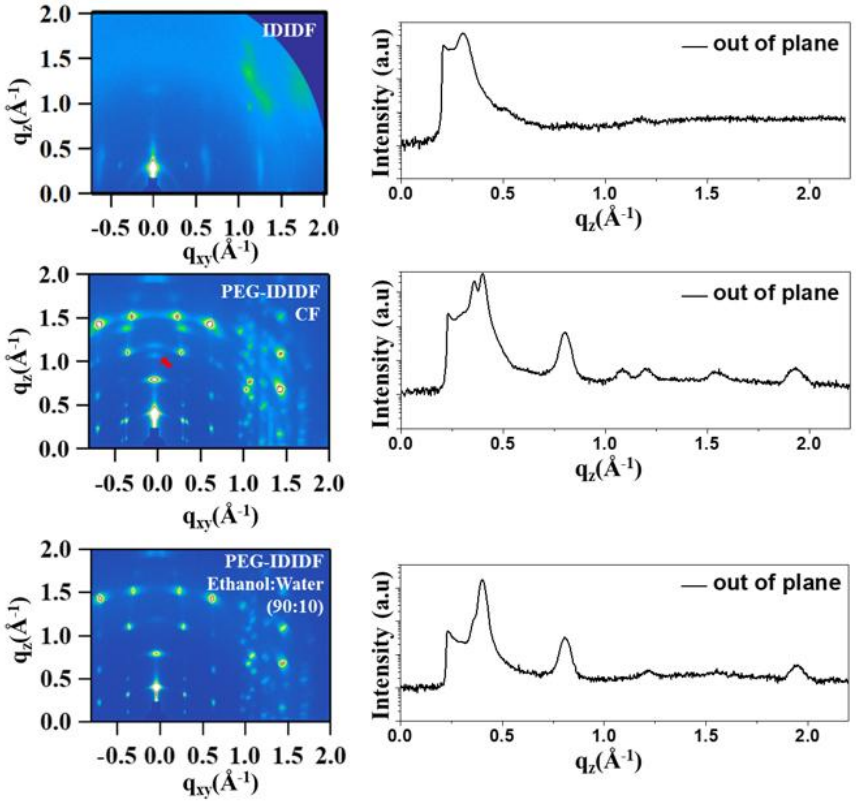

Figure 3.9 GIWAXS patterns and out of plane line-cuts of the IDIDF, PEG-IDIDF processed with CF, and PEG-IDIDF processed with ethanol water co-solvent (90:10)

Compound	2theta	d(Å)
IDIDF	4.23	20.87
PEG-IDIDF	5.13	17.22
	5.70	14.72
	11.41	7.75
	17.13	5.17

Compound	Solvent	FWHM($Å^{-1}$)
PEG-IDIDF	CF	0.157
	Ethanol	0.293
	Ethanol:Water [95:5]	0.248
	Ethanol:Water [90:10]	0.164

Table 3.3 Summarize d-spacing parameters of the IDIDF, and PEG-IDIDF films processed with the CF solvent and FWHM values of the first peak of XRD analyses of PEG-IDIDF with various solvents

3.3.3 Solution-Processed OFET Characteristics

To evaluate the charge transport characteristics of the IDIDF and PEG-IDIDF, the bottom-gate/top-contact (BGTC) solution-processed OFETs are tested. The CF processed IDIDF OFETs yielded the low hole mobility of 1.32 × 10^{-4} cm^2 V^{-1} s^{-1}. On the other hand, the PEG-IDIDF based OFETs demonstrated higher mobility of 8.08 × 10^{-4} cm^2 V^{-1} s^{-1} with a current on/off ratio ~ 10^4, which was mainly ascribed to preferred edge-on molecular orientation, and their device performances are summarized in **Table 3.4**. The PEG-IDIDF OFETs prepared by the ethanol exhibited hole-mobility of 5.53 × 10^{-4} cm^2 V^{-1} s^{-1}. As we expected, the hole mobilities of the PEG-IDIDF devices were enhanced with the addition of water. As shown in **Figure 3.10 and 3.11**, the representative transfer and output characteristics of the PEG-IDIDF processed by the optimum ethanol water (90:10) ratio. The device showed the highest carrier mobility of 4.07 × 10^{-3} cm^2 V^{-1} s^{-1}, along with the highest current on/off ratio of ~ 10^6. When the water content increased over

12%, the device performance was decreased due to the presence of large aggregated morphologies and the device performance summarized in **Table 3.5**. **Figure 3.12** exhibits the solvent-dependent hole mobility trend for the PEG-IDIDF devices, along with the enhancement in device performance. In addition, the overall electrical characteristics of the PEG-IDIDF device is in good agreement with the results of the XRD and GIWAXS analyses. Thus, the experimental observations support that a suitable aqueous process through additional water enables the proper formation of highly ordered packing, thereby facilitating efficient charge transporting characteristics of their corresponding OFETs.

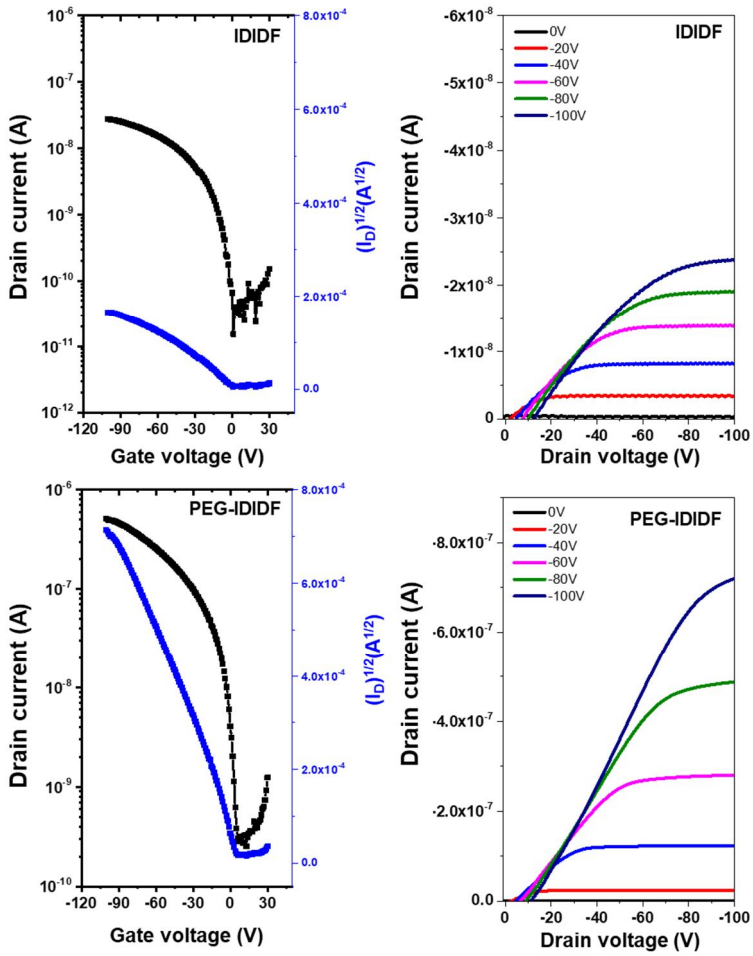

Figure 3.10 Transfer and output characteristics of the IDIDF and PEG-IDIDF processed with CF

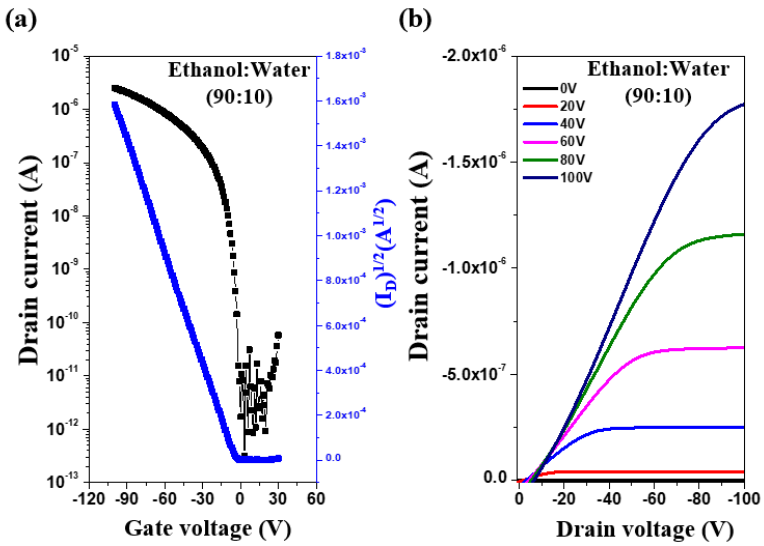

Figure 3.11 Transfer and output characteristics of the PEG-IDIDF processed with Ethano:Water (90:10)

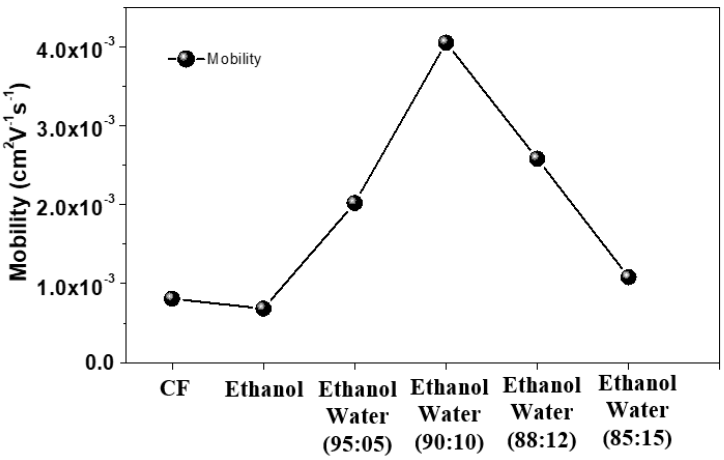

Figure 3.12 Diverse solvent-dependent mobility of the PEG-IDIDF OFETs.

Compound	Solvent	μ_h [cm^2/Vs]	V_{th} [V]	I_{on}/I_{off}
IDIDF	CF	1.32 x 10^{-4}	-1 ± 1	10^3
PEG-IDIDF	CF	8.08 x 10^{-4}	-3 ± 4	10^4

Table 3.4 OFET device performance of IDIDF, and PEG-IDIDF film processed by CF solvent

Compound	Solvent	μ_h [cm^2/Vs]	V_{th} [V]	I_{on}/I_{off}
PEG-IDIDF	Ethanol	5.53 × 10^{-4}	3 ± 3	10^4
	Ethanol:Water (95:5)	1.00 × 10^{-3}	3 ± 2	10^3
	Ethanol:Water (90:10)	4.07 × 10^{-3}	1 ± 5	10^6
	Ethanol:Water (88:12)	2.01 × 10^{-3}	3 ± 4	10^5
	Ethanol:Water (85:15)	9.08 × 10^{-4}	2 ± 2	10^4

Table 3.5 OFET device performance including the PEG-IDIDF film processed from Ethanol and various ethanol water co-solvents

3.4 Conclusion

In this letter, we report the simple and effective ethanol/water co-solvent approach to obtain the enhanced device outputs of OFETs. The chain length of OEG solubilizing moieties was carefully engineered to the rigid conjugated backbone for the achievement of sufficient solubility and better crystallinity inherently necessary for small molecular based-OFETs. The PEG-IDIDF provide outstanding solubility in common organic solvent and high soluble feature in alcohol solvent. Moreover, the PEG-IDIDF provided that the advanced crystallinity feature in film state which is highly linked with the tight molecular packing. Altogether, these properties contributed to yielding excellent hole mobility of 4.07×10^{-3} cm^2 V^{-1} s^{-1}. Thus, we anticipate that these findings will aid the practical progress toward the realization of high-performance small molecule OSCs processable with green solvents.

3.5 Reference

[1] C. Arias, J. D. MacKenzie, I. McCulloch, J. Rivnay and A. Salleo, *Chem. Rev.*, 2010, **110**, 3-24.

[2] H. Sirringhaus, *Adv. Mater.*, 2005, **17**, 2411-2425.

[3] C. D. Dimitrakopoulos and P. R. L. Malenfant, *Adv. Mater.*, 2002, **14**, 99-117.

[4] M. Chen, L. Yan, Y. Zhao, I. Murtaza, H. Meng and W. Huang, *J. Mater. Chem. C*, 2018, **6**, 7416-7444.

[5] J. Wu, Q. Li, G. Xue, H. Chen and H. Li, *Adv. Mater.*, 2017, **29**, 1606101.

[6] S. Vegiraju, G.-Y. He, C. Kim, P. Priyanka, Y.-J. Chiu, C.-W. Liu, C.-Y. Huang, J.-S. Ni, Y.-W. Wu, Z. Chen, G.-H. Lee, S.-H. Tung, C.-L. Liu, M.-C. Chen and A. Facchetti, *Adv. Funct. Mater.*, 2017, **27**, 1606761.

[7] Y. Yuan, G. Giri, A. L. Ayzner, A. P. Zoombelt, S. C. B. Mannsfeld, J. Chen, D. Nordlund, M. F. Toney, J. Huang and Z. Bao, *Nat. Commun.*, 2014, **5**, 3005.

[8] F. Campana, C. Kim, A. Marrocchi and L. Vaccaro, *J. Mater. Chem. C.*, 2020, **8**, 15027-15047.

[9] J. Cho, S. H. Yu and D. S. Chung, *J. Mater. Chem. C.*, 2017, **5**, 2745-2757.

[10] G. Kim, S.-J. Kang, G. K. Dutta, Y.-K. Han, T. J. Shin, Y.-Y. Noh and C. Yang, *J. Am. Chem. Soc.*, 2014, **136**, 9477-9483.

[11] ECHA (European Chemical Agency). Registration, Evaluation, Authorisation and Restriction of Chemicals (REACH). https://echa.europa.eu/regulations/reach/understanding-reach.

[12] Z. Ma, B. Zhao, Y. Gong, J. Deng and Z. a. Tan, *J. Mater. Chem. A.*, 2019, **7**, 22826-22847.

[13] J. Mei and Z. Bao, *Chem. Mater.*, 2014, **26**, 604-615.

[14] C. Duan, K. Zhang, C. Zhong, F. Huang and Y. Cao, *Chem. Soc. Rev.*, 2013, **42**, 9071-9104.

[15] Z. Wang, Y. Shi, Y. Deng, Y. Han and Y. Geng, *Adv. Funct. Mater.*, 2021,

31, 2104881.

[16] H. Wei, H. Zhang, G. Jin, T. Na, G. Zhang, X. Zhang, Y. Wang, H. Sun, W. Tian and B. Yang, *Adv. Funct. Mater.*, 2013, **23**, 4035-4042.

[17] H. Borchert, E. V. Shevchenko, A. Robert, I. Mekis, A. Kornowski, G. Grübel and H. Weller, *Langmuir*, 2005, **21**, 1931-1936.

[18] J. Lee, S. A. Park, S. U. Ryu, D. Chung, T. Park and S. Y. Son, *J. Mater. Chem. A.*, 2020, **8**, 21455-21473.

[19] S. Zhang, J. Gao, W. Wang, C. Zhan, S. Xiao, Z. Shi and W. You, *ACS Appl. Energy Mater.*, 2018, **1**, 1276-1285.

[20] R. Kim, B. Kang, D. H. Sin, H. H. Choi, S.-K. Kwon, Y.-H. Kim and K. Cho, *Chem. Commun.*, 2015, **51**, 1524-1527.

[21] C. Lee, H. R. Lee, J. Choi, Y. Kim, T. L. Nguyen, W. Lee, B. Gautam, X. Liu, K. Zhang, F. Huang, J. H. Oh, H. Y. Woo and B. J. Kim, *Adv. Energy Mater.*, 2018, **8**, 1802674.

Abstract in Korean

에틸렌 글라이콜과 인돌로[3,2-b]인돌을 기반으로 한 유기반도체의 합성, 특성 및 응용에 대한 연구

서울대학교 대학원

재료공학부

홍승화

용액 공적이 가능한 유기반도체의 경우 유연성, 화학적 가능성 등 다양한 장점들로 인하여 많은 연구가 진행되고 있다. 특히, 이종원소를 포함하는 접합된 복소고리 방향족 화합물의 경우 독특한 광학적 및 전기적 특성, 확장된 공액구조등 다양한 특성에 의해서 매력적인 기반 구조체로서 연구되었다. 다양한 복소고리 방향족 화합물 중에서 특히 피롤을 포함하는 화합물들의 경우 다른 복소고리 방향족과는 다르게 분자구조 변형 및 용해도를 좀 더 쉽게 조절 할 수 있는 것을 토대로 많은 연구가 집중되었지만 아직까지 피롤을 포함하는 복소고리 방향족 화합물의 경우 상대적으로 연구가 미진한 부분이 있다. 다양항 피롤을 포함하는 복소고리 방향족 화합물 중에서, 본 저자는 안쪽에 두 개의 피롤 링과 바깥쪽에 두 개의 벤젠링을 접합된 구조의 인돌로[3.2-b]인돌 (IDID) 구조체에 관하여

서 연구에 대해서 주목하였으며 특히 IDID의 (3,8-) 위치에 플로린 (Fluroine, F) 원자를 도입을 하게 될 경우 유도체의 평면화와 연장, 분자간의 쌓임을 야기하는데 매우 긍정적인 부분이 있는 것을 확인 하였다. 하지만 다음 유도체의 경우 유도체의 평면화와 증진됨에 따라서 용액공정에 필요한 용해도가 감소하는 문제를 해결 하는 것이 매우 중요하다고 생각하여, 이를 바탕으로 본 학위논문에서는 다음의 두가지 주요 주제에 관련하여 서술하였다. 1) 가장 보편적으로 용해도를 증진시키기 위해 사용되는 유연한 알킬 (alkyl) 그룹 대신에 사용될 수 있는 에틸렌 글라이콜 사슬을 도입 함으로써 용해도 뿐만 아니라 분자 유도체의 강한 분자간의 파이-상호작용을 같이 야기하여 더욱더 견고한 분자 쌓임을 유도 ㄴ) 에틸렌 글라이콜의 길이를 적적하게 적용하여 다양한 고효율 유기반도체 구현을 위한 분자설계.

최근 페로브스카이 태양전지의 정공전달층용 물질 개발에 대한 많은 연구가 진행되고 있으며 특히 *p-i-n* 소자 구조와 *n-i-p* 소자 구조에서 많이 활용 되고 있다. 특히 단분자 유도체의 경우 첨가제가 필요 없는 높은 전공 이동도를 가지는 정공전달층용 단분자를 개발해야하며, 이를 위해서는 분자구조의 평면도가 높고 우수한 결정성을 가지는 고성능 정공전달층용 단분자의 개발이 절실히 요구되고

있다. 하지만 평면도가 높고 우수한 결정성을 가지는 분자구조 일수록 공정에 필요한 용해도가 감소 하기 때문에 적절한 균형을 맞출 필요가 있다.

이를 바탕으로 본 학위논문에서는 보고된 정공전달층용 물질인 IDIDF 유도체에서 *N*-위치에 있는 유연한 알킬 그룹 대신에 에틸렌 글라이콜 사슬을 도입하여서 용해도와 더욱 강한 분자간 파이−상호작용을 야기하고자 하였다. diethylene glycol (DEG) 사슬을 도입한 (DEG-IDIDF) 유도체를 개발하였다. 개발된 DEG-IDIDF의 경우 *p-i-n* 페로브스카이트 태양전지에 정공 전달 층으로 사용하여 고성능의 특성을 확인 하였다. 특히 상용의 정공 전달 물질인 PEDOT:PSS 와 보고된 IDIDF 물질 보다 우수한 성능을 보이는 것을 확인 하였다. 결과적으로 DEG-IDIDF를 정공 전달 물질로 사용한 페로브스카이트 태양전지 소자에서 16.60%의 광 에너지 전환 호율 (power conversion efficiency, PCE)를 보였으며, 뛰어난 열 안정성을 보이는 것으로 에틸렌 글라이콜 사슬이 도인된 IDID 기반의 물질이 새로운 고효율의 페로브스카이트 태양 전지용 정공 수송 물질로의 사용 가능성을 확인할 수 있었다.

다만, n−i−p 페로브스카이트 태양전지에서 정공 전달 층으로 사용하기 위해서는 페로브스카이트 층을 충분히 덮을 수 있는 두께

를 만족 해야하기 때문에 용해도를 증진 시키기 위해서 DEG 사슬 대신 Tri-ethylene glycol (TEG) 사슬을 도입하여 TEG-IDIDF 물질을 개발 하였다. 비록 좀 더 긴 사슬이 도입 되었지만 공정에 필요한 용해도를 확보 하였으며 TEG사슬에서 산소 원소와 IDID 구조체의 수소 원소간의 강한 수소 결합에 의해서 더욱 강한 분자간 파이−상호작용을 야기하여 더욱 견고한 분자 쌓임을 가능하게 하였다.따라서, TEG-IDIDF의 경우 첨가제 없이도 첨가제를 사용한 상용의 정공 전달 물질인 Spiro-OMeTAD보다 우수한 정공 이동도를 나타냄을 확인 하였다. 결과적으로, TEG-IDIDF를 정공 전달층 물질로 사용한 $MAPbI_3$ 페로브스카이트 태양전지 소자에서 첨가제 없이도 18%의 광전 변환 효율을 나타내었으며, $FAPbI_3$ 페로브스카이트 태양전지 소자에서는 첨가제를 넣을 경우 22.71%, 첨가제가 없을 경우 20.42% PCE를 보였다. 특히 TEG-IDIDF를 활용한 페로브스카이트 태양전지 소자의 경우 높은 습도(60%)에서도 50일 동안 80% 이상의 소자 효율을 유지하는 것을 확인 하였다.

한편, 유해한 화학물질 대신 친환경 유기반도체 소자에 대한 연구가 많이 진행 됨에 따라서, 독성용매가 아닌 물과 에탄올과 같은 친환경 용매에도 녹을 수 있는 물질 개발에 대한 연구가 필요하다. 따라서, 더욱 길이가 늘어난 에틸렌 글라이콜 사슬 Penta-ethylene

glycol (PEG) 사슬을 도입하여 용해도를 높여 에탄올에도 녹을 수 있도록 했다. 이때 합성된 단분자 물질인 PEG-IDIDF의 경우 유기 전계-효과 트랜지스터 (Organic field-effect transistor) 소자에서 높은 이동도의 p-형 반도체 특성을 보였다. 또한 박막의 결정성을 높이기 위해서 에탄올에 소량의 물을 첨가 할 경우 우수한 형태의 필름이 형성됨과 함께 트랜지스터에 적합한 배향을 가지는 것을 확인 하였으며 친환경 용매를 활용해서 매우 높은 반도체 p-형 반도체 특성 (4.07×10^{-3} cm^2 V^{-1} s^{-1}, on/off ratio of ~10^6)을 확인 하였다.

주요어: 인돌로[3,2-b]인돌, 정공 수송, 에틸렌 글라이콜 사슬, 무첨가제 및 첨가제 페로브스카이트 정공 전달 물질, 유기 전계-효과 트랜지스터, 친환경용매

학번: 2019-32576

List of Publication

1. Seung Hwa Hong, Seong Il Kim, Dong Won Kim, and Soo Young Park*, “Impact of diethylene glycol chains on indolo [3,2-b]indole based small molecule as dopant-free hole transporting materials for efficient and stable inverted perovskite solar cells”, Organic Electronics, 2023, 113, 106719

2. Seung Hwa Hong, Dong Won Kim, and Soo Young Park*, “Aqueous-alcohol-processable indolo[3,2-b]indole-based crystalline small molecules for organic field effect transistors with oligo(ethylene glycol) side chain”, Dyes and Pigments, 2023, 10, 111093

3. Dong Won Kim; Min-Woo Choi; Won Sik Yoon; Seung Hwa Hong; Sungjin Park; Ji Eon Kwon; Soo Young Park, “A dopant-free donor–acceptor type semi-crystalline polymeric hole transporting material for superdurable perovskite solar cells”, J. Mater. Chem. A, 2022, 10, 12187–12195.

4. Seungyun Baik, Dong Won Kim, Hyun-Sik Kang, Seung Hwa Hong, Sungjin Park, Byeong-Kwan An and Soo Young Park, “ITIC derivative acceptors for ternary organic solar cells: fine-tuning of absorption bands, LUMO energy levels, and cascade charge transfer”, Sustainable Energy Fuels, 2022, 6, 110–120.

5. Jin Hong Kim, Min-Woo Choi, Won Sik Yoon, Sangyoon Oh, Seung Hwa Hong, and Soo Young Park, “Structural and Electronic Origin of Bis-Lactam Based High Performance Organic Thin Film Transistors”, ACS Appl. Mater.

Interfaces 2019, 11, 8301−8309.

6. Jun-Mo Park, Dong Won Kim, Hae Yeon Chung, Ji Eon Kwon, Seung Hwa Hong, Tae-Lim Choi *b and Soo Young Park, “A Stereoregular β-Dicyanodistyrylbenzene (β-DCS)-based Conjugated Polymer for High-Performance Organic Solar Cells with Small Energy Loss and High Quantum Efficiency”, J. Mater. Chem. A, 2017, 5, 16681–16688.

7. Sang Kyu Park, Jin Hong Kim, Tatsuhiko Ohto, Ryo Yamada, Andrew O. F. Jones, Dong Ryeol Whang, Illhun Cho, Sangyoon Oh, Seung Hwa Hong, Ji Eon Kwon, Jong H. Kim, Yoann Olivier, Roland Fischer, Roland Resel, Johannes Gierschner, Hirokazu Tada, and Soo Young Park*, “Highly Luminescent 2D-type Slab Crystals Based on a Molecular Charge-Transfer Complex as Promising Organic Light-Emitting Transistor Materials”, Adv. Mater. 2017, 29, 1701346

List of Presentation

1. S. H. Hong, D. W. Kim, J. M. Park, S. K. Park, and S. Y. Park, “Indoloindole-based HoleTransporting Material for Highly Efficient Perovskite Solar Cells”, IUPAC-FAPS 2017 Polymer Congress, October 13, 2017, Jeju, Korea.

2. Seung Hwa Hong, Dong Won Kim, Illhun Cho, Jun Mo Park, Ji Eon Kwon, Sang Kyu Park and Soo Young Park, “Indoloindole-based Crystalline Hole Transport Material for Highly Efficient Dopant-Free Perovskite Solar Cells”, Perovskite Photonics Conference 2017, November 21, 2017, Jeju, Korea.

3. Seung Hwa Hong, Dong Won Kim, Illhun Cho, Ji Eon Kwon, Jun-Mo Park, Sang Kyu Park and Soo Young Park, “Indoloindole-based Crystalline Hole Transport Material for Highly Efficient Dopant-Free Perovskite Solar Cells”, 2018 Materials Research Society Spring Meeting & Exhibit, April 6, 2018, Phoenix, Arizona.

List of Patents

박수영 권지언 김동원 **홍승화** 안병관 최강훈 강현식, “신규 화합물 및 그의 정공전달층으로의 용도”, 출원번호 “10-2018-0091181”, 등록번호 “제-10-2128578호”